



National Library  
of Canada

Acquisitions and  
Bibliographic Services Branch

395 Wellington Street  
Ottawa, Ontario  
K1A 0N4

Bibliothèque nationale  
du Canada

Direction des acquisitions et  
des services bibliographiques

395, rue Wellington  
Ottawa (Ontario)  
K1A 0N4

*Your file - Votre référence*

*Our file - Notre référence*

## NOTICE

The quality of this microform is heavily dependent upon the quality of the original thesis submitted for microfilming. Every effort has been made to ensure the highest quality of reproduction possible.

If pages are missing, contact the university which granted the degree.

Some pages may have indistinct print especially if the original pages were typed with a poor typewriter ribbon or if the university sent us an inferior photocopy.

Reproduction in full or in part of this microform is governed by the Canadian Copyright Act, R.S.C. 1970, c. C-30, and subsequent amendments.

## AVIS

La qualité de cette microforme dépend grandement de la qualité de la thèse soumise au microfilmage. Nous avons tout fait pour assurer une qualité supérieure de reproduction.

S'il manque des pages, veuillez communiquer avec l'université qui a conféré le grade.

La qualité d'impression de certaines pages peut laisser à désirer, surtout si les pages originales ont été dactylographiées à l'aide d'un ruban usé ou si l'université nous a fait parvenir une photocopie de qualité inférieure.

La reproduction, même partielle, de cette microforme est soumise à la Loi canadienne sur le droit d'auteur, SRC 1970, c. C-30, et ses amendements subséquents.

Canada

THE UNIVERSITY OF ALBERTA

THE DYNAMIC EVALUATION OF ALVEOLAR FLUID CLEARANCE  
USING PROTON AND DEUTERON  
NUCLEAR MAGNETIC RESONANCE IMAGING

BY



PATRICK WILLIAM STROMAN

A THESIS  
SUBMITTED TO THE FACULTY OF GRADUATE STUDIES AND  
RESEARCH IN PARTIAL FULFILLMENT OF THE REQUIREMENTS FOR  
THE DEGREE OF DOCTOR OF PHILOSOPHY  
IN  
MEDICAL SCIENCES

DEPARTMENT OF APPLIED SCIENCES IN MEDICINE

EDMONTON, ALBERTA

FALL 1993



National Library  
of Canada

Acquisitions and  
Bibliographic Services Branch

395 Wellington Street  
Ottawa, Ontario  
K1A 0N4

Bibliothèque nationale  
du Canada

Direction des acquisitions et  
des services bibliographiques

395, rue Wellington  
Ottawa (Ontario)  
K1A 0N4

*Your file* *Votre référence*

*Our file* *Notre référence*

The author has granted an irrevocable non-exclusive licence allowing the National Library of Canada to reproduce, loan, distribute or sell copies of his/her thesis by any means and in any form or format, making this thesis available to interested persons.

L'auteur a accordé une licence irrévocable et non exclusive permettant à la Bibliothèque nationale du Canada de reproduire, prêter, distribuer ou vendre des copies de sa thèse de quelque manière et sous quelque forme que ce soit pour mettre des exemplaires de cette thèse à la disposition des personnes intéressées.

The author retains ownership of the copyright in his/her thesis. Neither the thesis nor substantial extracts from it may be printed or otherwise reproduced without his/her permission.

L'auteur conserve la propriété du droit d'auteur qui protège sa thèse. Ni la thèse ni des extraits substantiels de celle-ci ne doivent être imprimés ou autrement reproduits sans son autorisation.

ISBN 0-315-88148-8

Canada

July 6, 1993

Re: Manuscript entitled: "Evaluation of the effects of PAF on alveolar fluid clearance using NMR imaging"

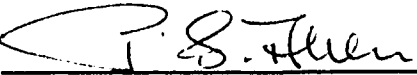
by P. W. Stroman, P. S. Allen, D. C. Lien, G. Machin, S. F. P. Man

The authors permit the reproduction of this manuscript for inclusion as a chapter in the Ph.D. thesis by Patrick W. Stroman, entitled "The Dynamic Evaluation Of Alveolar Fluid Clearance Using Proton And Deuteron Nuclear Magnetic Resonance Imaging".

P. W. Stroman

 date July 14/93


P. S. Allen

 date Aug 4 / 93

D. C. Lien

 date July 14/93

G. Machin

 date July 14/1993

S. F. P. Man

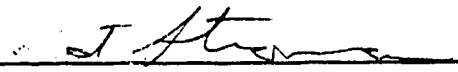
 date August 3/93

July 6, 1993

Re: Manuscript entitled: "In-vivo NMR assessment of bi-directional alveolar fluid fluxes"  
by P. W. Stroman, S. F. P. Man and P. S. Allen

The authors permit the reproduction of this manuscript for inclusion as a chapter in the Ph.D. thesis by Patrick W. Stroman, entitled "The Dynamic Evaluation Of Alveolar Fluid Clearance Using Proton And Deuteron Nuclear Magnetic Resonance Imaging".


P. W. Stroman

 date Aug 3/93

S. F. P. Man

 date Aug 3/93

P. S. Allen

 date Aug 4/93

THE UNIVERSITY OF ALBERTA  
RELEASE FORM

NAME OF AUTHOR: Patrick William Stroman

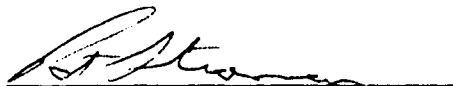
TITLE OF THESIS: The Dynamic Evaluation of Alveolar Fluid Clearance  
Using Proton and Deuteron Nuclear Magnetic Resonance  
Imaging.

DEGREE: Ph. D. in Medical Sciences

YEAR THIS DEGREE GRANTED: 1993

Permission is hereby granted to the University of Alberta Library to reproduce single copies of this thesis and to lend or sell such copies for private, scholarly or scientific research purposes only.

The author reserves all other publication and other rights in association with the copyright in the thesis, and except as hereinbefore provided neither the thesis nor any substantial portion thereof may be printed or otherwise reproduced in any material form whatever without the author's prior written permission.



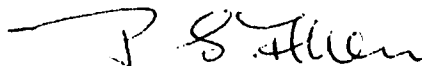
Patrick W. Stroman  
407 10610 83<sup>rd</sup> Avenue  
Edmonton, Alberta  
T6E 2E2

Aug 5/93

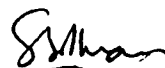
THE UNIVERSITY OF ALBERTA

FACULTY OF GRADUATE STUDIES AND RESEARCH

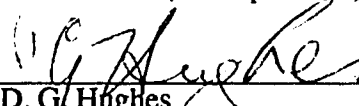
The undersigned certify that they have read, and recommend, a thesis entitled  
THE DYNAMIC EVALUATION OF ALVEOLAR FLUID CLEARANCE  
USING PROTON AND DEUTERON NUCLEAR MAGNETIC RESONANCE  
IMAGING submitted by PATRICK WILLIAM STROMAN in partial fulfilment  
of the requirements for the degree of DOCTOR OF PHILOSOPHY in MEDICAL  
SCIENCES.



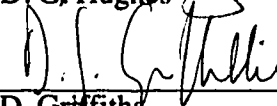
Dr. P. S. Allen (Co-supervisor)



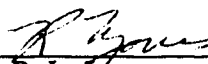
Dr. S. F. P. Man (Co-supervisor)



Dr. D. G. Hughes



Dr. D. Griffiths



Dr. R. L. Jones



for Dr. D. C. Lien



for Dr. D. C. Ailion

Date: Aug 5/93

Dedicated to my family.

To my Mom and Dad,  
to my brothers, Leland and Michael,  
and to my sisters, Veronica, Mary-  
Anne, and Melanie.

To my beautiful wife, Janet.

## **Abstract**

Nuclear magnetic resonance (NMR) imaging is a sensitive, non-invasive technique for monitoring extravascular lung water (EVLW), *in-vivo*. Previous studies carried out in this facility have monitored the temporal changes in EVLW content during the development of increased permeability pulmonary edema (D. M. Phillips, M.Sc. Thesis, University of Alberta, 1987). In this project we continued with the development of NMR imaging techniques to study the clearance of lung fluid during the resolution of alveolar edema.

In the first phase of this study, a bolus of autologous serum, or autologous serum plus platelet-activating factor (PAF), was instilled into one lung lobe in an anesthetized cat and was monitored with  $^1\text{H}$  NMR imaging for 4 hours. PAF is an inflammatory mediator produced by the lung in some disease states. Images showed that serum alone was cleared slowly from the lung with 86% of that instilled remaining after 4 hours. With PAF the clearance was bi-phasic with a rapid initial clearance, and only 35% of the instillate remained after 4 hours.

To investigate whether PAF influenced fluid absorption from the airspaces or secretion into the airspaces, in the second phase of this study, the instillate was a 50%  $\text{D}_2\text{O}$  serum-like solution (SLS). Fluid absorption was monitored with  $^2\text{H}$  NMR imaging while the combined effects of fluid absorption and secretion were monitored, as before, with  $^1\text{H}$  NMR imaging. Without PAF, fluid was secreted into the airspaces steadily with the equivalent of 30% of the instilled volume over 4 hours. Fluid absorption from the airspaces was relatively constant when SLS was the instillate with 50% absorbed over 4 hours. With PAF, however, the absorption was markedly bi-phasic with a rapid initial absorption that slowed considerably after 1 hour, resulting in 60% of that instilled being absorbed over 4 hours.

These results indicated that PAF enhances absorption from the alveolar space without affecting secretion processes, resulting in an enhanced net clearance. Also, these results are the first *in-vivo* observations of bi-directional fluid movements across the pulmonary air-blood barrier and demonstrate its hitherto unknown and unexpected high degree of activity.

## **Acknowledgements**

I would like to thank Dr. Peter Allen and Dr. Paul Man for their supervision over the course of this project, for all they have taught me, and for their enthusiasm toward this project.

The success of this project is also due to the assistance of Dan Doran, Karim Damji, Dave Ellinger, and Ivy Ho. Their efforts are greatly appreciated.

I would also like to thank my wife, Janet, and Brian and Lorrain Collin, for the support, advice, and great friendship they have given me over the course of this project.

My social and academic life has also been greatly enhanced by people like Dan Doran, Christian Beaulieu, Karim Damji, Frances Fenrich, Dr. Ravi Menon, Dr. George Sexsmith, Sue Albo, Dr. Laird Trimble, Dr. Chris Hanstock, Alan Wilman, Frank Ye, Dr. Gang Zhu, Dan Gheorghiu, Paul Labreque, and Andrew Hirsch.

Lastly, I would like to acknowledge the Department of Applied Sciences in Medicine for a Research Assistantship, and the Alberta Lung Association for a Postgraduate Studentship.

## **Table of Contents**

1.0 Introduction to the Thesis .....	1
1.1 The Air-Blood Barrier of the Lung .....	2
1.2 The Pulmonary Fluid Balance .....	5
1.3 NMR Studies of Lung Water .....	9
1.3.0 A brief historical overview .....	9
1.3.1 Macroscopic Nuclear Magnetization .....	12
1.3.2 Magnetization Relaxation Processes .....	25
Dipole-Dipole Relaxation .....	26
Quadrupolar Relaxation .....	42
The Two-Site Rapid Exchange Model of Relaxation .....	44
1.3.3 NMR Imaging Theory .....	47
Theory of Spin Echoes and Gradient-Recalled Echoes .....	48
Spatially Selective RF Pulses .....	52
A k-Space Representation of NMR Imaging Theory and Image Reconstruction .....	58
Two-Dimensional Fourier Transform Image Reconstruction .....	60
Backprojection Reconstruction .....	65
1.4 Application of NMR to Studies of Lung Water .....	78
1.5 References .....	80
 2.0 Evaluation of the Effects of PAF on Alveolar Fluid Clearance Using NMR Imaging. ....	 91
2.1 Introduction .....	91
2.2 Methods .....	93

2.2.1 Animal Model Of Alveolar Fluid Clearance .....	93
2.2.2 NMR Imaging .....	96
2.3 Results .....	100
2.4 Discussion .....	106
2.5 Summary .....	110
2.6 References .....	111
 3.0 In-vivo NMR Assessment of Bi-directional Alveolar Fluid Fluxes. ....	116
3.1 Introduction .....	116
3.2 Methods.....	118
3.2.1 Animal Model of Alveolar Fluid Clearance .....	118
3.2.2 $^1\text{H}$ and $^2\text{H}$ NMR Methods .....	120
3.3 Results .....	122
3.4 Discussion .....	128
3.5 Summary .....	133
3.6 References .....	134
 4.0 General Discussion and Veracity of the Conclusions .....	138
4.1 NMR and Gravimetric Measurements of Clearance Rates .....	138
4.2 Transverse Relaxation Time Measurements of Water Protons .....	139
4.3 A Model of the Lung Fluid Balance .....	142
4.4 References .....	152
 5.0 Summary .....	154
 Appendix 1.1: Detailed Calculations of the Motions of Spins in the Presence of a Rotating Magnetic Field .....	158

Appendix 3.1: Deuteron NMR Techniques Employed for Monitoring Instilled Alveolar SLS, or SLS plus PAF .....	162
Appendix 3.2: Proton Transverse Relaxation Time Measurements of Lung Water, after Instillation of either SLS or SLS plus PAF .....	165
Appendix 3.3: Derivation of the Equations used to Compute the Time Course of Alveolar Fluid Absorption and of Alveolar Fluid Secretion .....	170
Appendix 4.1: Flow chart of the Mathematical Model of the Lung Fluid and Solute Exchange .....	173

## **List of Tables**

Table 1.1 Computed intensities at a point P, a distance D from an object of diameter d, after N signal intensity profiles have been projected onto the image plane. ....	75
Table 2.1 The number of cats included in each of the experimental groups .....	96
Table 4.1 Parameters used in a mathematical model of the alveolar fluid exchange.....	144

## **List of Figures**

Figure 1.1 A schematic representation of a portion of the pulmonary air-blood barrier .....	3
Figure 1.2 Motion of a system of non-interacting spins in a frame of reference rotating at angular velocity $\Omega$ in the presence of an applied field, $\mathbf{B}_1$ , rotating at angular velocity $\Omega$ . The system was initially at thermal equilibrium with a net magnetization, $\mathbf{M}$ , along the z axis.....	21
Figure 1.3 Motion of a system of non-interacting spins in a frame of reference rotating at angular velocity $\Omega = -\gamma\mathbf{B}_0$ in the presence of an applied field, $\mathbf{B}_1$ , rotating at angular velocity $\Omega$ . The system was initially at thermal equilibrium with a net magnetization, $\mathbf{M}$ , along the z axis. ....	22
Figure 1.4 Spherical-polar coordinate system used to describe the magnetic field due to a magnetic dipole moment, $\mu$ .....	29
Figure 1.5 The dependence of the normalized Debye spectral density on frequency, expressed relative to the correlation time, $\tau_c$ .....	38
Figure 1.6 The dependence of the quantity, $\omega_0[J(\omega_0) + 4 J(2\omega_0)]$ , and therefore the dependence of $R_1$ , on the value of $\tau_c$ , for a fixed frequency, $\omega_0$ .....	40

Figure 1.7 Schematic representation of water protons in two rapidly exchanging relaxation environments .....45

Figure 1.8 Dephasing of transverse magnetization components due to static magnetic field inhomogeneities, depicted in the rotating frame of reference. ....48

Figure 1.9 The time course of changes in the transverse magnetization of an ensemble of spins due to the effects of static  $B_0$  inhomogeneities being refocussed at a time  $2\tau$  after the initial  $90_x$  RF pulse rotated the magnetization into the transverse plane. ....49

Figure 1.10 NMR signal from an ensemble of spins with the effects of static  $B_0$  inhomogeneities being refocussed at a time  $2\tau$  after the initial  $90^\circ$  RF pulse rotated the magnetization into the transverse plane. ....50

Figure 1.11 The z direction variation of the transverse magnetization of a uniform spin system, after the application of a rectangular  $90^\circ$  RF pulse of duration  $2\tau$  in the presence of a magnetic field gradient in the z direction. The transverse magnetization amplitude has been normalized to equal 1 at  $z = 0$ . ....54

Figure 1.12 The phase distribution of magnetic moments in the transverse plane, along the z direction, after the application of a rectangular  $90^\circ$  RF pulse of duration  $2\tau$  in the presence of a magnetic field gradient in the z direction. ....55

Figure 1.13 The amplitude of the Fourier transform of a rectangular function with amplitude 1/2 and width  $2\tau$ . .....56

Figure 1.14 The z direction variation of the transverse magnetization of a spin system, normalized to 1 at  $z=0$  (solid line), after the application of a Gaussian  $90^\circ$  RF pulse in the presence of a z direction magnetic field gradient. Also, shown for comparison is a Gaussian function having the same maximum amplitude, and width at half maximum, as that of the transverse magnetization distribution (dashed line).....57

Figure 1.15 The phase distribution of magnetic moments in the transverse plane, along the z direction, after the application of a Gaussian  $90^\circ$  RF pulse in the presence of a magnetic field gradient in the z direction.....57

Figure 1.16 Representation of k-space with rectangular sampling .....62

Figure 1.17 Schematic representation of a pulse sequence for rectangular sampling of the data in k-space which corresponds to a transverse imaging plane. ....63

Figure 1.18 The relationship between the number of sample points and the sampling interval in k-space (A) and the resolution and the size of the FOV of the image (B) which results from applying a Fourier transform to the data in k-space. ....65

Figure 1.19 Schematic representation of a pulse sequence for polar sampling of the data in k-space which corresponds to a transverse imaging plane. Values of $G_x$ and $G_y$ are expressed for the $n^{\text{th}}$ of $N$ data acquisition steps. ....	66
Figure 1.20 Representation of k-space with radial or polar sampling .....	67
Figure 1.21 Definition of the coordinates $r$ , $s$ and $\phi$ for a given signal projection, in terms of the fixed cartesian coordinates, $x$ and $y$ .....	68
Figure 1.22 The spatial element of integration as expressed in cartesian and polar coordinates. ....	69
Figure 1.23 An image plane containing three cylindrical objects and the corresponding projection profiles at three polar angles. ....	71
Figure 1.24 The reconstruction of the original image from three projection profiles, back-projected onto the image plane and summed. ....	72
Figure 1.25 A circular object within an image plane, and definition of the reference point $P$ . ....	73
Figure 1.26 A single intensity profile of the object illustrated in figure 1.25, back projected onto the image plane at an angle $\phi$ from the $x$ axis. The dashed lines indicate the center line and edges of the back-projected profile. ....	74

Figure 1.27 Theoretical intensity profiles for an image of the circular object illustrated in figure 1.25, reconstructed by means of a back-projection algorithm. The intensities were computed with the equations listed in table 1.1. The distance from the object center is expressed relative to the object diameter and the intensities are expressed relative to the intensity at the object center. The number of back-projections represented in each of these curves is indicated on the right. .... 76

Figure 2.1 Schematic of the pulse sequence used to obtain 8 spin-echo images of each of 2 non-contiguous slices. The TTL respiratory gating signal indicates when the cat's lungs are not at FRC. In this case, spin conditioning takes place and no gradients are applied and the NMR signal is not acquired..... 98

Figure 2.2 The method used for defining regions of interest in transverse images of a cat's thorax. Only the first spin-echo images are used for monitoring the time course of changes in the lung water content. The intensity of the acquired signal which is due to the instilled fluid is given by:  $I_{inst}(\Delta t) = I_{FF}(\Delta t) - I_{BG}$ ..... 100

Figure 2.3 Transverse images of a cat's thorax ..... 101

Figure 2.4 The time course of alveolar fluid clearance as determined by in-vivo NMR imaging and by gravimetric measurements of excised lungs. Circles indicate averaged NMR intensity data (serum n=6, serum plus PAF n=5). Triangles indicate averaged gravimetric measurements (each group: 1 hour n=2, 4 hours n=9). The dotted line shows the fitted

clearance curve without PAF: % Remaining =  $100\exp(-t/966)$ . The dashed line shows the fitted clearance curve with PAF: % Remaining =  $55\exp(-t/40) + 45\exp(-t/966)$ . ..... 102

Figure 2.5 The time dependence of the time averaged transverse relaxation times of cat lungs containing instilled fluid. The filled circles represent serum instilled into the lungs. The open circles represent serum plus PAF instilled into the lungs. .... 104

Figure 2.6a Photomicrograph of cat lung, 4 hours after instillation of autologous serum plus PAF. .... 105

Figure 2.6b Photomicrograph of cat lung, 4 hours after instillation of autologous serum. .... 105

Figure 3.1 a) A  $^1\text{H}$  NMR image of a 1 cm thick transverse slice of a cat's thorax, ~30 minutes after the instillation of SLS into the left lower lung lobe (upper left). b) The corresponding  $^2\text{H}$  NMR image of the instilled fluid in the cat's left lower lung lobe, as well as two of the projection profiles used to construct the image, acquired ~20 minutes after fluid instillation (upper right). c) The same  $^1\text{H}$  and  $^2\text{H}$  NMR images overlaid for a spatial comparison (bottom). .... 123

Figure 3.2 The averaged ( $n = 4$ ) time course of the  $\text{H}_2\text{O}$  content (black circles) and of the  $\text{D}_2\text{O}$  content (black squares) of a lower lung lobe after instillation of SLS. The data points correspond to averages over a 40

minute data acquisition period centered at the time of the data point.  
The error bars indicate the standard error of the mean. .... 124

Figure 3.3 The averaged ( $n = 4$ ) time course of the  $^1\text{H}$  content (white circles) and of the  $^2\text{H}$  content (white squares) of a lower lung lobe after instillation of SLS plus PAF. The data points correspond to averages over a 40 minute data acquisition period centered at the time of the data point. The error bars indicate the standard error of the mean. .... 125

Figure 3.4 The net clearance time course of instilled alveolar SLS, computed from in-vivo NMR measurements (black circles) and the corresponding gravimetric measurement (black triangle), with error bars indicating the standard error of the mean. The NMR measurements are averages over 40 minute data acquisition periods and over 4 cats. The gravimetric measurement is an average over 5 cats sacrificed at 4 hours post instillation. .... 126

Figure 3.5 The time course of the net clearance of instilled alveolar SLS plus PAF, computed from in-vivo NMR measurements (white circles) and the corresponding gravimetric measurement (white triangle), with error bars indicating the standard error of the mean. The NMR measurements are averages over 40 minute data acquisition periods and over 4 cats. The gravimetric measurement is an average over 5 cats sacrificed at 4 hours post instillation. .... 127

Figure 3.6 A comparison of the time course of the net clearance from the present experiments and from the previous work (25) on net  $^1\text{H}$

clearance. Squares are used to indicate values computed from equation 3.1 from the present combined  $^1\text{H}$  and  $^2\text{H}$  intensity measurements, whereas the circles represent previous results of  $^1\text{H}$  intensity measurements (25). The instillates are represented as follows, SLS (black squares), serum (black circles), SLS plus PAF (white squares), and serum plus PAF (white circles). ..... 129

Figure 3.7 An illustration of the time course of the amount of fluid absorbed from the lung, relative to the amount instilled, calculated from equation 3.2. Absorption of SLS (black circles) and of SLS plus PAF (white circles) are shown. .... 130

Figure 3.8 An illustration of the time course of the amount of fluid secreted into the lung, relative to the amount instilled, calculated from equation 3.3. Fluid secretion after the instillation of SLS (black circles), and after the instillation of SLS plus PAF (white circles), are shown. .... 130

Figure 4.1 The time courses of fluid clearance after the instillation of serum (black circles) and SLS (white circles) and the result of a mathematical model of the lung fluid clearance (solid line). .... 145

Figure 4.2 The time courses of the changes of the  $\text{H}_2\text{O}$  and  $\text{D}_2\text{O}$  contents of the lung after instillation of SLS. The corresponding time courses simulated with a mathematical model of the lung fluid clearance are indicated by the dotted line and the dashed line, respectively. Results of the mathematical model are plotted at 15 minute intervals. .... 146

Figure 4.3 The time courses of fluid clearance after the instillation of serum plus PAF (black circles) and SLS plus PAF (white circles) and the results of a mathematical model of the clearance of serum plus PAF (solid line) and the clearance of SLS plus PAF (dashed line) from the airspaces of the lung. Results of the mathematical model are plotted at 15 minute intervals. .... 147

Figure 4.4 The time courses of the changes of the H<sub>2</sub>O and D<sub>2</sub>O contents of the lung after instillation of SLS plus PAF. The corresponding time courses simulated with a mathematical model of the lung fluid clearance are indicated by the dotted line and the dashed line, respectively. Results of the mathematical model are plotted at 15 minute intervals. .... 148

Figure A1.1.1 Precession of the net magnetization,  $\mathbf{M}_0$ , about an effective magnetic field in the rotating frame of reference,  $\mathbf{B}_{\text{eff}}$ , defined to be along the  $z_p'$  axis..... 158

Figure A1.1.2 Precession of the net magnetization,  $\mathbf{M}_0$ , about an effective magnetic field in the rotating frame of reference,  $\mathbf{B}_{\text{eff}}$ . .... 159

Figure A1.1.3 Definition of the effective magnetic field in the rotating frame of reference. .... 161

Figure A3.2.1 A comparison of the time course of lung water proton transverse relaxation times of the more slowly relaxing component,  $T_{2S}$ , and of the faster relaxing component,  $T_{2F}$ . White circles are used to indicate relaxation times measured after the instillation of SLS plus PAF

whereas the black circles indicate measurements obtained after the instillation of SLS alone. The two time courses of  $T_{2F}$  values illustrated in this figure overlap so that one obscures the other. All measurements are averages over 40 minute data acquisition periods and over 4 cats, with error bars indicating the standard error of the mean. .... 166

### List of Symbols and Abbreviations

2D	two dimensional
$90_x$	$90^\circ$ RF pulse in the $x_p$ direction
$180_x$	$180^\circ$ RF pulse in the $x_p$ direction
$A(t)$	time course of fluid absorption from the airspaces
abs+	additional epithelial fluid absorption caused by PAF
abs_norm	normal epithelial fluid absorption rate
$a_n(t)$	time dependent coefficient of the $n^{\text{th}}$ term of a wave function
ANOVA	analysis of variance
$a_p$	pore area
asd	effective area for solute diffusion through a single pore
asf	area for solute filtration through a single membrane pore
awf	area for water filtration through a single membrane pore
$a_{\text{alb}}$	diameter of an albumin molecule
$a_{\text{water}}$	diameter of a water molecule
$\mathbf{B}$	net external magnetic field vector
$\mathbf{b}$	magnetic field vector due to a magnetic dipole
$\mathbf{B}_1$	externally applied radio-frequency magnetic field vector
$\mathbf{B}_{\text{eff}}$	effective external magnetic field vector, in the rotating frame
$\mathbf{B}_0$	static magnetic field vector
$b_r, b_\theta, b_\phi$	vector components of the magnetic field due to a magnetic dipole, in spherical-polar coordinates
$C$	mean concentration of solutes on two sides of a membrane
$C_+, C_-$	coefficients of $ \alpha\rangle$ and $ \beta\rangle$ to describe a single-spin wave function
cAMP	cyclic-adenosine 3',5' monophosphate
chod_as	alveolar HOD concentration

chod <sub>is</sub>	interstitial HOD concentration
$C_k(t)$	the magnitude of the wave function coefficient, $a_n(t)$
CP	Carr-Purcell NMR pulse sequence
CPMG	Carr-Purcell-Meiboom-Gill NMR pulse sequence
D	distance from the center of a circular object
d	object radius
decay <sub>time</sub>	characteristic decay time of the effect of PAF
DW	dwelt time, the time between sampling successive data points
E	energy
e	electronic charge
$E_{d-d}$	dipole-dipole interaction energy
$E_n$	energy of the $n^{\text{th}}$ nuclear spin state
FID	free induction decay signal
FOV	field of view
FRC	functional residual capacity
FT	Fourier transform
F <sub>end1</sub>	number of endothelial pores of size #1
F <sub>end2</sub>	number of endothelial pores of size #2
F <sub>ep</sub>	number of epithelial pores
g	force of gravity at the earth's surface
$g(r,\phi)$	IFT of a signal intensity projection profile, in polar coordinates
$G(\tau)$	auto-correlation function
$g^*(r,\phi)$	filtered signal intensity projection profile
$G_r$	magnetic field gradient in the radial direction
$G_{x,y,z}$	magnetic field gradients in the x, y, or z directions, respectively
$G_{y\text{max}}$	maximum value of $G_y$ employed in an imaging pulse sequence
$h$	Planck's constant divided by $2\pi$

Hb	hemoglobin
$\mathcal{H}$	Hamiltonian
$\mathcal{H}_{d-d}$	Hamiltonian of the dipole-dipole interaction
$\mathcal{H}_{d-nsec}$	non-secular part of $\mathcal{H}_{d-d}$
$\mathcal{H}_{d-sec}$	secular part of $\mathcal{H}_{d-d}$
$\mathcal{H}_q$	Hamiltonian of the electric quadrupole/ electric field interaction
$\mathcal{H}_{Tot}$	Hamiltonian of the Zeeman plus dipole-dipole interactions
$\mathcal{H}_{Trunc}$	Truncated Hamiltonian given by $\mathcal{H}_z + \mathcal{H}_{d-sec}$
$\mathcal{H}_z$	Hamiltonian of the Zeeman interaction
I	spin quantum number
$\mathbf{I}$	spin angular momentum operator
I	total signal intensity of an image region
$I(\Delta t)$	intensity of an image region after fluid instillation
$I(r, \phi)$	image data in polar coordinates
$I_+, I_-$	raising and lowering operators, respectively
$\mathbf{i}, \mathbf{j}, \mathbf{k}$	unit vectors along the x, y and z axes, respectively
i.d.	inner diameter
$I_{BG}$	NMR signal from a normal lung lobe, the background signal
$I_D(t)$	time course of changes in the deuteron NMR signal intensity
$I_{D-image}(\Delta t)$	total deuteron image intensity, as a function of time
$I_{FF}(\Delta t)$	NMR signal from a fluid filled lung lobe
IFT	inverse Fourier transform
$I_H(t)$	time course of changes in the proton NMR signal intensity
$I_{inst}(\Delta t)$	NMR signal from the instilled fluid in an image region
$I_{mid}$	intensity midway between to object
$I_{Net}(t)$	net fluid clearance time course computed from $I_H(t)$ and $I_D(t)$
$I_o$	intensity of an image region before fluid instillation

$\hat{i}_p, \hat{j}_p, \hat{k}_p$	unit vectors along the $x_p$ , $y_p$ and $z_p$ axes in the rotating frame
$I_{SV}$	deuteron signal intensity measured with a single-voxel acquisition
$J(\omega)$	spectral density function
$J_s$	trans-membrane solute flux
$J_{s\_as}$	solute flux across the epithelium
$J_{s\_is1}$	solute flux across the endothelium through pore size #1
$J_{s\_is2}$	solute flux across the endothelium through pore size #2
$J_v$	trans-membrane fluid flux
$J_{v\_as}$	fluid flux across the epithelium
$J_{v\_is1}$	fluid flux across the endothelium through pore size #1
$J_{v\_is2}$	fluid flux across the endothelium through pore size #2
$K$	membrane conductance
$k$	Boltzmann's constant
$k, k'$	constants
$k_1, k_1', k_1''$	constants
$k_r$	radial k-space coordinate
$k_{x,y,z}$	cartesian coordinates of k-space
$k_{xmax}$	maximum value of $k_x$
$k_{ymax}$	maximum value of $k_y$
$l_p$	membrane fluid permeability
$\mathbf{M}$	net magnetization vector
$m$	an integer
$M(k_x, k_y)$	ensemble magnetization as a function of k-space position
$M(t)$	magnitude of the nuclear magnetization as a function of time
$M_+$	magnetization in the transverse plane
$M_0$	magnitude of the net nuclear magnetization of a spin ensemble
$m_0$	initial amplitude of the magnetization at an isochromat

$M_{x,y,z}$	magnetization components in the x, y, or z directions, respectively
$M_{xy}$	magnetization in the transverse plane
$m_z$	z-component nuclear spin quantum numbers
$N$	number of sample points
$N$	number of signal projections employed for image reconstruction
$N$	number of spins in an ensemble
$n$	an integer
$n$	the number of data points included in an averaged value
$N_\alpha, N_\beta$	relative numbers of spins in the $ \alpha\rangle$ and $ \beta\rangle$ states, respectively
$N(t)$	time course of net fluid clearance from the lung
NMR	nuclear magnetic resonance
o.d.	outer diameter
$p$	probability that two data sets are samples of the same distribution, calculated by a student's t-test
$P_1, P_2$	hydrostatic pressures on sides 1 and 2 of a membrane, respectively
PAF	platelet-activating factor
$p\text{CO}_2$	partial gas pressure due to $\text{CO}_2$
PEEP	positive end-expiratory pressure
$P_{ij}$	transition probability from an energy state $i$ to a state $j$
$p\text{O}_2$	partial gas pressure due to $\text{O}_2$
PSS	physiological saline solution
$P_1$	hydrostatic pressure on side 1 of the membrane
$P_2$	hydrostatic pressure on side 2 of the membrane
$Q$	nuclear electric quadrupole moment
$\dot{Q}_f$	rate of fluid filtration across a membrane
$\dot{Q}_{fas}$	rate of fluid flux across the epithelium
$\dot{Q}_{fis}$	rate of fluid flux across the endothelium

$\dot{Q}_{sas}$	rate of solute flux across the epithelium
$\dot{Q}_{sis}$	rate of solute flux across the endothelium
$q_{hod\_as}$	quantity of HOD in the alveolar space
$q_{hod\_is}$	quantity of HOD in the interstitial space
$Q_{lymph}$	rate of lymph flow out of the interstitial space
$Q_{Nat}$	amount of naturally occurring H <sub>2</sub> O in a portion of a lung
$q_{s\_as}$	quantity of solutes in the alveolar space
$Q_{w-inst}$	amount of H <sub>2</sub> O in the instilled fluid
$r$	regression coefficient
$\underline{r}$	unit vector in the radial direction
$\underline{r}, \underline{\theta}$ and $\underline{\phi}$	axial unit vectors in the spherical-polar coordinate system.
$r, s$ and $\phi$	coordinates $r$ and $s$ in a system at an angle $\phi$ from an $x, y$ system
$R_1$	longitudinal relaxation rate
$R_2$	transverse relaxation rate
$R_{bound}$	relaxation rate of the bound fluid component
$RF$	radio-frequency
$R_{free}$	relaxation rate of the bulk water
$R_{obs}$	the observed relaxation rate
$r_p$	radius of a membrane pore
$S(k_x, k_y)$	NMR signal expressed in k-space coordinates
$S(t)$	time course of fluid secretion into the airspaces
$S(t)$	NMR signal expressed as a function of time
$S(t, \phi)$	signal projection at an angle $\phi$ from the $x$ axis
$sec+$	additional epithelial fluid secretion caused by PAF
$sec\_norm$	normal epithelial fluid secretion rate
$Sin\_as$	solute flux rate into the alveolar space
$Sin\_is$	solute flux rate into the interstitial space

SLS	serum-like solution
$S_0$	NMR signal at time $t = 0$
$S_{out\_as}$	solute flux rate out of the alveolar space
$S_{out\_is}$	solute flux rate out of the interstitial space
$T$	absolute temperature, Tesla
$T_1$	longitudinal relaxation time
$t_{1/2}$	alveolar fluid clearance half-time
$T_2$	transverse relaxation time
$T_2^*$	effective transverse relaxation time
$T_{2F}$	transverse relaxation time of the faster relaxing fluid component
$T_{2S}$	transverse relaxation time of the slower relaxing fluid component
$T_{alv}$	relaxation time of water protons in the alveolar space
$T_{aq}$	signal acquisition duration
$T_{bound}$	relaxation time of the protons in the bound fluid compartment
TE	inter-echo interval
$T_{free}$	relaxation time of the protons in the bulk water
$T_{int}$	relaxation time of water protons in the interstitial space
$T_{obs}$	observed relaxation time
$T_p$	duration of a phase-encoding magnetic field gradient
$T_R$	time between successive applications of a pulse sequence
TTL	transistor-transistor logic
$V(t)$	time varying electric potential
$V(x,y,z)$	electric potential field
$V_D$	the volume of $D_2O$ instilled into a lung lobe
$V_H$	the volume of $H_2O$ instilled into a lung lobe
$V_{inst}$	the total volume instilled into a lung lobe, $V_D + V_H$
$V_{in\_as}$	fluid flux rate into the alveolar space

$V_{in\_is}$	fluid flux rate into the interstitial space
$V_{out\_as}$	fluid flux rate out of the alveolar space
$V_{out\_is}$	fluid flux rate out of the interstitial space
$V_{xx}, V_{yy}, V_{zz}$	second derivatives of $V$ , with respect to $x, y, z$ respectively
$V_{xy}, V_{xz}, V_{yz}$	second derivatives of $V$ , with respect to the subscripted coordinates
$v_{as}$	alveolar fluid volume
$v_{instilled}$	volume of fluid instilled into the alveolar space
$v_{int}$	interstitial fluid volume
$v_{int\_initial}$	interstitial fluid volume of the normal lung
$W_{ij}$	transition probability per unit time from a state $i$ to a state $j$
$X, Y$	dimensions of the field of view
$x_\rho, y_\rho, z_\rho$	cartesian coordinates in the rotating reference frame
$Z$	spatial part of the dipole-dipole Hamiltonian
$ \alpha\rangle,  \beta\rangle$	low and high energy eigenstates of a spin 1/2 nucleus, respectively
$\gamma$	gyromagnetic ratio
$\Gamma$	torque
$\Delta\phi$	angle between successive signal intensity projections
$\Delta G_y$	increment in $G_y$ between successive data acquisition steps
$\Delta k_x, \Delta k_y$	separation of sampled points in $k$ -space
$\Delta r$	distance between two nuclei in a spin ensemble
$\underline{\Delta r}$	unit vector pointing from one nucleus to the other
$\Delta t$	element of time over which fluid and solute fluxes are integrated
$\Delta t$	time from fluid instillation to the mid-point of an image acquisition
$\phi, \varphi$	projection angles from the $x$ axis
$\phi_f, \phi_s$	phases of faster, and slower, precessing spins relative to the $x$ axis
$\eta$	asymmetry parameter used to describe an electric field
$\Phi$	spin part of the dipole-dipole Hamiltonian

$\mu$	vector magnetic moment of a nucleus
$\mu_0$	permeability of free space
$\xi$	magnitude coefficient of $\mathcal{H}_q$
$\Pi_1, \Pi_2$	osmotic pressures on sides 1 and 2 of a membrane, respectively
$\pi_1$	protein osmotic pressure on side 1 of the membrane
$\pi_2$	protein osmotic pressure on side 2 of the membrane
$\pi_{as}$	protein osmotic pressure of the alveolar space fluid
$\pi_{is}$	protein osmotic pressure of the interstitial space fluid
$\theta$	angle of $\mathbf{B}_{eff}$ from $\mathbf{B}_0$ , in the rotating reference frame
$\rho$	local spin density
$\rho_{alv} \ \rho_{int}$	relative fractions of water protons in alveolar and interstitial fluid
$\rho_{bound}$	relative fraction of protons in the bound fluid compartment
$\rho_F$	relative amount of signal from the faster relaxing component
$\rho_{free}$	relative fraction of protons in the bulk water
$\rho_{int}$	relative fraction of protons in the interstitial space
$\rho_s$	relative amount of signal from the more slowly relaxing component
$\sigma$	reflection coefficient of a membrane
$\sigma$	population standard deviation
$\tau$	an interval in time
$\tau_c$	correlation time
$\Psi$	nuclear spin state
$\psi$	nuclear spin eigenstate
$\chi_0$	static nuclear susceptibility
$\lambda$	ratio of the amount of water in a gram of tissue to the amount of water in a gram of blood.
$\Omega$	rotational frequency of the rotating frame of reference

$\omega$	angular frequency
$\omega$	permeability of the membrane to solutes
$\omega_{\text{eff}}$	effective spin angular velocity in the rotating reference frame
$\omega_{jk}$	frequency corresponding to a spin state transition, from state j to k
$\omega_0$	Larmor frequency of a nuclear spin in a static magnetic field, $B_0$

## **1.0 Introduction to the Thesis**

All animals, including man, depend on oxygen-based metabolism which provides cells with the energy to function. For most terrestrial animals the supply of oxygen originates at only one source; the lung, the prime function of which is to match ventilation with perfusion (76). To this end, the lung has a series of branching airways, matched closely by the pulmonary arteries, opening into 300 million alveolar sacs; in the adult human the alveolar surface area of 70 m<sup>2</sup> is in contact with roughly 70 ml of blood in the pulmonary capillaries. The air-blood barrier is only 1.5  $\mu$ m thick, on average, allowing rapid equilibration (< 0.25 sec) of O<sub>2</sub> and CO<sub>2</sub> between the alveolar air and the blood.

While the air-blood barrier of the lung is well adapted to gas exchange, it also provides a large surface area for fluid movement from the capillaries into the alveolar space. This does occur when the alveolar-capillary membrane is damaged, and the alveoli become flooded with fluid. For obvious reasons, the balance of fluid movement across the air-blood barrier of the lung, and the mechanisms which maintain it, have long been a topic of research. With the advent of nuclear magnetic resonance (NMR) imaging, with its sensitivity to the mobile protons in water, came an exciting means of monitoring fluid in the lung, non-invasively. Many of the earliest attempts to observe lung water, either with imaging (18, 20, 35, 46, 65) or magnetization relaxation time measurements (66, 67, 71, 83), however, were only marginally successful because of respiratory motions of the lung, *in-vivo*, and because of strong local magnetic field inhomogeneities caused by magnetic susceptibility differences at air-fluid interfaces. With more recent developments in NMR hardware and measurement techniques, sensitive measurements of magnetization relaxation times have been obtained, *in-vivo*, (68, 69, 70) and images

have provided qualitative observations of the development of pulmonary edema (21, 62).

The original purpose of this project was to improve further upon available  $^1\text{H}$  imaging and relaxation time measurement techniques, specifically for monitoring lung water *in-vivo*, and to monitor the time course of changes of lung water content after a solution simulating protein rich edema fluid was introduced into the alveolar space of the lung. This study explored the mechanisms that keep the alveoli dry. We raised the question of whether fluid was only being absorbed from the alveolar space, or if there was actual bi-directional fluid movement across the air-blood barrier. In an attempt to address this question, a second phase of this project was undertaken in which  $^2\text{H}$  NMR imaging was developed to monitor the alveolar absorption of  $^2\text{H}_2\text{O}$  in a serum-like solution. Inter-leaved with the  $^2\text{H}$  image acquisitions,  $^1\text{H}$  NMR imaging was used, as in the first phase of the study, to monitor the combined effects of fluid absorption from the alveoli and secretion of fluid into the alveoli.

### **1.1 The Air-Blood Barrier of the Lung**

The fluid balance of the lung is governed primarily by the air-blood barrier which, as a result, will be the focus of this thesis. For details of the structure and function of the lung the reader is referred to any one of the books by Staub (76), Levitzky (42), West (82) and Lim (44).

The alveolar-capillary membrane forms the walls of the alveoli which are polygonal in shape with a diameter of approximately 300  $\mu\text{m}$ , and have a total surface area of approximately 100  $\text{m}^2$  in adult humans. The alveolar surface is lined

with surfactant, a phospholipid compound which serves to reduce the alveolar surface tension and facilitates expansion of the alveoli during inhalation. Surfactant also serves to smooth the alveolar surface somewhat by filling in the corners created by junctions of alveolar walls and as a result the alveolar surface more closely describes a sphere. Alveoli are grouped into terminal respiratory units which are normally supplied with air via a single terminal bronchiole, but collateral ventilation from adjacent terminal respiratory units is also available via small openings in the interalveolar septae known as the pores of Kohn. The existence of two or more possible routes of ventilation can greatly influence the alveoli when there is regional edema, particularly if sections of airways are filled with fluid upstream from partially or completely air-filled alveoli.

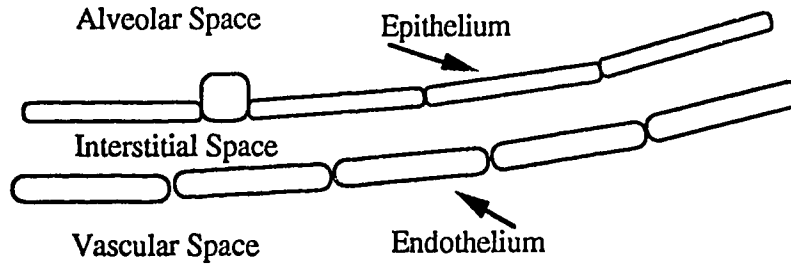


**Figure 1.1** A schematic representation of a portion of the pulmonary air-blood barrier

The surface for gas exchange in the lung, the air-blood barrier, is composed of the alveolar epithelium and its basement membrane, and the pulmonary capillary endothelium and its basement membrane, as indicated in figure 1.1. Two types of cells, in approximately equal numbers, compose the alveolar epithelium; type I cells which are flat, agranular, lining cells covering ~90% of the alveolar surface, and type II cells which are cuboidal and metabolically active. Type II epithelial cells are responsible for the production of surfactant and for maintaining the integrity of the

epithelium by differentiating into both type I and type II cells when required. These epithelial cells are joined by tight junctions and normally form a highly impermeable barrier.

The basement membrane supporting the epithelium is, in places, fused to the basement membrane of the pulmonary capillary which it overlies, and otherwise there is an interstitial space which contains interstitial fluid, fibroblasts, collagen and elastin fibers, and interstitial cells (76). It is generally agreed that the lymphatics, which lie in the interstitial space, extend only to the level of the terminal bronchioles requiring interstitial fluid to be moved from the alveolar septae to the level of the lymphatics by a pressure gradient (51, 75). While the lymphatics play a role in the alveolar fluid balance, the extent of their role in the clearance of edema fluid has been shown to be relatively small and depends somewhat on the protein and solute concentrations in the fluid (52, 75).

The pulmonary capillaries which underlie 70% to 80% of the surface area of the alveolar epithelium, have walls formed by single endothelial cell processes providing a minimal barrier to the diffusion of gases into the blood. Junctions between these endothelial cells are not as tight as those between the alveolar epithelial cells and the capillaries are likely the main source of interstitial fluid and solutes (51). The diameter of the capillaries is such that red blood cells must pass through in single file, maximizing the exposure of each red blood cell to the air-blood barrier. The supply of blood to the alveoli depends both on gravity and the flow resistance of the supplying arterioles which can be varied by changing the tone of the smooth muscle in the arteriole walls. The pulmonary blood supply is reduced to alveoli which are poorly ventilated, resulting in an increase in the blood supply to better ventilated areas, thereby serving the lung's prime function which is the

matching of ventilation to perfusion (76). There are, however, a number of mechanisms responsible for matching ventilation to perfusion.

## **1.2 The Pulmonary Fluid Balance**

The maintenance of "dry" alveoli for gas exchange requires a delicate balance between the mechanisms affecting fluid pressures on each side of the air-blood barrier. Classically, the filtration of fluid across the air-blood barrier has been described solely in terms of hydrostatic and osmotic pressures. This model was proposed by Starling in 1896 for fluid filtration across a semipermeable membrane, in what has become known as the Starling equation:

$$(1.1) \quad \dot{Q}_f = K[(P_2 - P_1) - \sigma(\Pi_2 - \Pi_1)]$$

Here  $\dot{Q}_f$  represents the rate of fluid filtration across the membrane and is positive when the flow is from side 1 to side 2 of the membrane,  $K$  is the membrane conductance,  $P_1$  and  $P_2$  are the hydrostatic pressures on sides 1 and 2 of the membrane, respectively. The reflection coefficient of the membrane to osmotically active particles is  $\sigma$  which has values of 1 for an impermeable membrane and 0 for a permeable membrane.  $\Pi_1$  and  $\Pi_2$  are the osmotic pressures on sides 1 and 2 of the membrane, respectively. In applying this equation to the capillary endothelium only protein osmotic pressures need to be considered because this membrane is relatively permeable to solutes. For the alveolar epithelium, however, both proteins and solutes must be taken into account because of the relative impermeability of this membrane.

The Starling equation has proven to be very useful in describing the development of hydrostatic pulmonary edema, in which the pulmonary capillary pressure is greatly elevated, and the development of increased permeability pulmonary edema in which the capillary endothelium is damaged thereby increasing the membrane conductance. Both of these situations lead to an increased fluid flux into the interstitial space resulting in interstitial edema, and if the interstitial pressure becomes sufficiently elevated, or the alveolar epithelium is also damaged, fluid will move into the alveolar space resulting in alveolar edema as well. The pathogenesis of pulmonary edema is often characterized by the protein concentration of the edema fluid relative to that of plasma with a ratio of  $<0.65$  indicating that hydrostatic pressure is the primary cause and a ratio of  $>0.75$  indicating that the edema is primarily due to an increase in membrane permeability (53). What the Starling equation fails to describe, however, is how alveolar fluid is cleared from the lung after the hydrostatic pressure is reduced to normal or the capillary membrane is repaired and once again becomes impermeable.

In a variety of studies investigating the clearance of fluid and protein from the alveolar space it was observed that fluid is cleared from the lung much more rapidly than albumin. In dogs, sheep, and rabbits, it was observed that blood serum or plasma fluid was cleared from the alveoli with clearance half-times ( $t_{1/2}$ ) of 18 hours, 9 hours and 6 hours, respectively, and that albumin was cleared at a rate of only ~1% per hour (9, 50, 73). The result of these vastly different fluid and albumin clearance rates is that, over time, albumin is concentrated in the alveolar space producing a large osmotic pressure gradient favoring fluid movement into the airspaces. In spite of this pressure gradient, however, the clearance of fluid from the airspaces proceeds, and this led Matthay et al. (50) to propose that active

electrolyte transport might be an important mechanism of fluid clearance from the alveoli.

The active transports of  $\text{Na}^+$ ,  $\text{Cl}^-$  and  $\text{K}^+$  ions have been observed in excised lungs at the levels of the trachea and the subsegmental bronchi (14, 23, 59). Moreover, angiotensin II was observed to stimulate active  $\text{Cl}^-$  secretion by cultured tracheal epithelial cells (79). Alveolar type II epithelial cells grown in culture were observed to form fluid domes, indicating that these cells are actively transporting electrolytes with water following passively (31). Inhibitors of  $\text{Na}^+$  transport such as amiloride and ouabain, and a low  $\text{Na}^+$  medium were each observed to inhibit the dome formation, while  $\text{Cl}^-$  transport inhibitors, such as furosemide, or the removal of  $\text{Cl}^-$  or  $\text{K}^+$  from the medium had no effect on dome formation (32, 77) indicating that the domes were formed as a result of  $\text{Na}^+$  transport from the apical to the basolateral side of the epithelial cells. Also, a variety of factors such as  $\beta$ -adrenergic agonists, cAMP analogues and phosphodiesterase inhibitors were observed to increase dome formation, indicating that, if active  $\text{Na}^+$  transport is important to fluid clearance *in-vivo*, it may be affected by nervous stimulation or the supply of intracellular cAMP (33, 49).

In an effort to determine if the active electrolyte transport observed in cultured epithelial cells is a significant mechanism for clearing fluid from the alveolar space, Basset et al. carried out a series of experiments on isolated rat lungs which were perfused with Ringer's solution, and had Ringer's solution instilled into the airspaces (3, 4). They observed both passive  $\text{Na}^+$  movements, assumed to be paracellular, and active  $\text{Na}^+$  transport across the alveolar epithelium via  $\text{Na}^+$  channels and a  $\text{Na}^+$ -D-glucose symport across the luminal cell membrane, as well as a  $\text{Na}^+$ - $\text{K}^+$  pump across the abluminal membrane. Also, they observed that there

may be a luminal  $\text{Na}^+\text{-K}^+$  pump as well, suggesting that two types of epithelial cells actively transport electrolytes as it is unlikely that one cell would have both luminal and abluminal  $\text{Na}^+\text{-K}^+$  pumps (19). More recently, similar results were observed *in-vivo* when Smedira et al. (73) instilled plasma into the airspaces of anesthetized rabbits and demonstrated that 75% of the fluid clearance could be inhibited with the addition of amiloride to the instillate. Also, Berthiaume stimulated  $\text{Na}^+$  transport across alveolar epithelial cells in anesthetized sheep by raising lung tissue cAMP levels, and as a result observed an increased lung fluid clearance (10).

The clearance of protein from the alveolar space presented even more of a puzzle than the fluid clearance as albumin was observed to be cleared from the lungs of anesthetized animals at a rate of  $\sim 1\%$ /hour and yet the tight epithelium was intact and considered impermeable to macromolecules (9). In 1947 Drinker et al (22) proposed that proteins must be broken down by enzymes into fragments small enough to cross the epithelium. This view held until 1967 when Bensch et al. (5) observed that the lung can absorb intact proteins. Bensch et al. later expanded these findings when they observed that macromolecules can be transported to the capillary blood by pinocytotic vesicles in type I epithelial cells and capillary endothelial cells and that the lymphatics play only a minor role in the protein clearance from the lung (6).

All of the above studies indicate that in addition to hydrostatic and osmotic forces, the pulmonary fluid balance is also affected by the active transport of ions and macromolecules across the alveolar epithelium. Under normal circumstances the lung must require a balance between all of these mechanisms to maintain a steady state of "dry" alveoli. The development of lung edema likely depends, for the most part, on hydrostatic and osmotic pressures as it has been shown that fluid

absorption mechanisms become inoperative if the normally high reflection coefficients for  $\text{Na}^+$  and  $\text{Cl}^-$  are lowered (4). The clearance of edema fluid during the recovery from a pathological state, however, is likely dominated by the active transport mechanisms that have been demonstrated across the air-blood barrier of the lung.

Platelet-activating factor (PAF) is a family of ether-lipids whose active component is 1-O-Hexadecyl/octadecyl-2-acetyl-sn-glycero-3-phosphocholine and is produced by a wide variety of cells in the body including alveolar type II epithelial cells (36, 37, 58, 63). It has been shown that intra-airway PAF can cause bronchoconstriction, inflammation in the airways and capillary spaces, and pulmonary neutrophil sequestration (11, 78, 80). The effects of PAF on the clearances of alveolar fluid and protein are addressed in this thesis because this agent is suspected of playing roles in asthma and in sarcoidosis, and the role of PAF in the development and/or resolution of pulmonary edema has not been previously evaluated (2, 64).

### **1.3 NMR Studies of Lung Water**

#### **1.3.0 A brief historical overview**

The means by which an image of an object can be formed from an NMR signal was first described in 1973 by Lauterbur (40) and, independently, by Mansfield and Grannell (47). Three years later Lauterbur (41) and Frank (27) concluded that it may be feasible to use NMR imaging to detect pulmonary edema when they observed a linear relationship between the longitudinal relaxation rate and the dry weight to wet weight ratio of lung tissue. Since that time a variety of

studies have been carried out showing that both longitudinal ( $T_1$ ) and transverse ( $T_2$ ) relaxation times increase with increasing lung water (62, 66, 67, 71, 83) and that relaxation times can be used to differentiate between hydrostatic and permeability edema types (66). The NMR signal intensity has also been used to detect regional edema and it has been shown to be well correlated with the extravascular lung water content under a variety of conditions (18, 20, 35, 46, 65).

All of these in-vivo studies suffered, however, from the typically low signal to noise ratio obtained from the lung because of the paucity of water protons in the normal lung, short transverse relaxation times, plus cardiac and respiratory motions. The means to reduce the detrimental effects of these properties began to develop as an understanding of the NMR properties of lung water, and more sophisticated NMR hardware, were developed. For example, it was determined that air-water interfaces in the lung can cause local magnetic field gradients due to magnetic susceptibility differences across the interface, and that these local gradients enhance transverse relaxation effects. However, the effects of local magnetic field gradients can under most circumstances be reversed with an NMR pulse sequence, which will be discussed in section 1.3.3. Further understanding of the relaxation mechanisms which are dominant in the lung was provided by the observations of Kveder et al (38). Firstly, they observed that lung water underwent fairly restricted movement and diffused much more slowly than free water. Secondly, they observed that water proton relaxation in the lung is influenced by the rapid exchange of water between a free state, and a state in which it is bound to biopolymer segments at the lung tissue surface. As a result, Kveder et al. postulated that longitudinal relaxation rates of lung water protons should be proportional to the lung tissue surface area (39). Moreover, for improving the quality of lung images various techniques for respiratory gated signal acquisition have been described (24).

Also, Phillips et al. have proposed that the optimal NMR pulse sequence for lung imaging and relaxation time measurements is a spin-echo sequence which includes respiratory gated signal acquisition with regular radio-frequency excitation pulses to maintain a steady state (spin-conditioning), and excludes cardiac gated signal acquisition (61, 62).

Making use of these developments in NMR techniques, Phillips et al. were able to observe the changes in relaxation times that occurred as permeability edema developed *in-vivo* (62). Moreover, Shioya et al. were able to achieve a high enough signal to noise ratio to observe the bi-exponential transverse relaxation of water protons in normal lung tissue *in-vivo*, and therefore to measure the transverse relaxation times of two distinct fluid components in the lung (68, 69, 70). Although much progress has been made in the use of NMR for the study of lung edema, the bulk of the studies that have been carried out were aimed at demonstrating that some property of the NMR signal or some technique could be useful for detecting and monitoring edema. Of the studies that had been done prior to this project, only four had actually involved monitoring extravascular lung water or one of its properties for a period of time (21, 62, 67, 70).

The capabilities of current NMR hardware and techniques, for both clinical and research applications, are demonstrated by the following examples. Firstly, recent developments of a projection reconstruction technique for reducing the effects of motion and magnetic susceptibility differences, have enabled the acquisition of images which demonstrate the large blood vessels and bronchi in the lung (7). Magnetic resonance imaging has been shown to detect experimentally induced changes in the lung ventilation and perfusion distributions in an anesthetized animal, with the administration of intra-airway and intravenous contrast

agents (8). Clinically, magnetic resonance imaging has been shown to depict the presence or absence of hilar lymph nodes, and to demonstrate differences between patients with and without *Pneumocystis carinii* pneumonia (54, 81). Moreover, NMR imaging has been shown to be useful for the characterization of pleural fluid and is able to distinguish pleural effusion from parenchymal disease and from pleural tumors (56). Relaxation time measurements, and relaxation time weighted imaging, have also demonstrated differences in pleural effusions, as well as demonstrating the extent of chest wall invasion by lung tumors, and the presence of bronchogenic carcinoma and distal airway collapse (54, 56, 81). While the ability to characterize regions of increased signal intensity in, or adjacent to, the lung is well demonstrated by these studies, we have found no clinical NMR studies concerning the quantification of extravascular lung water discussed in the literature.

### 1.3.1 Macroscopic Nuclear Magnetization

The induction of nuclear magnetization in a spin ensemble by means of an external magnetic field requires only that one or more species of nuclei comprising the system have magnetic moments. The nuclear magnetic moment,  $\mu$ , is related to the nuclear spin,  $I$ , by the equation

$$(1.2) \quad \mu = \gamma \hbar I$$

where  $\gamma$  is the gyromagnetic ratio and is unique for each nuclear species, and  $\hbar$  is Planck's constant divided by  $2\pi$ . The interaction between the magnetic moment of a nucleus,  $\mu$ , and the external magnetic field,  $B_0$ , known as the Zeeman interaction, has a Hamiltonian,  $\mathcal{H}_Z$ , given by

$$(1.3) \quad \mathcal{H}_z = - \mu \cdot \mathbf{B}_0$$

Taking  $\mathbf{B}_0$  to be along the z axis, and substituting for  $\mu$  from equation 1.2, results in equation 1.4.

$$(1.4) \quad \mathcal{H}_z = - \gamma \hbar B_0 I_z$$

where  $I_z$  denotes the z component of the nuclear spin. Substituting this Hamiltonian into the Schroedinger equation yields a solution with  $2I+1$  stationary eigenstates with energies,  $E$ , given by

$$(1.5) \quad E = - \gamma \hbar B_0 m_z$$

where  $m_z$  represents the eigenvalues of the operator  $I_z$ , and has values  $-I, -I+1, \dots, I-1, I$ . For a spin  $I = 1/2$  nucleus there are two energy eigenstates, identified by their orthonormal eigenfunctions  $|\alpha\rangle$  and  $|\beta\rangle$ , corresponding to  $m_z$  values of  $1/2$  and  $-1/2$ , respectively. In the general case, however, the spin state of a nucleus cannot be described by one or the other of these energy eigenfunctions, but rather is an admixture of the two.

For an ensemble of non-interacting nuclear spins in thermal equilibrium, the relative number of spins in each energy state is given by a Boltzmann distribution with more spins in the lower energy states than in the higher energy states. In the case of spin  $I = 1/2$  nuclei, the number of spins in state  $|\beta\rangle$ ,  $N_\beta$ , relative to the number in state  $|\alpha\rangle$ ,  $N_\alpha$ , is

$$(1.6) \quad (N_\beta/N_\alpha) = \exp\left[\frac{-\Delta E}{kT}\right]$$

where

$$(1.7) \quad \Delta E = E_{\beta} - E_{\alpha} = \gamma \hbar B_0$$

In equation 1.6,  $k$  is Boltzmann's constant and  $T$  is the absolute temperature. The population difference between these two energy states results from the probability of finding a spin aligned parallel to  $B_0$  being greater than that of finding it antiparallel to  $B_0$ , and for an ensemble of  $N$  spins results in a net  $z$ -component magnetization given by

$$(1.8) \quad M_z = \gamma \hbar \sum_{\text{all spins}} \langle I_z \rangle$$

where  $\langle I_z \rangle$  denotes the expectation value of  $I_z$  for a single nuclear spin. For an ensemble of  $N$  spins in thermal equilibrium, the net  $z$ -component magnetization has magnitude  $M_0$  (1)

$$(1.9) \quad M_0 = N \gamma^2 \hbar^2 I(I+1) B_0 / 3kT = \chi_0 B_0$$

In this expression  $\chi_0$  is known as the static nuclear susceptibility. In thermal equilibrium, there is no preferred direction for the transverse component of an individual spin magnetic moment, and all transverse spin component orientations can be found with equal probability. As a result, the transverse magnetization components,  $M_x$  and  $M_y$ , are zero and there is no detectable NMR signal. (The detection of the NMR signal is discussed later in this section.) However, in the general case

$$(1.10) \quad M_x = \gamma \hbar \sum_{\text{all spins}} \langle I_x \rangle$$

$$(1.11) \quad M_y = \gamma \hbar \sum_{\text{all spins}} \langle I_y \rangle$$

In these expressions  $\langle I_x \rangle$  and  $\langle I_y \rangle$  denote the expectation values of  $I_x$  and  $I_y$  for a single nuclear spin. Alternatively, one can combine equations 1.10 and 1.11, and substitute the raising operator,  $I_+$ , for  $I_x + i I_y$ , to obtain the expression for the transverse magnetization of the spin ensemble,  $M_+$ , in equation 1.12.

$$(1.12) \quad M_+ = \gamma \hbar \sum_{\text{all spins}} \langle I_+ \rangle$$

Because a nuclear spin state can generally be described by an admixture of its energy eigenfunctions, the spin ensemble expectation values of  $I_x$ ,  $I_y$ , and  $I_+$ , can be non-zero when the spin system is not in thermal equilibrium. For example, the single spin state  $\psi$ , can generally be written

$$(1.13) \quad \psi = C_+ |\alpha\rangle + C_- |\beta\rangle$$

subject to the condition that

$$(1.14) \quad C_+^2 + C_-^2 = 1$$

The expectation value  $\langle I_+ \rangle$  can then be computed as shown in equations 1.15 to 1.19, with the use of Dirac notation (43). Firstly,  $\langle I_+ \rangle$  is given by

$$(1.15) \quad \langle I_+ \rangle = \langle \psi | I_+ | \psi \rangle$$

(43) and substituting for  $\psi$  from equation 1.13 gives

$$(1.16) \quad \langle I_+ \rangle = \langle \psi | I_+ | (C_+ | \alpha \rangle + C_- | \beta \rangle)$$

Applying the raising operator then yields

$$(1.17) \quad \langle I_+ \rangle = \langle \psi | C_- | \alpha \rangle$$

and substituting for  $\psi$  from equation 1.13 results in the expression

$$(1.18) \quad \langle I_+ \rangle = (C_+^* \langle \alpha | + C_-^* \langle \beta |) C_- | \alpha \rangle$$

where  $*$  denotes the complex conjugate. Because  $| \alpha \rangle$  and  $| \beta \rangle$  are orthogonal and normalized, equation 1.18 can be simplified further to the expression

$$(1.19) \quad \langle I_+ \rangle = C_+^* C_-$$

As a result, the quantum mechanical treatment of the nuclear spin interaction with a magnetic field can be used to describe the net transverse magnetization,  $M_+$  (equation 1.12), of a spin ensemble and is not limited to describing magnetization which is parallel or antiparallel to a static  $B_0$  field.

To describe the motion of the net magnetization,  $\mathbf{M}$ , of an ensemble of spins in any external magnetic field, Felix Bloch (12) used a phenomenological approach to develop a set of equations that turn out to be valid for most biomedical applications of NMR because of the highly fluid state of animal tissue. In low viscosity liquids such as water, extracellular fluid, or plasma for example, the magnetic field that a spin experiences due to adjacent spin magnetic moments averages to zero over time because of the random thermal motions of the spins, and the system magnetization approaches its equilibrium value exponentially as assumed by Bloch. The basis of Bloch's approach is that a magnetic moment,  $\mu$ , interacting with a magnetic field,  $\mathbf{B}$ , will experience a torque given by

$$(1.20) \quad \mathbf{\Gamma} = \mu \times \mathbf{B}$$

Substituting the rate of change of the spin angular momentum,  $\hbar \mathbf{I}$ , for the torque,  $\mathbf{\Gamma}$ , yields

$$(1.21) \quad \hbar \frac{d\mathbf{I}}{dt} = \mu \times \mathbf{B}$$

With the additional substitution of  $\mu/\gamma\hbar$  for  $\mathbf{I}$ , from equation 1.2, gives

$$(1.22) \quad \frac{1}{\gamma} \frac{d\mu}{dt} = \mu \times \mathbf{B}$$

$$(1.23) \quad \frac{d\mu}{dt} = \gamma\mu \times \mathbf{B}$$

In order to apply this same treatment to a spin ensemble, one can substitute for the magnetic moment  $\mu$ , its expectation value  $\langle\mu\rangle$  (72). Furthermore, if the spins in the ensemble can be thought of as not interacting with one another, equation 1.23

holds true for the magnetic moment per unit volume, i.e. the total magnetization of the spin system,  $\mathbf{M}$  (72). The substitution of  $\mathbf{M}$  for  $\boldsymbol{\mu}$  in equation 1.23 results in the expression

$$(1.24) \quad \frac{d\mathbf{M}}{dt} = \gamma \mathbf{M} \times \mathbf{B}$$

Without a loss in generality one can define the z axis of the coordinate system to be parallel to  $\mathbf{B}$ . The solution of the differential equation 1.24 is then that the x and y components of  $\mathbf{M}$  precess about the z axis at a frequency  $\omega_0$ , called the Larmor frequency, which is equal to  $-\gamma B$ .

Because the spin ensemble magnetization precesses about an externally applied magnetic field, the interaction between  $\mathbf{M}$  and  $\mathbf{B}$  is much easier to describe in a reference frame which is rotating about the z axis at the frequency  $\omega_0$ . To allow for the more general case, however, we describe this interaction in a reference frame rotating about the z axis at a frequency  $\Omega$ , and then investigate the special case in which  $\Omega = \omega_0$ . In differentiating  $\mathbf{M}$  with respect to time in a rotating frame, it is necessary to allow for the general case in which the orthogonal unit vectors  $\mathbf{i}$ ,  $\mathbf{j}$ , and  $\mathbf{k}$  may be rotating with an instantaneous angular velocity  $\Omega \mathbf{k}$  (72). In this case, the transformation from the laboratory frame to the rotating frame proceeds as follows. Firstly,

$$(1.25) \quad \frac{d\mathbf{M}}{dt} = \mathbf{i} \frac{dM_x}{dt} + \mathbf{j} \frac{dM_y}{dt} + \mathbf{k} \frac{dM_z}{dt} + M_x \frac{d\mathbf{i}}{dt} + M_y \frac{d\mathbf{j}}{dt} + M_z \frac{d\mathbf{k}}{dt}$$

and in a rotating frame the time derivative of a unit vector is given by

$$(1.26) \quad \frac{d\mathbf{i}}{dt} = \boldsymbol{\Omega} \times \mathbf{i}$$

with similar expressions for the derivatives of the  $\mathbf{j}$  and  $\mathbf{k}$  unit vectors. Substituting expressions for  $d\mathbf{i}/dt$ ,  $d\mathbf{j}/dt$  and  $d\mathbf{k}/dt$  into equation 1.25 and simplifying, yields

$$(1.27) \quad \frac{d\mathbf{M}}{dt} = \frac{\delta\mathbf{M}}{\delta t} + \boldsymbol{\Omega} \times \mathbf{M}$$

Now by substituting for  $\frac{d\mathbf{M}}{dt}$  from equation 1.24 results in the expression

$$(1.28) \quad \frac{\delta\mathbf{M}}{\delta t} = \gamma\mathbf{M} \times \mathbf{B}_0 - \boldsymbol{\Omega} \times \mathbf{M}$$

which can be rearranged to give

$$(1.29) \quad \frac{\delta\mathbf{M}}{\delta t} = \gamma\mathbf{M} \times (\mathbf{B}_0 + \boldsymbol{\Omega}/\gamma)$$

With the introduction of an effective magnetic field in the rotating frame,  $\mathbf{B}_{\text{eff}}$ , defined by

$$(1.30) \quad \mathbf{B}_{\text{eff}} = \mathbf{B}_0 + \boldsymbol{\Omega}/\gamma$$

equation 1.29 is reduced to

$$(1.31) \quad \frac{\delta\mathbf{M}}{\delta t} = \gamma\mathbf{M} \times \mathbf{B}_{\text{eff}}$$

Depending on the magnitude and sense of  $\Omega$ ,  $\mathbf{B}_{\text{eff}}$  can be larger or smaller than  $\mathbf{B}_0$ . In the on-resonance case the reference frame rotates at the angular velocity of the precessing magnetization,  $\mathbf{M}$ , as described by equation 1.32. Thus, in the on-resonance rotating frame the effects of the  $\mathbf{B}_0$  field are nullified and the magnetization appears to be static, as described by equation 1.33.

$$(1.32) \quad \Omega = \omega_0 = -\gamma B_0$$

$$(1.33) \quad \frac{\delta \mathbf{M}}{\delta t} = 0$$

If one superimposes onto the static  $\mathbf{B}_0$  field an RF field,  $\mathbf{B}_1$ , which is directed along the  $x_p$  axis in the rotating frame, and  $\Omega$  is chosen to be the same as the rotational frequency of the  $\mathbf{B}_1$  field, the resultant effective field becomes

$$(1.34) \quad \mathbf{B}_{\text{eff}} = (B_0 + \Omega/\gamma) \mathbf{k}_p + B_1 \mathbf{i}_p$$

Where the unit vectors  $\mathbf{i}_p$ ,  $\mathbf{j}_p$  and  $\mathbf{k}_p$  are along the  $x_p$ ,  $y_p$  and  $z_p$  axes, respectively. Substituting equation 1.34 into equation 1.31 now yields the new equation of motion in the rotating reference frame:

$$(1.35) \quad \frac{\delta \mathbf{M}}{\delta t} = \gamma \mathbf{M} \times [(B_0 + \Omega/\gamma) \mathbf{k}_p + B_1 \mathbf{i}_p]$$

As a result, the magnetization,  $\mathbf{M}$ , precesses about the new effective field in the rotating frame at a frequency,  $\omega_{\text{eff}}$ , given by equation 1.36 and as shown schematically in figure 1.2.

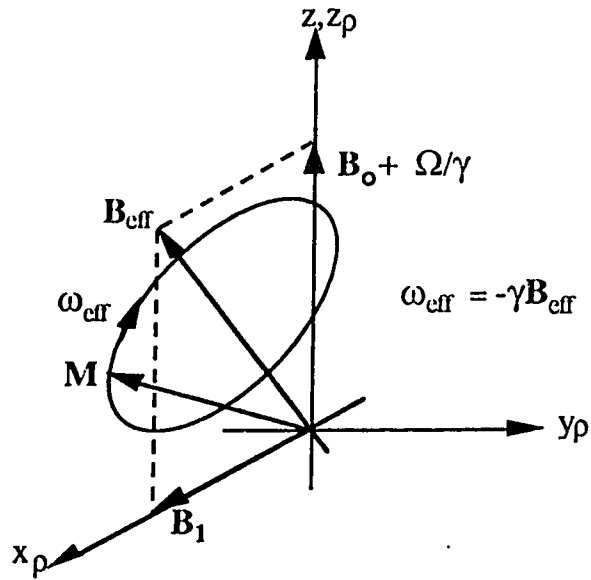


**Figure 1.2** Motion of a system of non-interacting spins in a frame of reference rotating at angular velocity  $\Omega$  in the presence of an applied field,  $\mathbf{B}_1$ , rotating at angular velocity  $\Omega$ . The system was initially at thermal equilibrium with a net magnetization,  $\mathbf{M}$ , along the  $z$  axis.

$$(1.36) \quad \omega_{\text{eff}} = \gamma[(B_0 + \Omega/\gamma)\mathbf{k}_p + B_1 \mathbf{i}_p] = \gamma\mathbf{B}_{\text{eff}}$$

In the special case in which the  $\mathbf{B}_1$  field is on-resonance,  $\Omega = -\omega_0$ , the effective field in the rotating frame is equal to  $B_1 \mathbf{i}_p$  and the magnetization precesses in the  $y_p z_p$  plane as shown in figure 1.3.

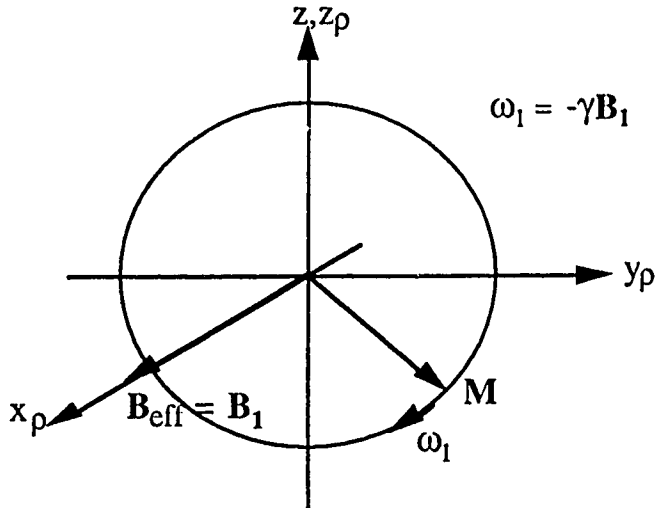


**Figure 1.3** Motion of a system of non-interacting spins in a frame of reference rotating at angular velocity  $\Omega = -\gamma B_0$  in the presence of an applied field,  $B_1$ , rotating at angular velocity  $\Omega$ . The system was initially at thermal equilibrium with a net magnetization,  $M$ , along the  $z$  axis.

As illustrated in figures 1.2 and 1.3, if the  $B_1$  field rotates at a frequency near  $\omega_0$  and is applied for the appropriate duration, the magnetization can be rotated  $90^\circ$  from the  $z$  axis into the  $x_p y_p$  plane. In practice, only brief pulses of the  $B_1$  field, on the order of  $1 \mu s$  to hundreds of  $\mu s$ , are required to rotate the ensemble magnetization through  $90^\circ$  and so pulses of this type are referred to as  $90^\circ$  RF pulses. Only when the  $B_1$  field is on-resonance as depicted in figure 1.3, can the magnetization be rotated (with a  $180^\circ$  RF pulse) from the  $+z$  axis to the  $-z$  axis. The general expressions for the magnitude of the magnetization components in the  $x_p y_p$  plane and along the  $z$  axis after an RF pulse of duration  $t$  are shown in equations 1.40 and 1.41. The derivation of these expressions is included in Appendix 1.1.

$$(1.3') \quad B_{\text{eff}} = [(B_0 + \Omega/\gamma)^2 + B_1^2]^{1/2}$$

$$(1.38) \quad \sin\theta = \frac{B_1}{B_{\text{eff}}}$$

$$(1.39) \quad \cos\theta = \frac{(B_0 + \Omega/\gamma)}{B_{\text{eff}}}$$

$$(1.40) \quad M_{xy} = M_0 \sin\theta [\cos^2\theta (1 + \cos(\gamma B_{\text{eff}} t))^2 + \sin^2(\gamma B_{\text{eff}} t)]^{1/2}$$

$$(1.41) \quad M_z = M_0 [\cos^2\theta - \sin^2\theta \cos(\gamma B_{\text{eff}} t)]$$

These equations demonstrate that by applying an on-resonance RF field,  $B_1$ , for the appropriate duration,  $t$ , the magnetization of a spin system can be rotated through any desired angle about  $B_1$ . The means to manipulate the spin system magnetization in this way is employed in all NMR applications, and is an integral part of the NMR imaging theory discussed in section 1.3.3.

Bloch also introduced into the equation of motion of  $\mathbf{M}$ , two terms to describe the relaxation of the magnetization back to thermal equilibrium, subject to the conditions that inter-nuclear interactions are weak and that the major cause of relaxation is thermal agitation of the spins (12). The first of these terms describes magnetization relaxation in the longitudinal direction, parallel to  $B_0$ , whereas the second term describes relaxation of the transverse component magnetization, normal to  $B_0$ . The longitudinal component of the magnetization,  $M_z$ , was assumed by Bloch to approach its thermal equilibrium value of  $M_0$  exponentially with a characteristic time,  $T_1$ , as described by the differential equation

$$(1.42) \quad \frac{dM_z}{dt} = - \frac{M_z - M_0}{T_1}$$

The transverse magnetization was similarly assumed by Bloch to return to its equilibrium value of zero, exponentially with a characteristic time,  $T_2$ , so that the rate of change of  $M_x$  and of  $M_y$  are described by the equations

$$(1.43) \quad \frac{dM_x}{dt} = -\frac{M_x}{T_2}$$

$$(1.44) \quad \frac{dM_y}{dt} = -\frac{M_y}{T_2}$$

Bloch then assumed that the effects of nuclear relaxation could be superimposed on the motions of the spins due to externally applied magnetic fields, to yield a general equation of motion for a system of weakly interacting nuclear magnetic moments such as in a liquid (equation 1.45).

$$(1.45) \quad \frac{d\mathbf{M}}{dt} = \gamma \mathbf{M} \times \mathbf{B} - \frac{(M_z - M_0)\mathbf{k}}{T_1} - \frac{(M_x\mathbf{i} + M_y\mathbf{j})}{T_2}$$

Equation 1.45 enables one to describe the interaction between the macroscopic nuclear magnetization and externally applied magnetic fields in most biological systems. Also, this equation can describe the basic NMR experiment in which a  $90^\circ$  RF pulse is applied to rotate the magnetization of a spin ensemble from thermal equilibrium into the transverse plane. As the resultant transverse component of the magnetization relaxes back to thermal equilibrium it also precesses about the static  $B_0$  field. If this precessing magnetization is linked by a receiver coil, it will induce in the coil an oscillating electromotive force (EMF), which in turn will produce a time varying potential difference,  $V(t)$ , across a load at the output of the coil. It is this potential difference,  $V(t)$ , that is the NMR signal. Descriptions of the NMR hardware and methods of producing static and RF magnetic fields, and detecting the

NMR signal have been provided in great detail by a variety of authors and so will not be repeated here (1, 28, 72).

### 1.3.2 Magnetization Relaxation Processes

The longitudinal relaxation of nuclear magnetization back to thermal equilibrium, parallel to the static  $B_0$  field, is also known as "spin-lattice" relaxation. The term "spin-lattice" is used because this relaxation is due to a transfer of energy from the excited spins to the thermal energy of the surrounding medium, termed the "lattice". Transverse relaxation, on the other hand, is also known as "spin-spin" relaxation. In this case "spin-spin" refers to the interaction between spin magnetic moments and adjacent spin magnetic moments or paramagnetic ions. Bloch (12) however, used an all encompassing description of transverse relaxation as being due to inter-nuclear interactions, interactions with paramagnetic ions, and with inhomogeneities in the static  $B_0$  field. The random interactions between a nuclear spin and another spin or a paramagnetic ion, cause both a change in the transverse components of the spin expectation values and a loss of coherence of their precession, leading to an irreversible decay of the transverse magnetization towards its equilibrium value of zero. This decay is characterized by the time  $T_2$ . Static field inhomogeneities, however, result in a dephasing of the transverse magnetization components which is spatially dependent and (in the absence of rapid diffusion) is reversible. Because the transverse relaxation described by Bloch includes effects of the static  $B_0$  field inhomogeneities, it is characterized by the relaxation time  $T_2^*$  which is less than or equal to the natural  $T_2$  of the spin system.

For the purposes of this thesis only two nuclear species are of interest, namely, the proton and the deuteron, and so the following discussions of nuclear

relaxation will be limited to these nuclei. For the spin  $I = 1/2$  proton, relaxation is dominated by the magnetic interaction between adjacent dipole moments, known as the dipole-dipole interaction. The deuteron, on the other hand, has a spin of 1 and so has an electric quadrupole moment which can interact with a local electric field gradient. For deuterons in a liquid-like system it is this quadrupolar interaction which dominates the nuclear relaxation.

### Dipole-Dipole Relaxation

The relaxation process which has been termed dipole-dipole relaxation is driven by the interaction between a spin magnetic dipole moment and local time dependent magnetic fields which are due to adjacent spin magnetic moments or paramagnetic ions. The time dependent nature of these local magnetic fields is provided by the random thermal motions of the spins, and by the natural flip rate of the ionic spins. It is the magnetic coupling of adjacent spin magnetic moments that provides a means of transferring energy between spins, and from spins to the thermal lattice so that the spin system and the lattice can approach a common thermal equilibrium.

The spin wave function for a two spin system in a static magnetic field, similar to that for the single spin system (equation 1.13), can be described as a linear combination of the following stationary eigenstates of the Zeeman Hamiltonian (equation 1.3):

$$(1.46) \quad \psi_1 = |\alpha\alpha\rangle$$

$$(1.47) \quad \psi_{0,s} = \frac{1}{\sqrt{2}}[|\alpha\beta\rangle + |\beta\alpha\rangle]$$

$$(1.48) \quad \psi_{0,A} = \frac{1}{\sqrt{2}}[|\alpha\beta\rangle - |\beta\alpha\rangle]$$

$$(1.49) \quad \psi_{-1} = |\beta\beta\rangle$$

Moreover, transition selection rules do not permit the system to undergo transitions between the symmetric spin eigenstates,  $\psi_1$ ,  $\psi_{0,S}$  and  $\psi_{-1}$ , and the antisymmetric state  $\psi_{0,A}$  (25). As a result, we can express a general two-spin wave function  $\Psi$  as a linear combination of energy eigenfunctions (similar to equation 1.13), as follows

$$(1.50) \quad \Psi = a_1(t)\psi_1 + a_0(t)\psi_{0,S} + a_{-1}(t)\psi_{-1}$$

$$(1.51) \quad \Psi = \sum_{n=-1}^1 a_n(t)\psi_n$$

where the coefficients,  $a_n(t)$ , are given by

$$(1.52) \quad a_n(t) = C_n \exp(-i E_n t / \hbar)$$

In this expression, the energy eigenvalue,  $E_n$ , corresponds to the eigenstate  $\psi_n$ , and the coefficient  $C_n$  is time dependent, as will be demonstrated below. In the special case in which the two-spin system is in thermal equilibrium with the lattice, it is most probable that the system will be in the lowest energy spin eigenstate,  $\psi_1$ . Thus, for the purposes of describing nuclear relaxation, we are interested in the rate at which a spin system undergoes transitions from the states  $\psi_{0,S}$  and  $\psi_{-1}$  to the state  $\psi_1$ .

The Hamiltonian of the dipole-dipole interaction,  $\mathcal{H}_{d-d}$ , similar to that of the Zeeman interaction, depends on the nuclear magnetic moment,  $\mu$ , and the magnetic field,  $\mathbf{b}$ , experienced by the spin as a result of an adjacent magnetic dipole. Therefore, to derive the dipole-dipole Hamiltonian we proceed as follows.

The magnetic field,  $\mathbf{b}$ , due to a magnetic dipole,  $\mu$ , is described in spherical-polar coordinates in equations 1.53 to 1.56, and the coordinate system used is illustrated in figure 1.4 (45).

$$(1.53) \quad \mathbf{b} = b_r \hat{\mathbf{r}} + b_\theta \hat{\boldsymbol{\theta}} + b_\phi \hat{\boldsymbol{\phi}}$$

$$(1.54) \quad b_r = \left( \frac{\mu_0}{4\pi} \right) \left( \frac{2\mu}{r^3} \right) \cos\theta$$

$$(1.55) \quad b_\theta = \left( \frac{\mu_0}{4\pi} \right) \left( \frac{\mu}{r^3} \right) \sin\theta$$

$$(1.56) \quad b_\phi = 0$$

where  $\mu_0$  is the permeability of free space, and  $\hat{\mathbf{r}}$ ,  $\hat{\boldsymbol{\theta}}$  and  $\hat{\boldsymbol{\phi}}$  are axial unit vectors in the spherical-polar coordinate system. Alternatively, this magnetic field can be expressed as (45)

$$(1.57) \quad \mathbf{b} = \left( \frac{\mu_0}{4\pi} \right) \left( \frac{1}{r^3} \right) [3(\mu \cdot \hat{\mathbf{r}})\hat{\mathbf{r}} - \mu]$$

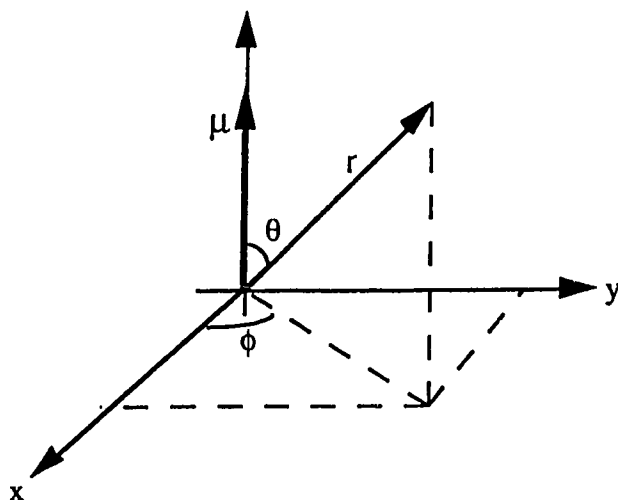


**Figure 1.4** Spherical-polar coordinate system used to describe the magnetic field due to a magnetic dipole moment,  $\mu$ .

Similar to the energy of the Zeeman interaction, given by equation 1.2, the energy of the interaction between a magnetic moment  $\mu_2$  and the field  $\mathbf{b}$  due to the magnetic moment  $\mu_1$  is given by:

$$(1.58) \quad E_{d-d} = \left( \frac{\mu_0}{4\pi} \right) \left( \frac{1}{r^3} \right) [\mu_1 \cdot \mu_2 - 3(\mu_1 \cdot \mathbf{r})(\mu_2 \cdot \mathbf{r})]$$

where  $r$  is now the distance between the two nuclei and  $\mathbf{r}$  is a unit vector pointing from one nucleus to the other. Because of the relationship between the nuclear spin of a nucleus and its magnetic moment, this energy can be expressed in terms of the nuclear spins as:

$$(1.59) \quad E_{d-d} = \left( \frac{\mu_0}{4\pi} \right) \left( \frac{\gamma^2 \hbar^2}{r^3} \right) [\mathbf{I}_1 \cdot \mathbf{I}_2 - 3(\mathbf{I}_1 \cdot \mathbf{r})(\mathbf{I}_2 \cdot \mathbf{r})]$$

Expanding this equation further in terms of spin operators yields the Hamiltonian for the dipole-dipole interaction,  $\mathcal{H}_{d-d}$ , as shown in equation 1.60 (13)

$$(1.60) \quad \mathcal{H}_{d-d} = \left( \frac{\mu_0}{4\pi} \right) \left( \frac{\gamma^2 \hbar^2}{r^3} \right) (A + B + C + D + E + F)$$

where:

$$A = I_{z1} I_{z2} (1-3\cos^2\theta_{12})$$

$$B = (-1/4)[I_{-1} I_{+2} + I_{+1} I_{-2}] \cdot (1-3\cos^2\theta_{12})$$

$$C = (-3/2)[I_{+1} I_{z2} + I_{+2} I_{z1}] \cdot \sin\theta_{12} \cos\theta_{12} \exp(-i \phi_{12})$$

$$D = (-3/2)[I_{-1} I_{z2} + I_{-2} I_{z1}] \cdot \sin\theta_{12} \cos\theta_{12} \exp(i \phi_{12})$$

$$E = (-3/4)(I_{+1} I_{+2}) \sin^2\theta_{12} \exp(-i 2\phi_{12})$$

$$F = (-3/4)(I_{-1} I_{-2}) \sin^2\theta_{12} \exp(i 2\phi_{12})$$

Expanding the dipole-dipole Hamiltonian into this form helps to illustrate several important points about it. Firstly, the A and B terms, called the secular terms of the Hamiltonian, do not involve net upward or downward energy transitions and so do not represent longitudinal relaxation effects. All of the terms, however, demonstrate a spatial dependence of the interaction strength. Term B represents an exchange of energy between two spins, and thus together they contribute to transverse relaxation effects. The C and D terms, on the other hand, involve energy state transitions of one spin, with the spins exchanging energy at the frequency  $\omega_0$  with the thermal lattice. Similarly, the E and F terms involve energy state transitions of both spins in the same direction and energy at the frequency  $2\omega_0$  is either gained or lost to the thermal lattice by the coupled-spin pair. As a result, spin state transitions, and therefore longitudinal relaxation, occurs only as a result of spins absorbing or emitting energy at specific frequencies,  $\omega_0$  and  $2\omega_0$ . It is

important to note, however, that because the heat capacity of the thermal lattice is very large relative to that of the spin system, the lattice is essentially always at thermal equilibrium with it. Lower Boltzmann energy states more populated than the higher energy states. A spin system is more likely to donate energy to the lattice, than it is to absorb energy from the lattice.

Now that the form of the spin wave function and of the dipole-dipole Hamiltonian have been established, we can investigate the probability that a transition between spin states and a change in the energy of the spin system will occur. Initially, we can assume that a given spin is in a state,  $j$ . The probability that this spin can be found in a different state,  $k$ , at a time  $t$  later, is given by  $P_{jk}$  (25)

$$(1.61) \quad P_{jk} = C_k^*(t) C_k(t)$$

where the functions,  $C_k(t)$ , are as described by equation 1.52. Thus, to describe the spin system relaxation toward thermal equilibrium we must determine the functional form of the coefficients,  $C_k$ , which were used to describe the spin wave function  $\Psi$ .

To obtain information about the coefficients of the spin wave function, we can make use of the time dependent Schroedinger equation

$$(1.62) \quad \mathcal{H}_{\text{tot}} \Psi = i \hbar \frac{\delta \Psi}{\delta t}$$

where  $\mathcal{H}_{\text{tot}}$  is the total Hamiltonian given by

$$(1.63) \quad \mathcal{H}_{\text{tot}} = \mathcal{H}_z + \mathcal{H}_{\text{d-sec}} + \mathcal{H}_{\text{d-ns}}$$

and where  $\mathcal{H}_{\text{d-sec}}$  is the secular part of the dipole-dipole Hamiltonian which contains only the A and B terms, and  $\mathcal{H}_{\text{d-ns}}$  is the remaining portion of the dipole-dipole Hamiltonian containing the C to F terms. It is important to note that the spin eigenstates described by equations 1.46 to 1.49 are also stationary eigenstates of the truncated Hamiltonian,  $\mathcal{H}_{\text{Trunc}}$ , which is defined by

$$(1.64) \quad \mathcal{H}_{\text{Trunc}} = \mathcal{H}_z + \mathcal{H}_{\text{d-sec}}$$

Because the magnetic field experienced by a spin due to a nearby spin magnetic moment is much smaller than the static  $B_0$  field provided by the NMR hardware, we can make the assumption that

$$(1.65) \quad \mathcal{H}_z + \mathcal{H}_{\text{d-sec}} \gg \mathcal{H}_{\text{d-ns}}$$

and make use of time-dependent perturbation theory to investigate the effects of the dipole-dipole interaction on the spin wave function (25).

Time-dependent perturbation theory requires the basic assumption that the perturbation Hamiltonian,  $\mathcal{H}_{\text{d-ns}}$ , is much smaller than the non-perturbed Hamiltonian,  $\mathcal{H}_{\text{Trunc}}$ , as we have already described, so that the spin eigenstates of  $\mathcal{H}_{\text{Trunc}}$  can be assumed to be reasonable approximations for the spin eigenstates of  $\mathcal{H}_{\text{tot}}$  as well. Making this assumption, and expanding  $\mathcal{H}_{\text{tot}}$  as described in equation 1.63, the time dependent Schroedinger equation (equation 1.62) becomes

$$(1.66) \quad (\mathcal{H}_z + \mathcal{H}_{\text{d-sec}}) \Psi + \mathcal{H}_{\text{d-ns}} \Psi = i \hbar \frac{\delta \Psi}{\delta t}$$

The time derivative of  $\Psi$  can also be expanded by substituting from equation 1.51 as follows.

$$(1.67) \quad \frac{\delta \Psi}{\delta t} = \sum_{n=-1}^1 \frac{\delta a_n(t)}{\delta t} \psi_n + \sum_{n=-1}^1 a_n(t) \frac{\delta \psi_n}{\delta t}$$

Because  $\psi_n$  represents the stationary eigenstates of  $\mathcal{H}_z + \mathcal{H}_{d\text{-sec}}$ , the time dependent Schroedinger equation gives the result

$$(1.68) \quad (\mathcal{H}_z + \mathcal{H}_{d\text{-sec}}) \sum_{n=-1}^1 a_n(t) \psi_n = i \hbar \sum_{n=-1}^1 a_n(t) \frac{\delta \psi_n}{\delta t}$$

This equality allows these terms to be subtracted from both sides of equation 1.66 to give

$$(1.69) \quad \mathcal{H}_{d\text{-ns}} \sum_{n=-1}^1 a_n(t) \psi_n = i \hbar \sum_{n=-1}^1 \frac{\delta a_n(t)}{\delta t} \psi_n$$

Now, to investigate a single  $C_n$ , say  $C_k$ , we can multiply the left side of all terms in equation 1.69 by  $a_k^*(t)\psi_k^*$  and integrate over all space to make use of the orthonormal properties of  $\psi_k$ . Secondly, we can make a simplifying assumption about the starting conditions by supposing that at  $t = 0$ , the system is definitely in state  $j$ , so that  $C_j(0) = 1$ , and all other  $C_n(0) = 0$ . The result of these manipulations is that equation 1.69 becomes

$$(1.70) \quad \langle \psi_k | \mathcal{H}_{d\text{-ns}} | \psi_j \rangle \exp\left[\frac{-i E_j t}{\hbar}\right] = i \hbar \frac{\delta C_k}{\delta t} \exp\left[\frac{-i E_k t}{\hbar}\right]$$

which, when rearranged, gives an expression for  $\frac{\delta C_k}{\delta t}$

$$(1.71) \quad \frac{\delta C_k}{\delta t} = \frac{-i}{\hbar} \exp\left[\frac{-i(E_j - E_k)t}{\hbar}\right] \langle \psi_k | \mathcal{H}_{d-ns} | \psi_j \rangle$$

Integrating this expression over time yields an expression for  $C_k(t)$  as well.

$$(1.72) \quad C_k(t) = \frac{-i}{\hbar} \int_0^t \exp\left[\frac{-i(E_j - E_k)t'}{\hbar}\right] \langle \psi_k | \mathcal{H}_{d-ns} | \psi_j \rangle dt'$$

Equations 1.71 and 1.72 demonstrate that as a result of the non-secular terms of the dipole-dipole Hamiltonian, the coefficients used to describe the two-spin wave function, are functions of time. Furthermore, the important energy difference in the time dependence of  $C_k$  is  $E_j - E_k$ , the energy of the spin state transition.

Returning to the problem of computing the probability of a spin state transition taking place, we can now compute the transition probability per unit time,  $W_{jk}$ , given by

$$(1.73) \quad W_{jk} = \frac{dP_{jk}}{dt} = \frac{dC_k^*(t)}{dt} C_k(t) + C_k^*(t) \frac{dC_k(t)}{dt}$$

where  $P_{jk}$  is defined in equation 1.61. Because  $C_k(t)$  is a function of time only, we can substitute the partial derivative of  $C_k(t)$  (equation 1.71) for  $dC_k(t)/dt$ . Substituting the expression given in equation 1.72 for  $C_k(t)$  then yields the expression

$$\begin{aligned}
 (1.74) \quad W_{jk} = & \frac{1}{\hbar^2} \int_{-t}^0 \langle \psi_k | \mathcal{H}_{d\text{-}ns} | \psi_j \rangle \langle \psi_j | \mathcal{H}_{d\text{-}ns} | \psi_k \rangle \exp[-i\omega_{jk}\tau] d\tau \\
 & + \frac{1}{\hbar^2} \int_{-t}^0 \langle \psi_j | \mathcal{H}_{d\text{-}ns} | \psi_k \rangle \langle \psi_k | \mathcal{H}_{d\text{-}ns} | \psi_j \rangle \exp[i\omega_{jk}\tau] d\tau
 \end{aligned}$$

where  $\omega_{jk}$  has been used to express  $(E_j - E_k)/\hbar$  and  $\tau = (t' - t)$ . Equation 1.74 can be simplified somewhat by recognizing that the second integral is the complex conjugate of the first, and that the complex conjugate in this expression amounts to a change in the sign of  $\tau$ . Therefore, we can integrate over the range of  $-t$  to  $t$  and combine the two integrals as follows

$$(1.75) \quad W_{jk} = \frac{1}{\hbar^2} \int_{-t}^t \langle \psi_k | \mathcal{H}_{d\text{-}ns} | \psi_j \rangle \langle \psi_j | \mathcal{H}_{d\text{-}ns} | \psi_k \rangle \exp[-i\omega_{jk}\tau] d\tau$$

Furthermore, if the integration interval,  $2t$ , is much larger than the period  $2\pi/\omega_{jk}$  we can change the integral limits to be  $-\infty$  to  $\infty$  to yield equation 1.76. The usefulness of such a change will become apparent in the following discussion.

$$(1.76) \quad W_{jk} = \frac{1}{\hbar^2} \int_{-\infty}^{\infty} \langle \psi_k | \mathcal{H}_{d\text{-}ns} | \psi_j \rangle \langle \psi_j | \mathcal{H}_{d\text{-}ns} | \psi_k \rangle \exp[-i\omega_{jk}\tau] d\tau$$

The non-secular part of the dipole-dipole Hamiltonian,  $\mathcal{H}_{d\text{-}ns}$ , can be expanded into its terms, C to F, and each of these can be expressed as a product of a space term,  $Z$ , and a spin term,  $\Phi$ .

$$(1.77) \quad \mathcal{H}_{d\text{-}ns} = \sum_{n=C \text{ to } F} Z_n \Phi_n$$

With  $\mathcal{H}_{d-ns}$  expanded into this form, the terms within the integral in equation 1.76 become

$$(1.78) \quad \langle \psi_k | \mathcal{H}_{d-ns} | \psi_j \rangle = \sum_{n=C \text{ to } F} Z_n \langle \psi_k | \Phi_n | \psi_j \rangle$$

$$(1.79) \quad \langle \psi_j | \mathcal{H}_{d-ns} | \psi_k \rangle = \sum_{n=C \text{ to } F} Z_n \langle \psi_j | \Phi_n | \psi_k \rangle$$

and equation 1.74 becomes

$$(1.80) \quad W_{jk} = \frac{1}{\hbar^2} \sum_{n=C \text{ to } F} |\langle \psi_k | \Phi_n | \psi_j \rangle|^2 \int_{-\infty}^{\infty} Z(t) Z(t') \exp[-i\omega_{jk}\tau] d\tau$$

Because the relative positions and orientations of the two spins vary randomly in time, the space parts of the Hamiltonian,  $Z(t)$ , vary randomly in time. As a result,  $Z(t)$  is not an analytical function so we cannot exactly predict its value at every point in time.

In order to deal with the random function,  $Z(t)$ , we can compute an autocorrelation function,  $G(\tau)$  which describes how well  $Z(t)$  correlates with itself over a time interval of duration  $\tau$ . This autocorrelation function is defined by

$$(1.81) \quad G(\tau) = \overline{Z(t)Z(t')}$$

where  $\overline{\quad}$  denotes the ensemble average, and again  $\tau = (t' - t)$ . To describe the distribution of the random motions of the interacting spins it is assumed that the auto-correlation function decays exponentially with the characteristic time,  $\tau_c$ , known as the correlation time, so that  $G(\tau)$  has the form

$$(1.82) \quad G(\tau) = G(0) \exp(-\tau/\tau_c)$$

To determine the frequency distribution of the random spin motions, and therefore to determine at which motional frequencies the thermal energy of the spins is stored, we compute the Fourier transform of the autocorrelation function

$$(1.83) \quad J(\omega) = \int_{-\infty}^{+\infty} G(\tau) \exp(-i \omega \tau) d\tau$$

The function  $J(\omega)$  is known as the spectral density. Substituting the exponential form of  $G(\tau)$  given in equation 1.82 yields the Debye spectral density, where

$$(1.84) \quad J(\omega) = \int_{-\infty}^{+\infty} G(0) \exp(-\tau/\tau_c) \exp(-i \omega \tau) d\tau$$

$$(1.85) \quad J(\omega) = G(0) \frac{\tau_c}{[1 + (\omega\tau_c)^2]}$$

The Debye spectral density describes the magnitudes of the frequency components of the random thermal motions of nuclei in a liquid-like spin system, as shown in figure 1.5.

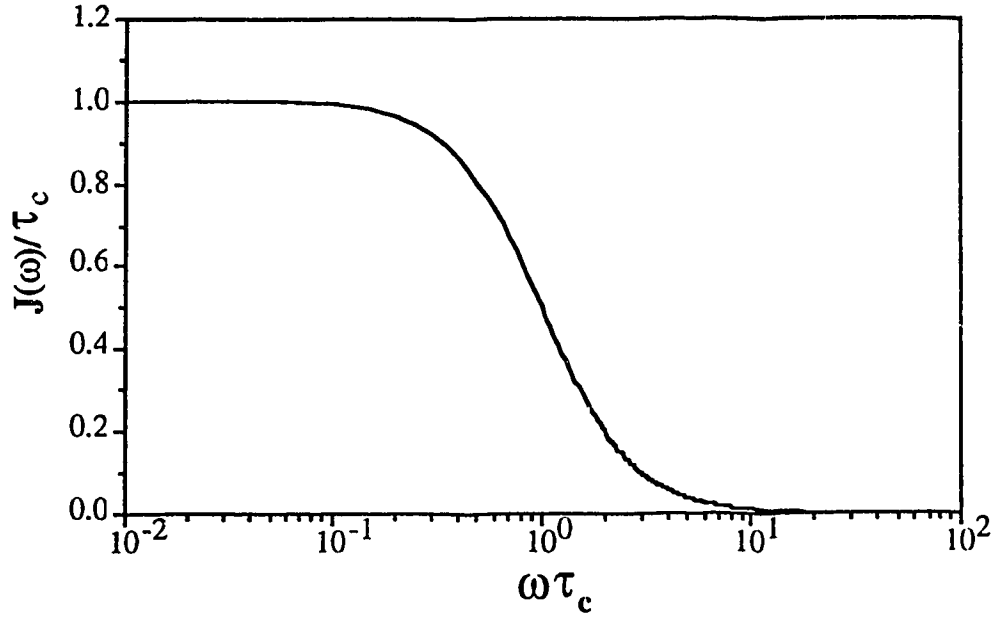


**Figure 1.5** The dependence of the normalized Debye spectral density on frequency, expressed relative to the correlation time,  $\tau_c$ .

This figure demonstrates that the random motions of the spins may have many frequency components, two of which correspond to the frequencies  $\omega_0$  and  $2\omega_0$ . Furthermore, it can be seen that by computing the ensemble average of  $W_{jk}$  in equation 1.80, the integral term in this equation can be substituted by the Debye spectral density described in equation 1.83. As a result

$$(1.86) \quad W_{jk} = \frac{1}{\hbar^2} \sum_{n=C \text{ to } F} |\langle \psi_k | \Phi_n | \psi_j \rangle|^2 J(\omega_{jk})$$

Since we are interested in relaxation of the spin system toward thermal equilibrium, and the thermal lattice is more likely to receive energy from the spin system than it is to give up energy to the spin system, we are concerned only with those terms of

$\mathcal{H}_{d-ns}$  resulting in transitions to lower energy states, i.e. the C and E terms. The longitudinal relaxation rate,  $R_1$ , is therefore given by

$$(1.87) \quad R_1 \propto \sum_{C \text{ and } E} W_{jk}$$

Substituting for the form of  $W_{jk}$  from equation 1.86 we obtain the expression

$$(1.88) \quad R_1 \propto k_1 J(\omega_o) + k_1' J(2\omega_o)$$

where  $k_1$  and  $k_1'$  are constants which allow for the different magnitudes of the space parts of the C and E terms of  $\mathcal{H}_{d-ns}$ . For the more specific case of a system of weakly interacting protons, this expression is (74)

$$(1.89) \quad R_1 = k_1'' \left\{ J(\omega_o) + 4 J(2\omega_o) \right\}$$

where  $k_1''$  is a constant which depends on the dipole-dipole interaction strength, the nature of the motion, and nuclear constants such that

$$(1.90) \quad R_1 = \left( \frac{6}{20} \right) \left[ \frac{\gamma^4 \hbar^2}{r^6} \right] \left\{ \frac{\tau_c}{[1 + (\omega_o \tau_c)^2]} + \frac{4\tau_c}{[1 + 4(\omega_o \tau_c)^2]} \right\}$$

This equation describes the spin-lattice relaxation rate dependencies on both the resonant frequency of the system as well as the correlation times of the motions of the interacting spins. The relaxation mechanisms are most efficient, and  $R_1$  is at a maximum, when  $\omega_o \tau_c = 0.64$  (i.e. approximately unity) as demonstrated in figure 1.6. The NMR hardware employed for the studies discussed in Chapters 2 and 3 resulted in a proton resonant frequency,  $\omega_o$ , of 100 MHz ( $10^8$  Hz) and for water

molecules in solution at room temperature the value of  $\tau_c$  is roughly  $3 \times 10^{-12}$  seconds (30). The product of these two constants,  $\omega_0 \tau_c$ , has a value of  $10^{-4}$  and figure 1.6 therefore demonstrates that the relaxation of pure water protons is not very efficient at a proton resonant frequency of 100 MHz. A macromolecule of molecular weight 20 000, however, may have a rotational correlation time of  $10^{-8}$  seconds and relaxation rates may be nearly maximal for protons in such molecules at a resonant frequency of 100 MHz (30).

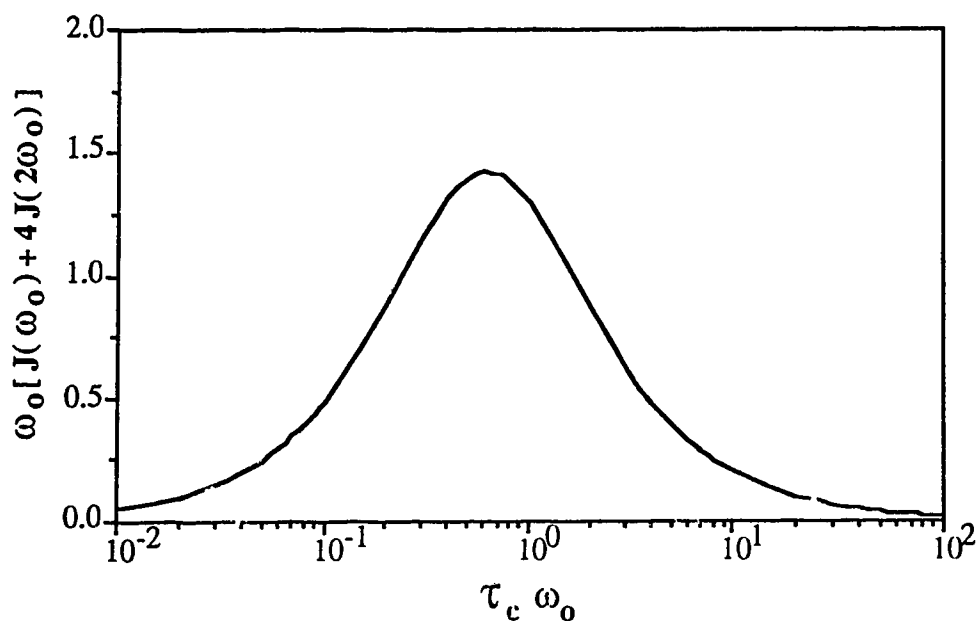


**Figure 1.6** The dependence of the quantity,  $\omega_0[J(\omega_0) + 4 J(2\omega_0)]$ , and therefore the dependence of  $R_1$ , on the value of  $\tau_c$ , for a fixed frequency,  $\omega_0$ .

The time dependent nature of the coefficients,  $C_k$ , arising from the non-secular terms of the dipole-dipole Hamiltonian, results in a time dependent expectation value for the individual transverse spin components (equation 1.19). In a description of the relaxation of the transverse component of the magnetization it is therefore necessary to include the non-secular terms of the dipole-dipole Hamiltonian as well as the secular (A and B) terms. As a result, the transverse

relaxation rate also depends on those terms used to describe the longitudinal relaxation rate, namely  $J(\omega_0)$  and  $J(2\omega_0)$ . In addition, the A and B terms of the dipole-dipole Hamiltonian involve near-zero frequency components of the spin motions so that the transverse relaxation rate,  $R_2$ , is given by (1)

$$(1.91) \quad R_2 \propto k_2 J(0) + k_2' J(\omega_0) + k_2'' J(2\omega_0)$$

where  $k_2$ ,  $k_2'$  and  $k_2''$  are constants, similar to those employed in equation 1.88. The transverse relaxation rate of a system of weakly interacting protons is given by

$$(1.92) \quad R_2 = k_2'' \{ 3 J(0) + 5 J(\omega_0) + 2 J(2\omega_0) \}$$

where  $k_2''$  is a constant which depends on the dipole-dipole interaction strength and nuclear constants (1) such that

$$(1.93) \quad R_2 = \left( \frac{3}{20} \right) \left[ \frac{\gamma^4 \hbar^2}{r^6} \right] \left\{ 3\tau_c + \frac{5\tau_c}{[1 + (\omega_0\tau_c)^2]} + \frac{2\tau_c}{[1 + 4(\omega_0\tau_c)^2]} \right\}$$

This expression for the transverse relaxation rate, in conjunction with figure 1.6 and equation 1.90, demonstrates that for a system of protons having a resonant frequency of 100 MHz and a correlation time of  $10^{-12}$  seconds,  $R_1$  and  $R_2$  are approximately equal. However, at the same proton resonant frequency, for a spin system having a correlation time of  $10^{-8}$  seconds the value of  $R_2$  is approximately twice that of  $R_1$ . Furthermore, because the transverse relaxation rate depends on  $J(0)$  it does not reach an upper limit at a  $\tau_c$  value near  $1/\omega_0$  as does  $R_1$ , but rather continues to increase with increasing  $\tau_c$ . As a result, it is possible for  $R_2$  to be orders of magnitude greater than  $R_1$ .

## Quadrupolar Relaxation

Quadrupolar relaxation occurs only when a nucleus with a spin  $I > 1/2$ , and therefore possessing an electric quadrupole moment, interacts with a time dependent local electric field gradient. The source of this electric field gradient is usually the electronic structure of the molecule which contains the nucleus of interest, but nearby ions or molecules can also contribute. For the case in which a nucleus with spin,  $I$ , and electric quadrupole moment,  $Q$ , interacts with a field described by an electric potential,  $V(x,y,z)$ , the Hamiltonian of the interaction,  $\mathcal{H}_q$ , is given by (72)

$$(1.94) \quad \mathcal{H}_q = \frac{eQ}{4I(2I-1)} [A' + B' + C' + D' + E']$$

where:

$$A' = V_{zz} (3I_z^2 - I^2)$$

$$B' = (V_{zx} + i V_{zy}) (I_+ I_z + I_z I_-)$$

$$C' = (V_{zx} - i V_{zy}) (I_+ I_z + I_z I_+)$$

$$D' = \left[ \frac{1}{2}(V_{xx} - V_{yy}) + i V_{xy} \right] (I_-)^2$$

$$E' = \left[ \frac{1}{2}(V_{xx} - V_{yy}) - i V_{xy} \right] (I_+)^2$$

The quantity  $e$  is the electronic charge, and  $V_{xx}$ ,  $V_{xy}$ ,  $V_{yz}$ , ... etc., represent the second partial derivatives of  $V$  with respect to  $x$ ,  $y$ , and  $z$ . It is important to keep in mind that the electric potential,  $V$ , is determined by the electronic structure of the molecule and that the derivatives of this potential can vary randomly at the location of the nucleus of interest. Thus, with  $\mathcal{H}_q$  expressed in this form, and recognizing the fact that each of the terms  $A'$  to  $E'$  contain both a space term and a spin term, the similarities between  $\mathcal{H}_q$  and  $\mathcal{H}_{d-d}$  in equation 1.60 are apparent. As a result, the method that was used to describe dipole-dipole relaxation from the starting point of the dipole-dipole Hamiltonian, can also be applied to the quadrupolar Hamiltonian

to describe quadrupolar relaxation. Expressions for the transverse and longitudinal quadrupolar relaxation rates, of an ensemble of spin  $I = 1$  nuclei in a liquid like system, are given in equations 1.95 and 1.96, respectively (1).

$$(1.95) \quad R_1 = \left(\frac{3}{80}\right) \xi \left\{ \frac{\tau_c}{[1 + (\omega_o \tau_c)^2]} + \frac{4\tau_c}{[1 + 4(\omega_o \tau_c)^2]} \right\}$$

$$(1.96) \quad R_2 = \left(\frac{1}{100}\right) \xi \left\{ 9\tau_c + \frac{15\tau_c}{[1 + (\omega_o \tau_c)^2]} + \frac{6\tau_c}{[1 + 4(\omega_o \tau_c)^2]} \right\}$$

where the correlation time,  $\tau_c$ , characterizes the time dependence of the spatial derivatives of  $V$  at the location of the nucleus of interest. The coefficient,  $\xi$ , expressed in a principal axis coordinate system ( $x', y', z'$ , such that  $V_{ij} = 0$  for  $i \neq j$ ) is given by

$$(1.97) \quad \xi = \left(1 + \frac{\eta^2}{3}\right) \left(\frac{eQ}{h} V_{z'z'}\right)^2$$

In this expression,  $\eta$ , known as the asymmetry parameter, is a measure of the electric field gradient deviation from axial symmetry, and is given by

$$(1.98) \quad \eta = \frac{V_{x'x'} - V_{y'y'}}{V_{z'z'}}$$

The rates of nuclear relaxation resulting from the dipole-dipole and quadrupolar interactions have similar dependencies on  $\omega_o$  and  $\tau_c$  because we have assumed the same form of the autocorrelation function to characterize the random motions which mediate each of these interactions. However, the strengths of these two interactions can be considerably different. This is demonstrated by the fact that the  $T_1$  of water

protons in a cat brain is dominated by the dipole-dipole interaction and has a value of 1.5 seconds. In a hypothetical situation in which we exchanged these water protons for deuterons, and in which the dipole-dipole interaction was still dominant, the  $T_1$  value resulting from equation 1.90 would be approximately 2700 seconds because of the lower deuteron gyromagnetic ratio ( $\gamma_{\text{proton}}/\gamma_{\text{deuteron}} = 6.5$ ). The  $T_1$  of deuterons in  $D_2O$  in a cat brain, however, is dominated by quadrupolar relaxation and has a value of roughly 250 msec (26). The ratio of the interaction strengths, i.e.  $\xi/(\gamma^4 \hbar^2/r^6)$ , in this hypothetical situation, is  $8.6 \times 10^4$ . Thus, in comparing these two specific examples it can be seen that the strength of the quadrupolar interaction can be several orders of magnitude greater than that of the dipole-dipole interaction.

### **The Two-Site Rapid Exchange Model of Relaxation**

In biological systems, such as the lung, the environment affecting magnetization relaxation is often spatially heterogeneous. In cases in which there are two relaxation environments, the relaxation rates observed depend strongly on the rate at which mobile nuclei can exchange between the two environments (29). The description of the relaxation in a system with two relaxation environments is generally tractable if it can be expressed in either the "fast-exchange" case, in which the mean exchange time between the two environments is much shorter than the relaxation time in either environment, or the "slow-exchange" case, in which the relaxation times are much shorter than the exchange time between the environments

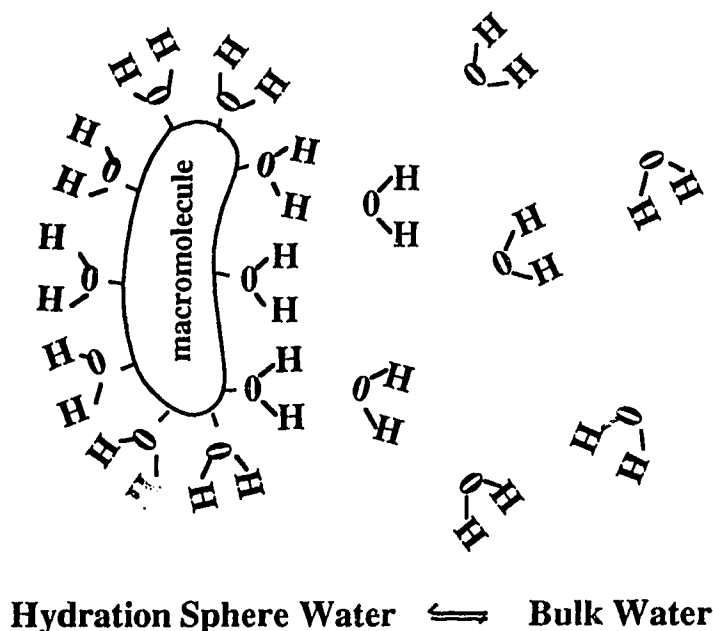


**Figure 1.7** Schematic representation of water protons in two rapidly exchanging relaxation environments; bulk water and water in a hydration sphere around a macromolecule.

The "fast-exchange" case generally occurs when two distinct relaxation environments are either in contact, or are separated by a physical boundary which only marginally impedes the diffusion of the water molecules from one environment to the other. An example of this case is illustrated in figure 1.7 in which protons in bulk water can diffuse rapidly from the slowly relaxing bulk water environment to the hydration sphere where they can exchange spin energy with the much faster relaxing protons in the macromolecule in solution (29). Similarly, this situation may arise for fluid in the airspaces of the lung, which is also in contact with epithelial cell membranes. Macromolecules which are incorporated into a cell membrane also contain relatively fast relaxing protons which can exchange spin energy with water protons in the hydration sphere. Because a given water proton

can spend time in the bulk water and in a hydration sphere while relaxing to thermal equilibrium with the lattice, we can observe only an average relaxation rate,  $R_{\text{obs}}$ , for the spin system. The relaxation rate observed is a weighted average of the relaxation rates in each of these two environments, as shown in equation 1.99.

$$(1.99) \quad R_{\text{obs}} = \rho_{\text{free}} R_{\text{free}} + \rho_{\text{bound}} R_{\text{bound}}$$

The relaxation rates  $R_{\text{free}}$  and  $R_{\text{bound}}$  are those of water protons in the bulk water and in the hydration sphere water, respectively. The quantities  $\rho_{\text{free}}$  and  $\rho_{\text{bound}}$  are the relative fractions of water protons, contributing to the water signal, in the bulk water and in the hydration sphere, respectively.

The "slow-exchange" case, on the other hand, gives rise to two or more relaxation components, and generally occurs when two different relaxation environments are separated by a physical boundary which impedes the diffusion of water molecules between the two environments. An example of this case is lung alveolar fluid with a water proton relaxation time of  $T_{\text{alv}}$ , which is separated from interstitial fluid with a water proton relaxation time of  $T_{\text{int}}$ , by the highly impermeable alveolar epithelium. Because the epithelium prevents the rapid diffusion of water between alveolar and interstitial fluid, a given water proton will relax under the influence of only one of the two environments. The NMR signal from such a spin system is thus a sum of the signals arising from water protons in each of the two relaxation environments, and demonstrates a bi-exponential decay as indicated by equation 1.100.

$$(1.100) \quad S(t) = S_0 [\rho_{\text{alv}} \exp(-t/T_{\text{alv}}) + \rho_{\text{int}} \exp(-t/T_{\text{int}})]$$

In this equation, the quantities  $\rho_{\text{alv}}$  and  $\rho_{\text{int}}$  are the relative fractions of water protons, contributing to the water signal, in the alveolar fluid and in the interstitial fluid, respectively.

The studies discussed in the following chapters include relaxation time measurements for lung water protons. Because of the heterogeneous nature of the lung, the measured lung water proton relaxation times are highly dependent on the two-site rapid exchange model of relaxation. Moreover, it is a consequence of the bi-exponential signal decay detected in the "slow-exchange" case that we believe we are able to measure relaxation times of two distinct fluid compartments in the lung.

### 1.3.3 NMR Imaging Theory

In order to obtain a two dimensional (2D) NMR image of a given plane in space (that presumably transects an object of interest), a nuclear excitation pulse sequence must satisfy three fundamental requirements which are;

- 1) to generate a detectable NMR signal,
- 2) to provide a means of defining the desired plane with spatially selective pulses, and
- 3) to provide a means of spatially encoding the signal in two dimensions in that plane.

The following sections detail the production of spin-echoes and gradient-recalled echoes, spatially selective pulses, the spatial encoding of magnetization represented in k-space, and some common image reconstruction techniques.

## Theory of Spin Echoes and Gradient-Recalled Echoes

The presence of local inhomogeneities in a static  $B_0$  field, whether caused by variations in magnetic susceptibility at regional boundaries in a heterogeneous sample, or by the NMR hardware, causes difficulties in the observation of the natural transverse relaxation time of a spin system,  $T_2$ , by reducing the transverse relaxation time observed from the natural  $T_2$ , i.e.  $T_2^* < T_2$ . To overcome these difficulties we make use of the fact that dephasing of the transverse magnetization caused by static field inhomogeneities is, in many cases, reversible. Figure 1.8 illustrates a situation in which the net magnetization of a spin ensemble has been rotated onto the  $y_p$  axis by means of a  $90^\circ$  RF pulse. The ensemble magnetization is then left to evolve under the influence of  $B_0$  for a time period  $\tau$ , during which static field inhomogeneities cause the transverse magnetization components to lose phase coherence.

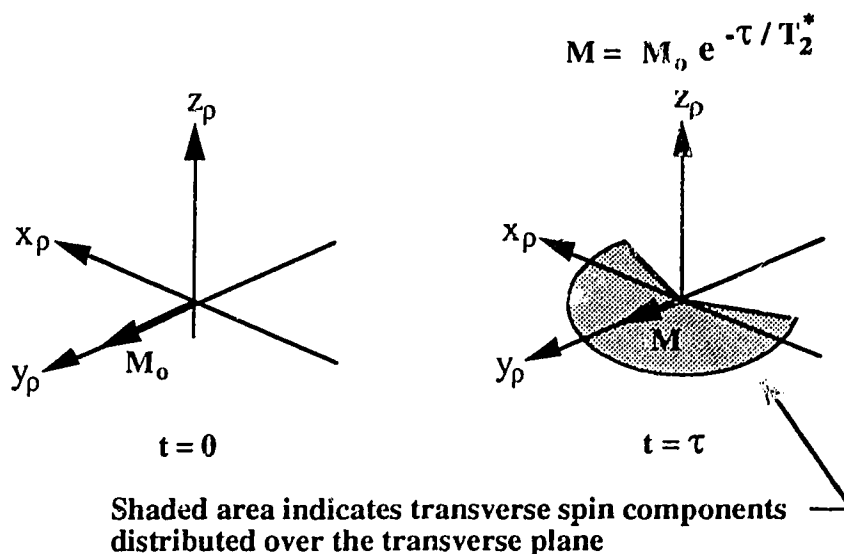


**Figure 1.8** Dephasing of transverse magnetization components due to static magnetic field inhomogeneities, depicted in the rotating frame of reference.

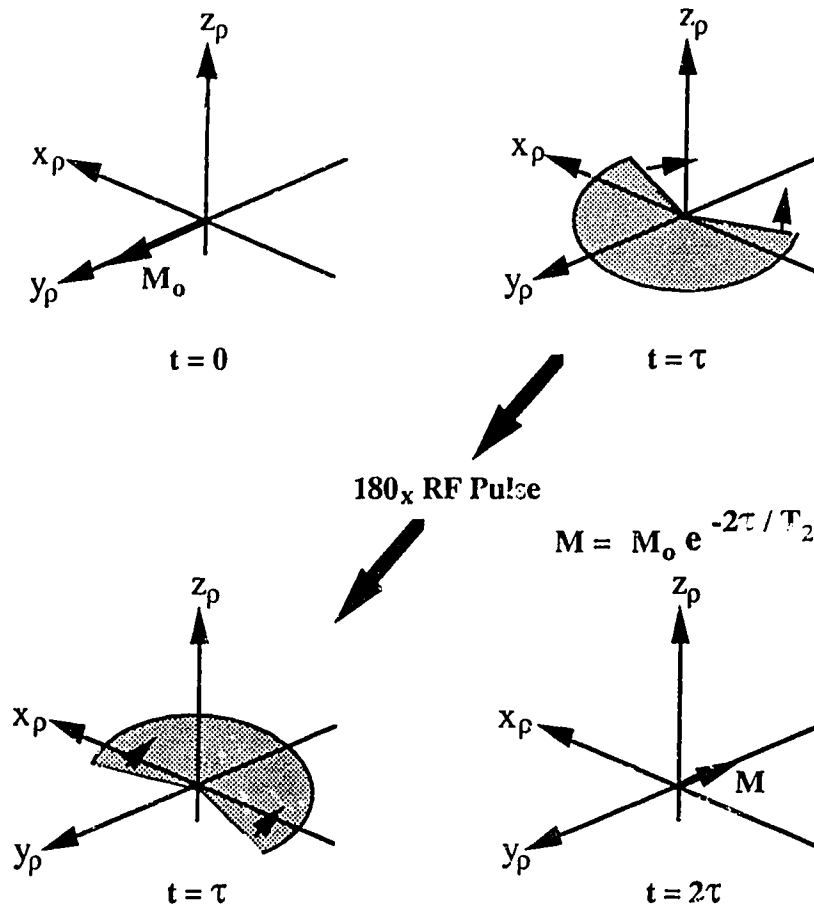


**Figure 1.9** The time course of changes in the transverse magnetization of an ensemble of spins due to the effects of static  $B_0$  inhomogeneities being refocussed at a time  $2\tau$  after the initial  $90_x$  RF pulse rotated the magnetization into the transverse plane.

If at the time  $t = \tau$ , as defined in figure 1.8, a  $180^\circ$  RF pulse is applied with  $B_1$  in the  $x_\rho$  direction (written  $180_x$ ), the spins are flipped about the  $x_\rho$  axis and the phase distribution about the  $-y_\rho$  axis becomes the opposite of that phase distribution about the  $+y_\rho$  axis immediately prior to the application of the RF pulse. In other words, a spin which precesses faster than the rotating reference frame, such that it is at an angle  $\phi_f$  from the  $y_\rho$  axis at the time  $t = \tau$ , is rotated by means of the  $180_x$  pulse to

be at an angle  $-\phi_f$  from the  $-y_p$  axis. Similarly, a spin which precesses slower than the reference frame will therefore lag the  $+y_p$  axis by an angle  $\phi_s$  at the time  $t = \tau$ , is rotated by means of the  $180_x$  pulse to lead the  $-y_p$  axis by the angle  $\phi_s$ . Thus, during a further time interval of duration  $\tau$ , all spin dephasing due to static  $B_0$  field inhomogeneities is reversed and the net magnetization in the transverse plane reaches a maximum after this second  $\tau$  and is then directed along the  $-y_p$  axis. The magnitude of the refocussed transverse magnetization is reduced from its initial value at  $t = 0$ , however, by the irreversible transverse relaxation as illustrated in figure 1.9. After the transverse magnetization has been refocussed, the evolution of the relative phases of the spins continues, and once again the spins fan-out in the transverse plane. This sequence of RF pulses is known as the Hahn spin-echo sequence (34) and is written symbolically as  $[90_x - \tau - 180_x - \tau]$ . The NMR signal that can be detected from an ensemble of spins undergoing this process is illustrated in figure 1.10.

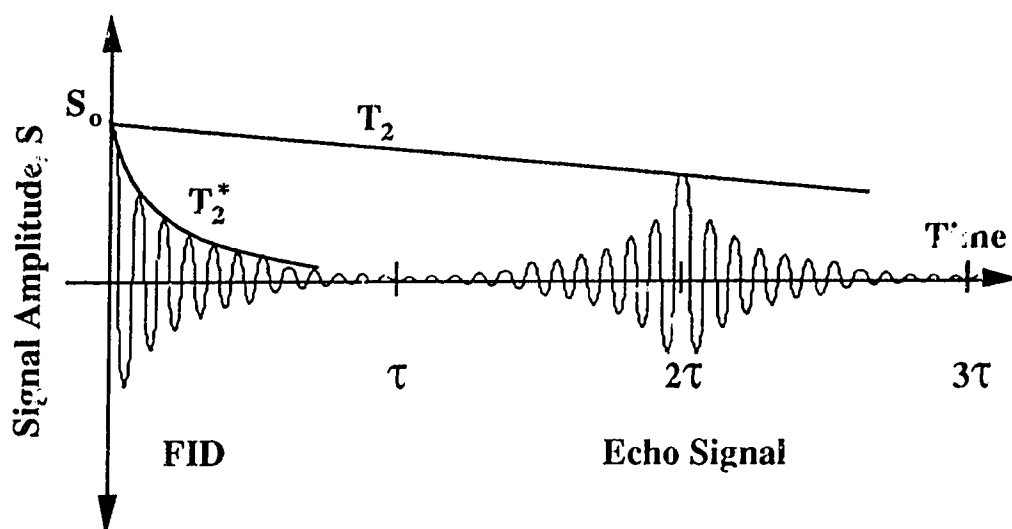


**Figure 1.10** NMR signal from an ensemble of spins with the effects of static  $B_0$  inhomogeneities being refocussed at a time  $2\tau$  after the initial  $90^\circ$  RF pulse rotated the magnetization into the transverse plane.

Note in figure 1.10 that the signal has been drawn as if the receiver phase was shifted  $180^\circ$  after detecting the free-induction decay signal (FID), in anticipation of the  $180^\circ$  change in phase of the echo signal, and the receiver reference frequency is slightly offset from the spin precessional frequency. Although the FID signal decays with the characteristic time  $T_2^*$ , the amplitude of the refocussed "echo" signal depends only on the natural transverse relaxation of the spin system and decays with the transverse relaxation time,  $T_2$ . Furthermore, with the application of a second  $180^\circ$  RF pulse at the time  $3\tau$ , a second echo can be formed at the time  $4\tau$  and so on, for as long as the echoes have non-zero amplitudes. Such an expansion of the Hahn sequence is known as the Carr-Purcell (CP) sequence (17) and is written  $[90_x - \tau - (180_x - \tau)^n]$ . By fitting an exponentially decaying curve to the echo amplitude maxima,  $S(2n\tau)$ , where  $n$  is an integer, the values of  $T_2$  and  $S_0$  can be determined as defined by equation 1.101.

$$(1.101) \quad S(2n\tau) = S_0 \exp(-2n\tau/T_2)$$

Because the Hahn and CP spin-echo amplitudes are highly sensitive to spatial variations or setting errors in the  $180^\circ$  refocussing pulses, the Carr-Purcell-Meiboom-Gill (CPMG) (55) spin-echo sequence  $[90_x - \tau - (180_y - \tau)^n]$ , was developed. Spin-echoes produced with the CPMG sequence are in phase because the magnetization is initially rotated onto the  $y_p$  axis and the  $180^\circ$  refocussing pulses rotate the magnetization about this same axis. Also, if the  $180^\circ$  pulses are imperfect and actually rotate the magnetization through slightly more, or less, than  $180^\circ$ , the error in the first pulse is negated by the error in the second pulse, and so on through the sequence. As a result, the even numbered echoes produced by the

CPMG sequence may provide more accurate data for measurements of  $T_2$  values, than those provided by either the Hahn or the CP spin-echo sequences.

An alternative to generating an echo signal by means of a  $180^\circ$  refocussing pulse is to reverse a gradient and produce what is called a gradient-recalled echo. Such an echo signal can be formed by first applying a magnetic field gradient to an ensemble of spins which are initially in phase, so that the spins are forced into a linear phase distribution along the gradient direction, and the net transverse magnetization reduces to zero. The phase distribution produced by this gradient can then be reversed by applying an equal and opposite gradient, the net transverse magnetization again approaches a maximum as an echo signal is formed which is similar to that produced by a spin-echo sequence. The use of a magnetic field gradient reversal to reverse the spin phase distribution has no effect on the dephasing caused by random inter-nuclear interactions or by static magnetic field inhomogeneities. The maximum amplitude of a gradient-recalled echo therefore decays exponentially with the characteristic time  $T_2^*$ , a salient difference from the Hahn spin-echo. Because the formation of a gradient-recalled echo does not require the transmission of tailored RF pulses, most NMR systems, particularly if they have actively shielded gradient coils, are able to produce gradient-recalled echoes with a shorter inter-echo interval than is possible for spin echoes. It is the ability to produce echo signals in rapid succession that makes the gradient-recalled echo sequence preferable to the spin-echo sequence for some imaging applications (57).

### **Spatially Selective RF Pulses**

The interaction between an ensemble of nuclear spins in a static  $B_0$  field with a rotating RF  $B_1$  field, as discussed in section 1.3.1, is highly dependent on the

frequency of the  $B_1$  field relative to the resonant frequency of the spins in the ensemble. It is the frequency dependence of this interaction that provides us with the means to excite spins selectively at a chosen location in space. This spatial selectivity requires the resonant frequency of the spins to be spatially dependent and so, for most NMR imaging applications, a linear magnetic field gradient is superimposed onto the homogeneous  $B_0$  field. The resultant static field is then as described by equation 1.102 for a gradient in the  $z$  direction.

$$(1.102) \quad \mathbf{B}(z) = B_0 \mathbf{k} + (G_z z) \mathbf{k}$$

In this expression the quantity  $G_z = \delta b / \delta z$  and  $\mathbf{b} = b \mathbf{k}$  is the gradient field. As a result of this magnetic field gradient, the resonant frequency varies along the  $z$  coordinate axis as depicted in equation 1.103

$$(1.103) \quad \omega(z) = \omega_0 + \gamma G_z z$$

If a  $\mathbf{B}_1$  field at the frequency  $\omega_0$  is now applied along the  $x_p$  axis in the rotating frame, the effective field in the rotating frame,  $\mathbf{B}_{\text{eff}}$  (defined by equation 1.34), is a function of position along the  $z$  axis, and is given by

$$(1.104) \quad \mathbf{B}_{\text{eff}}(z) = (B_0 + G_z z + \Omega/\gamma) \mathbf{k}_p + B_1 \mathbf{i}_p$$

and because  $\Omega = \omega_0 = -\gamma B_0$  (equation 1.32)

$$(1.105) \quad \mathbf{B}_{\text{eff}}(z) = G_z z \mathbf{k}_p + B_1 \mathbf{i}_p$$

If the  $B_1$  field is applied for the appropriate duration, spins at  $z = 0$  can be rotated through  $90^\circ$  into the  $y_p$  axis direction. However, the spins at  $z \neq 0$  will be rotated to lie at an angle of less than  $90^\circ$  from the  $z$  axis by such a  $B_1$  pulse, and their transverse components may not be aligned with the  $y_p$  axis, as illustrated in figure 1.2. For large  $z$ , such that  $z \gg B_1/G_z$ , the effective field in the rotating frame is essentially unaffected by the  $B_1$  pulse, and the spins remain aligned with  $B_0$  field. Figure 1.11 illustrates the transverse magnetization,  $M_{xy}$ , resulting from the application of a rectangular  $90^\circ$  RF pulse of duration  $2\tau$  and frequency  $\omega_0$ , as computed using the Bloch equations. The corresponding phase distribution of the transverse spin components is illustrated in figure 1.12.

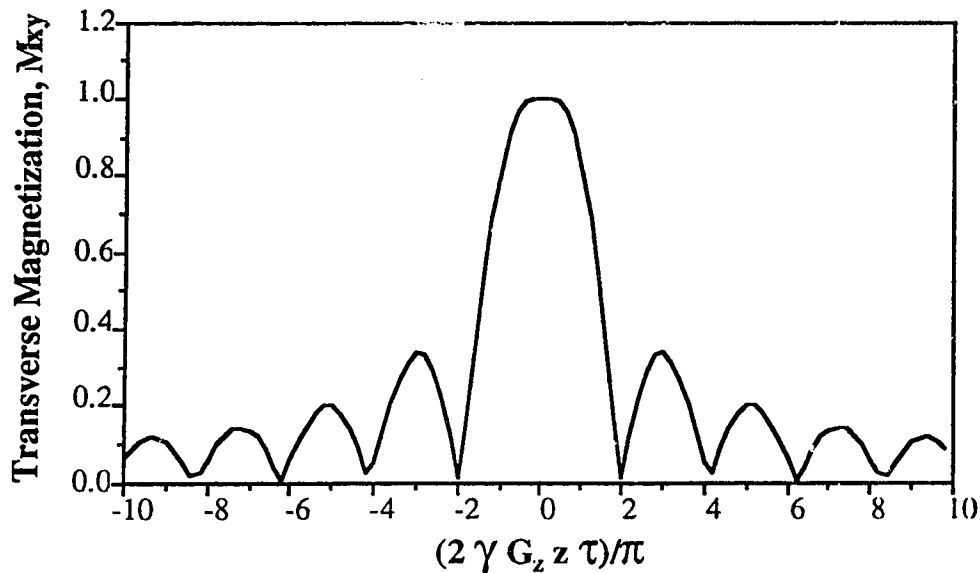


**Figure 1.11** The  $z$  direction variation of the transverse magnetization of a uniform spin system, after the application of a rectangular  $90^\circ$  RF pulse of duration  $2\tau$  in the presence of a magnetic field gradient in the  $z$  direction. The transverse magnetization amplitude has been normalized to equal 1 at  $z = 0$ .

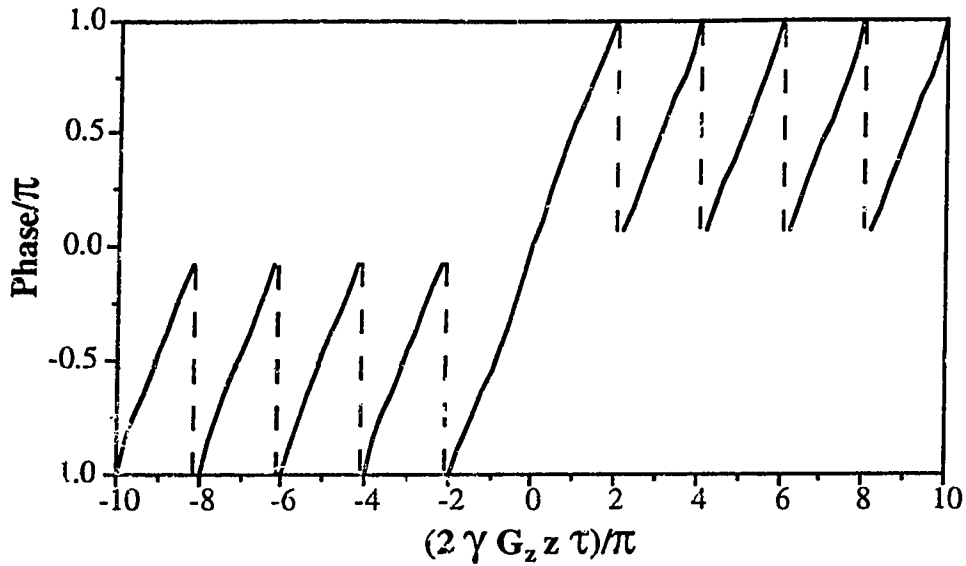


**Figure 1.12** The phase distribution of magnetic moments in the transverse plane, along the  $z$  direction, after the application of a rectangular  $90^\circ$  RF pulse of duration  $2\tau$  in the presence of a magnetic field gradient in the  $z$  direction.

The transverse magnetization distribution resulting from a rectangular  $90^\circ$  RF pulse, as demonstrated in figure 1.11, is obviously unsuitable for imaging purposes because of the multiple bands of excitation. Moreover, as demonstrated by figure 1.12, the spins are roughly linearly distributed in phase so that the net transverse magnetization of the spin system approximates zero. However, Mansfield et al. (48) have shown that the response of a spin system to an RF pulse in the presence of a linear magnetic field gradient is roughly equal to the Fourier transform of the RF pulse envelope. This similarity is also demonstrated by a comparison between the magnetization distribution illustrated in figure 1.11, and the Fourier transform shown in figure 1.13, of a rectangular function with amplitude  $1/2$  and width  $2\tau$ , and provides a clue to the shape of RF pulse that would be required to excite a single band of spins. However, because the response of a spin system to an RF pulse is non-linear (i.e.  $M_{xy}$  is not a linear function of  $B_1$ ), the

similarity between the transverse magnetization distribution and the Fourier transform of the RF pulse envelope is greatest for pulses which rotate the magnetization through a small tip angle,  $\phi$ , such that  $\sin\phi \approx \phi$ , (see equation 1.40) and gets progressively worse as the tip angle increases.

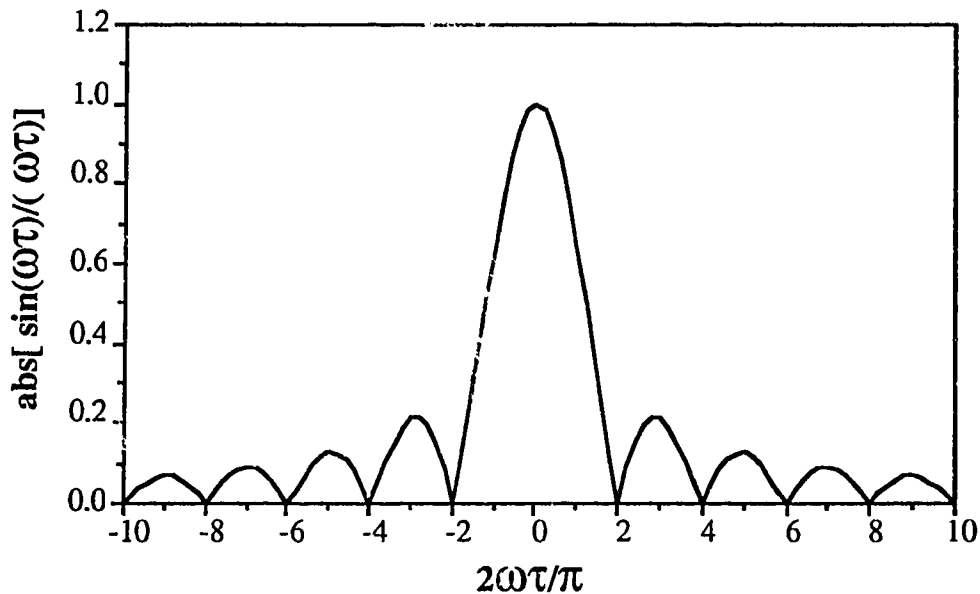


**Figure 1.13** The amplitude of the Fourier transform of a rectangular function with amplitude  $1/2$  and width  $2\tau$ .

The similarity between the transverse magnetization distribution and the Fourier transform of the RF pulse envelope leads one to expect that an RF pulse modulated as a sinc function (i.e.  $\text{sinc}(x) = \sin(x)/x$ , the form of the Fourier transform of a rectangular pulse, as illustrated in figure 1.13) would result in an approximately rectangular transverse magnetization distribution. However, the long duration of a sinc modulated RF pulse ( $\sim 30$  msec may be required) makes it unsuitable for use with the spin-echo imaging of lung alveolar fluid discussed in Chapters 2 and 3 because the faster relaxing component of lung water ( $T_2 \sim 25$  msec) would undergo appreciable transverse relaxation during such a pulse.

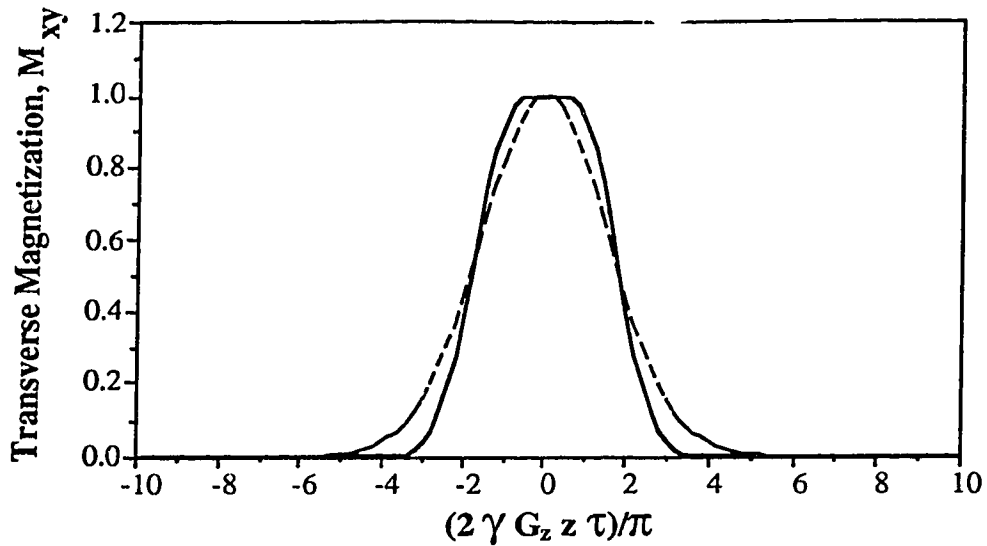


**Figure 1.14** The  $z$  direction variation of the transverse magnetization of a spin system, normalized to 1 at  $z=0$  (solid line), after the application of a Gaussian  $90^\circ$  RF pulse in the presence of a  $z$  direction magnetic field gradient. Also, shown for comparison is a Gaussian function having the same maximum amplitude, and width at half maximum, as that of the transverse magnetization distribution (dashed line).

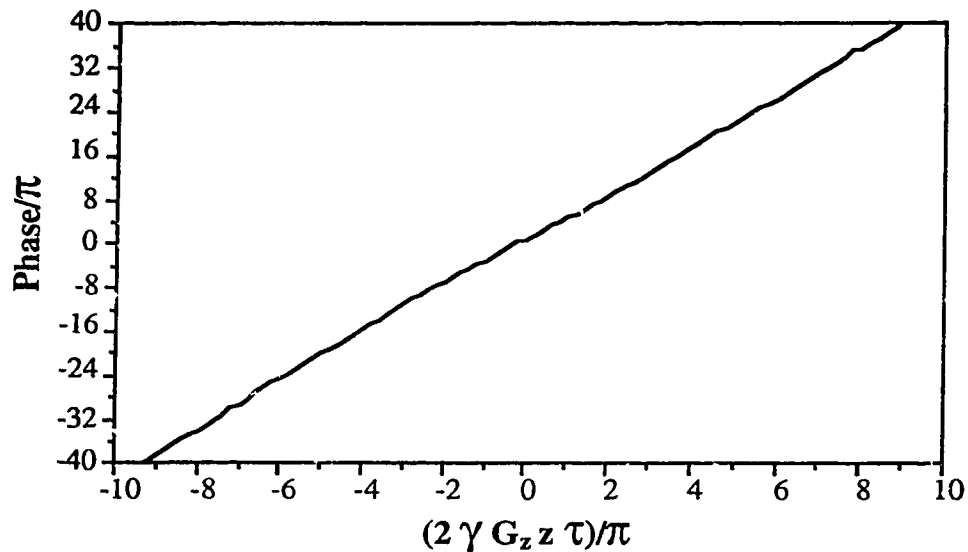


**Figure 1.15** The phase distribution of magnetic moments in the transverse plane, along the  $z$  direction, after the application of a Gaussian  $90^\circ$  RF pulse in the presence of a magnetic field gradient in the  $z$  direction.

A more suitable choice is the much shorter duration Gaussian modulated RF pulse which results in an approximately Gaussian transverse magnetization distribution along the z direction. The actual response of the spin system to a  $90^\circ$  Gaussian pulse, calculated with the Bloch equations, is shown in figures 1.14 and 1.15 as the transverse magnetization distribution, and the phase distribution of the magnetic moments in the transverse plane, respectively. Figure 1.14 also demonstrates a comparison between the transverse magnetization distribution resulting from a  $90^\circ$  Gaussian pulse, and a Gaussian distribution having the same maximum amplitude and width at half maximum. The transverse magnetization distribution along the z axis now has a single band of excitation as desired, with an approximately Gaussian distribution. The phase distribution of the magnetization is again roughly linear and so can be reversed with the application of a gradient pulse of the appropriate amplitude and duration, after the RF pulse has been applied. Because of these desirable properties of the spin system response to Gaussian RF pulses, spatially selective  $90^\circ$  pulses (7.7 msec duration) of this type are employed in the studies described in chapters 2 and 3.

### **A k-Space Representation of NMR Imaging Theory and Image Reconstruction**

Generating an image with the NMR signal from an object requires that the components of the signal, whether as part of an FID or an echo signal, have some dependence on the spatial location of their points of origin. As discussed earlier in this section, the precessional frequency of spins can be made spatially dependent by applying a magnetic field gradient. Also, the relative phase of the spin magnetic moments can be made spatially dependent by applying a magnetic field gradient for

a fixed duration during the sequence. In order to describe the response of the spin system to these space encoding mechanisms we first assume that the magnetization has been rotated from its thermal equilibrium direction onto the  $x_p$  axis by means of a slice defining  $90^\circ$  RF pulse in the presence of a magnetic field gradient in the  $z$  direction. The magnetization,  $m$ , of an isochromat, a small volume element over which it can be assumed that all spins experience that same magnetic field, is then given by equation 1.106.

$$(1.106) \quad m = m_0 \underline{x}_p$$

where  $\underline{x}_p$  is a unit vector along the  $x$  axis in the rotating frame, and  $m_0$  is the initial amplitude of the isochromat magnetization. At a time  $t$  from the onset of the application of a magnetic field gradient,  $G_x$ , in the  $x$  direction, the magnetization of the isochromat is

$$(1.107) \quad m = m_0 [\cos(\gamma G_x t) \underline{x}_p + \sin(\gamma G_x t) \underline{y}_p]$$

However, we choose to express this isochromatic magnetization in a more compact form which is given by

$$(1.108) \quad m = m_0 \exp(i \gamma G_x t)$$

Furthermore, by applying a magnetic field gradient,  $G_y$ , in the  $y$  direction, from time  $t = 0$  to  $t = T_p$ , at which time  $G_y$  is removed and  $G_x$  is applied, the magnetization of the isochromat becomes, at time  $t \geq T_p$

$$(1.109) \quad m = m_0 \exp\{i [\gamma G_x (t - T_p) + \gamma G_y T_p]\}$$

and demonstrates both x and y spatial dependencies. This expression is simplified by the introduction of the coordinates of k-space which are given by

$$(1.110) \quad k_x = \gamma G_x(t-T_p)$$

$$(1.111) \quad k_y = \gamma G_y T_p$$

so that by substitution equation 1.109 becomes

$$(1.112) \quad m = m_0 \exp[i(k_x x + k_y y)]$$

Neglecting relaxation effects, the magnetization  $m_0$  is proportional to the spin density,  $\rho$ , at the isochromat. For any isochromat in the xy plane, the magnetization  $m(x,y)$  is therefore given by

$$(1.113) \quad m(x,y) \propto \rho(x,y) \exp[i(k_x x + k_y y)]$$

Moreover, the NMR signal,  $s(x,y)$ , from an isochromat is proportional to the isochromat magnetization  $m(x,y)$ , and can be expressed as

$$(1.114) \quad s(x,y) \propto \rho(x,y) \exp[i(k_x x + k_y y)]$$

### **Two-Dimensional Fourier Transform Image Reconstruction**

The desired NMR image is a plot of the spin density distribution in the selected image plane, and so  $\rho(x,y)$  is the information that must be extracted from

the NMR signal. Toward this end, the NMR signal,  $S$ , from the entire volume of interest can be obtained by summing over all isochromats as shown in equation 1.115

$$(1.115) \quad S(k_x, k_y) \propto \int_x \int_y \rho(x, y) \exp[i(k_x x + k_y y)] dx dy$$

and can be easily recognized as the two-dimensional (2D) inverse Fourier transform (IFT) of  $\rho(x, y)$  at the position  $(k_x, k_y)$  in  $k$ -space. In order to reconstruct an image from this signal, however, it is necessary to obtain the entire 2D IFT of  $\rho(x, y)$ , and so the signal must be sampled at all values of  $k_x$  and  $k_y$ . This can be accomplished by applying the gradient  $G_x$  during the signal acquisition period over which  $t - T_p$  spans from  $-T_{aq}/2$  to  $T_{aq}/2$ , where the origin has arbitrarily been chosen to be at the center of the acquisition. As a result of this gradient,  $k_x$  is spanned over the range

$$(1.116) \quad k_x = -\gamma G_x T_{aq}/2 \text{ to } +\gamma G_x T_{aq}/2$$

where the separation of sampled points is

$$(1.117) \quad \Delta k_x = \gamma G_x \Delta t$$

In this expression,  $\Delta t$  is the digitization interval used when recording the NMR signal and is also known as DW, the dwell time. If between successive data acquisition steps  $G_y$  is incremented by a constant amount  $\Delta G_y$ , so that over the entire image acquisition period  $G_y$  is spanned from  $-G_{y\max}$  to  $G_{y\max}$ , then  $k_y$  is spanned over the range

$$(1.118) \quad k_y = -\gamma G_{y\max} T_p \text{ to } \gamma G_{y\max} T_p$$

and in this direction of k-space, the separation of sampled points is

$$(1.119) \quad \Delta k_y = \gamma \Delta G_y T_p$$

Thus,  $\Delta k_x$  and  $\Delta k_y$  have constant values, and the sampling of k-space is rectangular as shown in figure 1.16. The RF pulse sequence used to sample k-space in this way is shown schematically in figure 1.17.

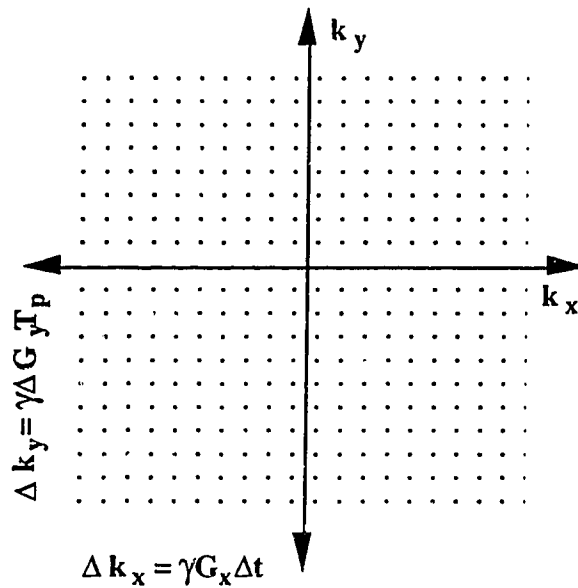


**Figure 1.16** Representation of k-space with rectangular sampling

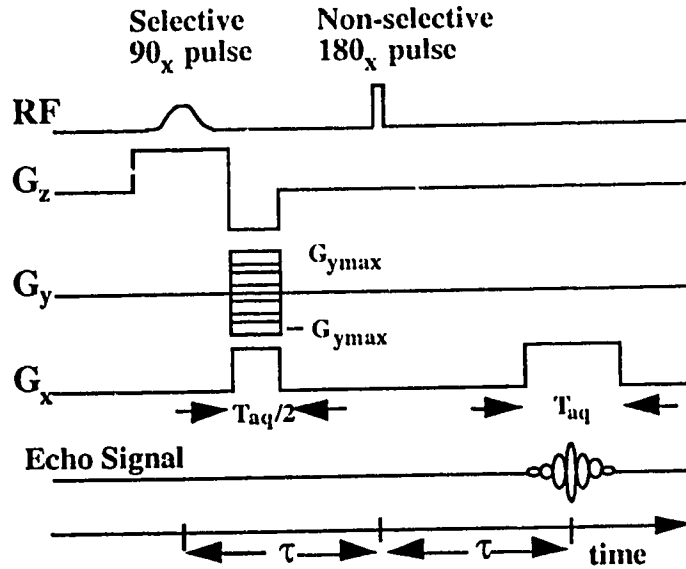


**Figure 1.17** Schematic representation of a pulse sequence for rectangular sampling of the data in  $k$ -space which corresponds to a transverse imaging plane.

The  $k$ -space data represented in figure 1.16 is, in practice, obtained from the NMR signal,  $S(k_x, k_y)$ . Equation 1.115 demonstrates that the spatial dependence of the spin density distribution,  $\rho(x, y)$ , can be obtained from this  $k$ -space data by means of a Fourier transform, as follows

$$(1.120) \quad \rho(x, y) \propto \int_{k_x} \int_{k_y} S(k_x, k_y) \exp[-i(k_x x + k_y y)] dk_x dk_y$$

Although the effects of relaxation have been neglected in this discussion, in practice, relaxation effects provide contrast between image regions depicting different relaxation environments, and can greatly increase the amount of diagnostic information contained in an image. As a result, relaxation effects can be of considerable importance to NMR imaging applications and so should not be overlooked.

Virtually any method of sampling k-space is suitable if the sampling efficiency is not a concern, but in all cases there are constraints which affect the quality of a reconstructed image. Because k-space is sampled at discrete points, the result of the Fourier transform used to reconstruct an image is cyclic. As a result, the highest frequency signal which is sampled must be below the Nyquist frequency to avoid aliasing in the reconstructed image (60). If the desired field of view, FOV, has dimensions X by Y then  $k_x$  and  $k_y$  must be constrained such that:

$$(1.121) \quad \frac{k_{x\max} X}{2} \leq \frac{\pi}{\Delta k_x}$$

$$(1.122) \quad \frac{k_{y\max} Y}{2} \leq \frac{\pi}{\Delta k_y}$$

where  $\Delta k_x$  and  $\Delta k_y$  are the separations of sampled points in k-space. In practice this is usually achieved by using magnetic field gradients with a low enough amplitude that the FOV is larger than the object of interest. This can present another problem, however, because  $\Delta k_x$  and  $\Delta k_y$  are also related to the image resolution that will be achieved as indicated in figure 1.18. Nonetheless, a property of the k-space data that can, in general, be utilized to improve the image quality, is that the higher frequency data points are usually very nearly zero. Points in k-space can therefore be packed with zeroes at frequencies higher than those sampled to effectively increase the number of sample points, N. As a result, the reconstructed image has closer data points but the size of the FOV does not change. This does not, however, improve the actual resolution of the image because this process increases the number of image data points, or pixels, by ideally interpolating points between the original data. As a result, the choice of the magnetic field gradient

magnitudes, the sampling rates, and the number of points to sample to generate an image, must be a balance of the desired resolution, the FOV, and the time to acquire the image data.

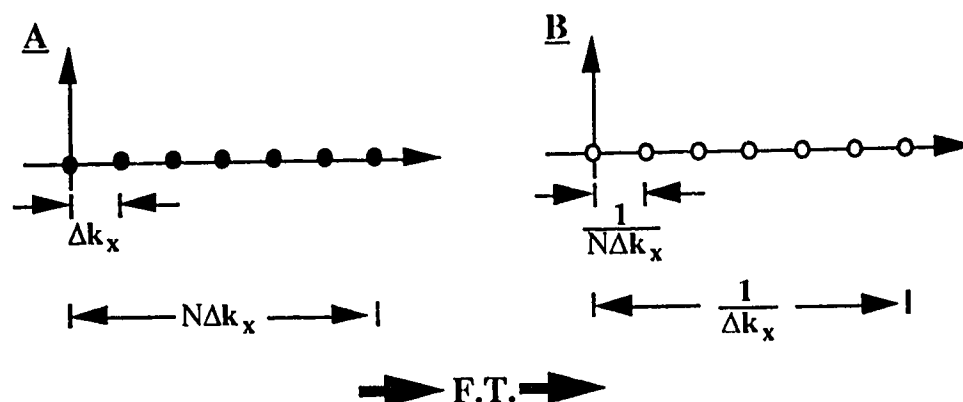


**Figure 1.18** The relationship between the number of sample points and the sampling interval in k-space (A) and the resolution and the size of the FOV of the image (B) which results from applying a Fourier transform to the data in k-space.

### Backprojection Reconstruction

An alternative pulse sequence for sampling k-space is as shown in figure 1.19 in which magnetic field gradients are applied at successively incremented angular displacements around the image plane. With such a pulse sequence k-space can be sampled in radial lines as shown in figure 1.20. An image can be reconstructed from this radially sampled k-space data by interpolating between sampled data points and applying a Fourier transform. However, the interpolation process can be time consuming, and generally requires a number of assumptions to be made about the form of the data in order to predict k-space data values at points which lie between the sampled points in k-space. An image is more readily

reconstructed from radially sampled k-space data by means of a reconstruction from projections technique, as follows (16).

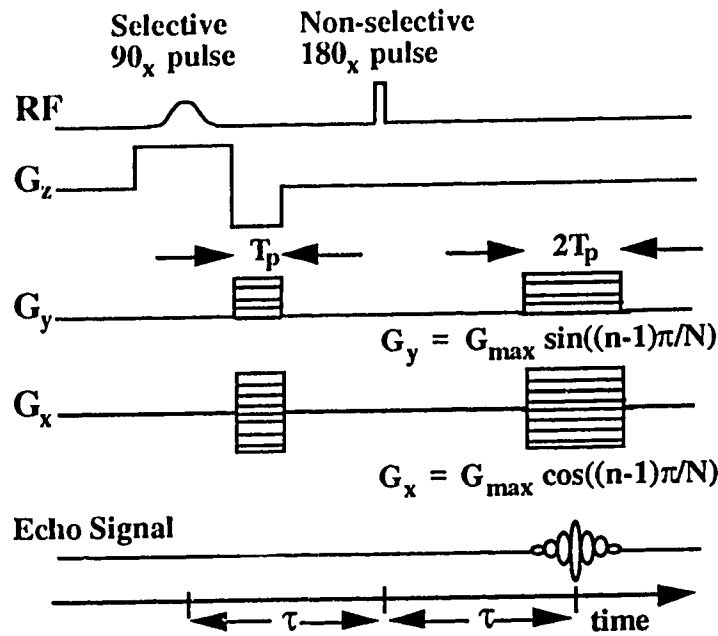


**Figure 1.19** Schematic representation of a pulse sequence for polar sampling of the data in k-space which corresponds to a transverse imaging plane. Values of  $G_x$  and  $G_y$  are expressed for the  $n^{\text{th}}$  of  $N$  data acquisition steps.

Each line of the data represented in figure 1.20 is the inverse Fourier transform of the projection of the signal from the object, onto a line defined by the gradient direction. The signal from such a projection at an angle  $\phi$  from the  $x$  axis is given by:

$$(1.123) \quad S(t, \phi) \propto \int_s \int_r \rho(r, \phi) \exp(i \gamma G_r r t) dr ds$$

where the  $r$ ,  $s$  and  $\phi$  are spatial coordinates as defined in figure 1.21, and  $\rho(r,\phi)$  is the spin density in the image plane, and is therefore the information that is displayed in an image.

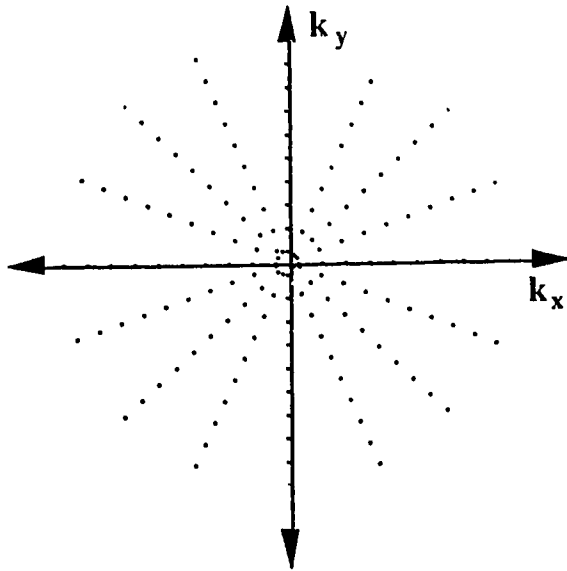


Figure 1.20 Representation of k-space with radial or polar sampling

Equation 1.123 can be simplified by substituting a function,  $g(r,\phi)$ , for the integral in  $s$ , where  $g(r,\phi)$  is the projection of  $\rho(r,\phi)$  onto a line at an angle  $\phi$  from the  $x$  axis, and is given by

$$(1.124) \quad g(r,\phi) = \int_s \rho(r,\phi) ds$$

This substitution yields the expression

$$(1.125) \quad S(t,\phi) \propto \int_r g(r,\phi) \exp(i \gamma G_r r t) dr$$

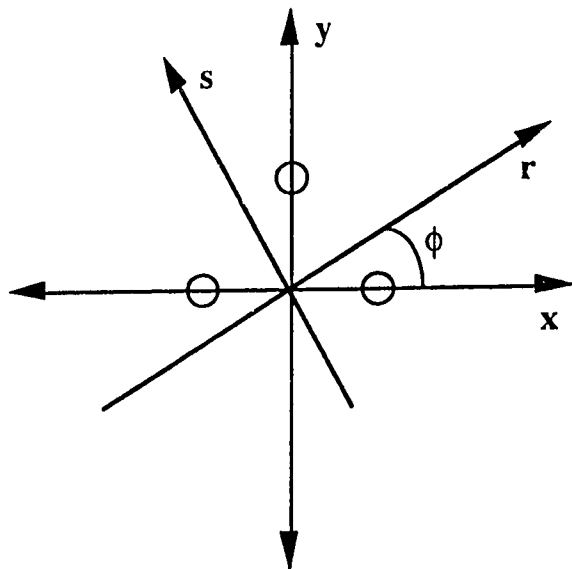


**Figure 1.21** Definition of the coordinates  $r$ ,  $s$  and  $\phi$  for a given signal projection, in terms of the fixed cartesian coordinates,  $x$  and  $y$ .

As with equation 1.109, the substitution to  $k$ -space coordinates can be made such that

$$(1.126) \quad k_r = \gamma G_r t$$

and by substitution equation 1.125 becomes

$$(1.127) \quad S(k_r, \phi) \propto \int_r g(r, \phi) \exp(i k_r r) dr$$

which is the inverse Fourier transform of the projection signal,  $g(r, \phi)$ . The desired image data, however, is proportional to  $\rho(x, y)$  and is given by the Fourier transform of  $S(k_x, k_y)$

$$(1.128) \quad \rho(x,y) \propto \int_{k_x} \int_{k_y} S(k_x, k_y) \exp[-i(k_x x + k_y y)] dx dy$$

and so a change of coordinates is required in order to make use of the signal projection profiles. The variables in the cartesian coordinate system,  $x$  and  $y$ , can be related to those in the polar system,  $r$  and  $\phi$ , as follows

$$(1.129) \quad x = r \cos \phi$$

$$(1.130) \quad y = r \sin \phi$$

and the element of space over which the signal is to be integrated can be related to polar coordinates as shown in figure 1.22.

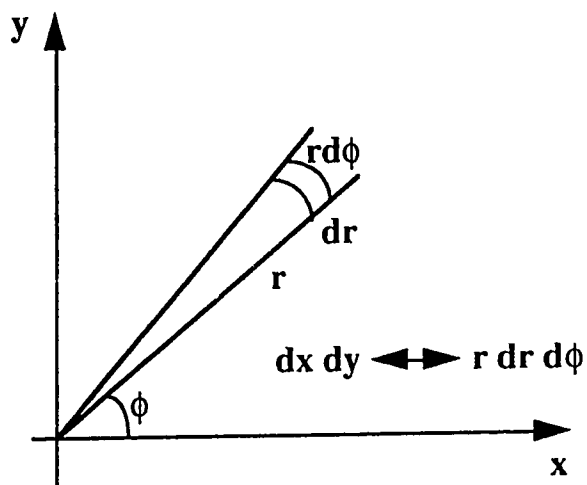


**Figure 1.22** The spatial element of integration as expressed in cartesian and polar coordinates.

Equation 1.128 can thus be converted into polar coordinates to give

$$(1.131) \quad \rho(r, \phi) \propto \int_0^\pi \int_r S(k_r, \phi) \exp(-i k_r r) |r| dr d\phi$$

The inner integral can be recognized as the Fourier transform of  $S(k_r, \phi)$  with respect to  $r$ , with the exception of the term  $|r|$  that has been introduced by the change of coordinates. Relating equation 1.131 to 1.127 one can define a quantity  $g^*(r, \phi)$  with the expression

$$(1.132) \quad g^*(r, \phi) = \int_r |r| S(k_r, \phi) \exp(-i k_r r) dr$$

where  $g^*(r, \phi)$  is the filtered projection of the signal from the object of interest. The image data can then be obtained from the filtered projections by integrating over all of the projection angles

$$(1.133) \quad \rho(r, \phi) \propto \int_0^\pi g^*(r, \phi) d\phi$$

In practice, however, the signal projections can be acquired at only a finite number of projection angles and so the reconstructed image is approximated as

$$(1.134) \quad I(r, \phi) = \sum_{n=0}^N g^*(r, \frac{n\Delta\phi}{N})$$

where  $\Delta\phi$  is the angle between successive projections.

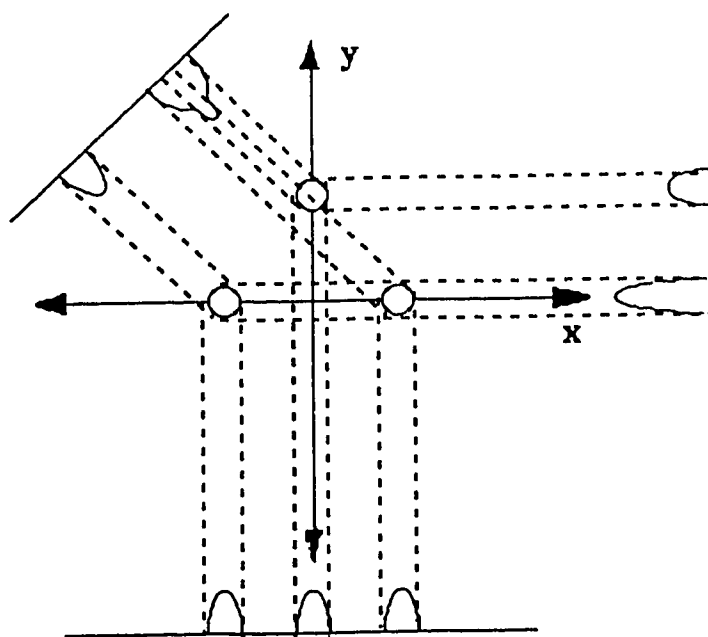


**Figure 1.23** An image plane containing three cylindrical objects and the corresponding projection profiles at three polar angles.

In the work described in Chapter 3, the number of projections used,  $N$ , was 8, whereas the first images published by Lauterbur (40) were reconstructed from only 4 projections, and Bowtell et al. (15) applied back-projection reconstruction to a fast-imaging technique with 64 projections. For an example of this reconstruction technique we look at an image plane containing three cylindrical objects as shown in figure 1.23. When three projections of the signal from these objects are projected back onto the image plane and summed as in equation 1.134, an image is created as shown in figure 1.24. In practice however, many more than three projections are usually required to generate an image. As can be seen in figure 1.24, the difference in signal intensity between the background and the object images increases with more profiles being back-projected, as does the resolution of the image.

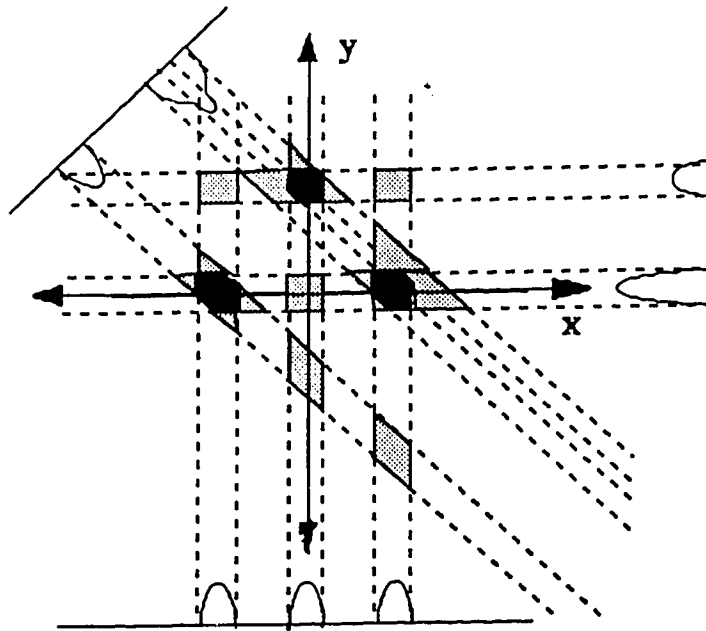


Figure 1.24 The reconstruction of the original image from three projection profiles, back-projected onto the image plane and summed.

In order to estimate the resolution that may be achieved in an image which has been reconstructed by means of a back-projection algorithm, we look at an image plane containing a single circular object of radius  $d$ , and compute the image pixel intensity at a point,  $P$ , a distance  $D$  from the object center, as illustrated in figure 1.25. We can choose this circular object to have a triangular cross section in every plane normal to the  $xy$  plane, so that its intensity projection profile at any angle from the  $x$  axis can be approximated by a triangular function, with amplitude  $I$ , where

$$(1.135) \quad I = \frac{I_0}{d} |r - d| \quad \text{for } -d \leq r \leq d$$

$$(1.136) \quad I = 0 \quad \text{for } |r| > d$$

and where  $I_0$  is the peak profile intensity, and  $r$  is the distance from the profile center.

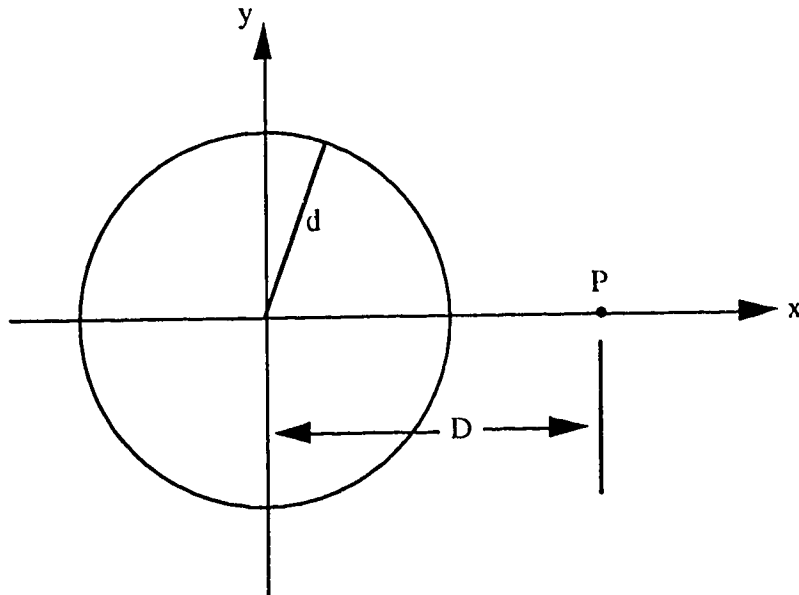


**Figure 1.25** A circular object within an image plane, and definition of the reference point P.

Figure 1.26 illustrates a case in which a single profile has been projected onto the image plane at an angle  $\phi$  from the  $x$  axis. In this situation, the point P is at a distance  $r = D \sin \phi$  from the center line of the projected profile, and the intensity,  $I_P$ , is given by

$$(1.137) \quad I_P = \frac{I_0}{d} (d - D \sin \phi) \quad \text{for } D \leq d / \sin \phi$$

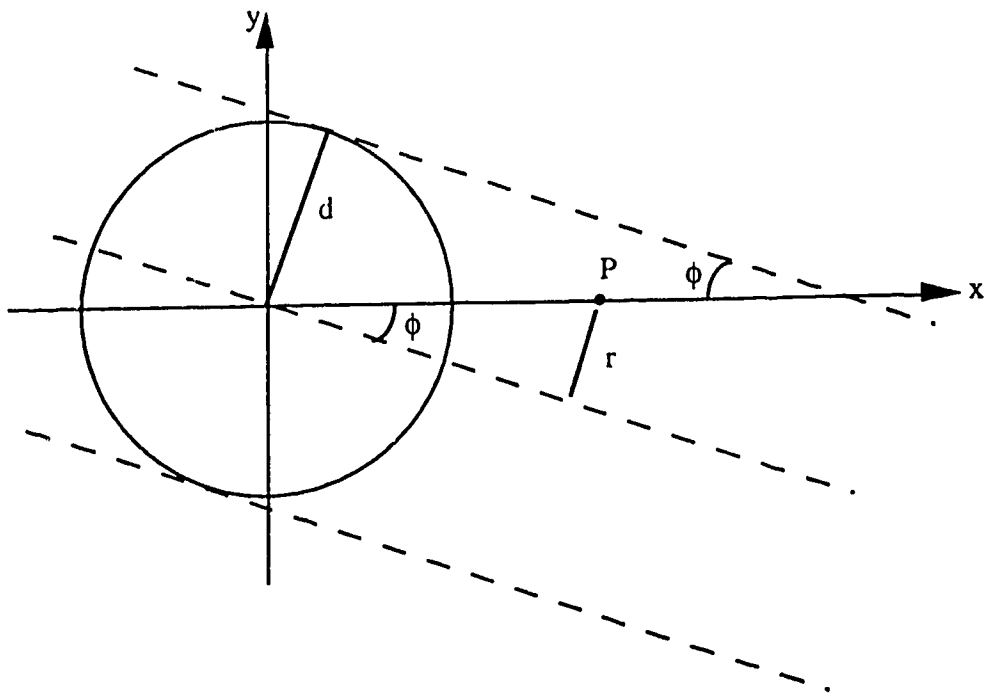


**Figure 1.26** A single intensity profile of the object illustrated in figure 1.25, back projected onto the image plane at an angle  $\phi$  from the x axis. The dashed lines indicate the center line and edges of the back-projected profile.

Because the point P has been chosen to lie on the x axis, after two profiles at angles 0 and  $\pi/2$  radians from the x axis have been back-projected on the image plane, the intensity  $I_P$  is equal to  $I_0$ . The intensity at the object center in this case, is  $2I_0$ . The intensity at point P after N profiles have been projected onto the image plane, however, depends not only on the number of back-projected profiles, but also on the distance D from the object center, and the diameter, d, of the object.

Number of Projections, N	Intensity at point P	
2	$I_0$	$D > d$
	$I_0 + \frac{I_0}{d}(d-D)$	$D \leq d$
4	$I_0$	$D > d/\sin(\pi/4)$
	$I_0 + \frac{2I_0}{d}(d-D\sin(\pi/4))$	$d < D \leq d/\sin(\pi/4)$
	$I_0 + \frac{I_0}{d}(d-D)$	$D \leq d$
	$+ \frac{2I_0}{d}(d-D\sin(\pi/4))$	
8	$I_0$	$D > d/\sin(\pi/8)$
	$I_0 + \frac{2I_0}{d}(d-D\sin(\pi/8))$	$d/\sin(\pi/4) < D$ and $D \leq d/\sin(\pi/8)$
	$I_0 + \frac{2I_0}{d}(d-D\sin(\pi/4))$	$d/\sin(3\pi/8) < D$ and $D \leq d/\sin(\pi/4)$
	$+ \frac{2I_0}{d}(d-D\sin(\pi/8))$	
	$I_0 + \frac{2I_0}{d}(d-D\sin(3\pi/8))$	$d < D \leq d/\sin(3\pi/8)$
	$+ \frac{2I_0}{d}(d-D\sin(\pi/4))$	
	$+ \frac{2I_0}{d}(d-D\sin(\pi/8))$	
	$I_0 + \frac{I_0}{d}(d-D)$	$D \leq d$
	$+ \frac{2I_0}{d}(d-D\sin(3\pi/8))$	
	$+ \frac{2I_0}{d}(d-D\sin(\pi/4))$	
	$+ \frac{2I_0}{d}(d-D\sin(\pi/8))$	

**Table 1.1** Computed intensities at a point P, a distance D from an object of diameter d, after N signal intensity profiles have been projected onto the image plane.

This theoretical intensity,  $I_p$ , at the point P, determined by summing the intensity contributions (computed from equation 1.137) from each of 2, 4, and 8 profiles which are back-projected onto the image plane at equal angular separations, is listed in table 1.1. Figure 1.27 illustrates the computed intensity distribution in an image constructed from each of 2, 4, 8 and 16 back-projection profiles, as well as the theoretical limit that is approached for a very large number of projections. The intensity at the object center after N profiles have been back projected, is equal to  $NI_0$ .

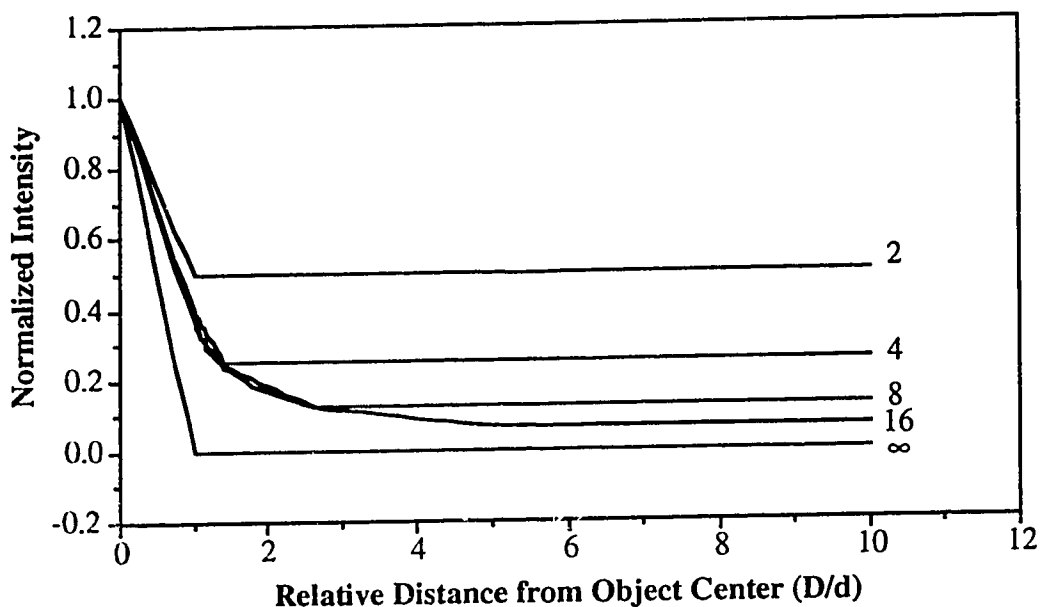


**Figure 1.27** Theoretical intensity profiles for an image of the circular object illustrated in figure 1.25, reconstructed by means of a back-projection algorithm. The intensities were computed with the equations listed in table 1.1. The distance from the object center is expressed relative to the object diameter and the intensities are expressed relative to the intensity at the object center. The number of back-projections represented in each of these curves is indicated on the right.

Figure 1.27 demonstrates the improved image contrast, and improved definition of the object edge, that can be obtained by increasing the number of back-projected profiles. Moreover, because the image intensity near the edge of this object depends both on the size of the object and on the number of back-projected profiles, the ability to resolve two such objects that are in close proximity will depend on these factors as well. The minimum distance between two objects which can be resolved, however, is determined by the separation of data points in the projections themselves, which for the deuteron images discussed in Chapter 3 was approximately 1.6 mm. However, for cases in which the image resolution is greater than the separation of the profile data points, the dimensions of the objects being resolved in an image should be specified for the quoted image resolution to be meaningful.

For the purposes of obtaining deuteron images of instilled alveolar HOD, as discussed in Chapter 3, a back-projection reconstruction from 8 projections provided sufficient image quality, because of the unique nature of this NMR application. Firstly, when imaging the  $^2\text{H}$  distribution in a body there is essentially no detectable NMR signal, with the exception of  $^2\text{H}$  which has been artificially placed into the body. Secondly, the HOD-based solution we instilled into a lung lobe was well localized, and therefore generally provided only one object of interest in our field of view. In this particular situation, the background pixel intensity in the reconstructed image was, at most, only 1/8 that of the pixel intensity of the object of interest, as demonstrated in figure 1.27. Moreover, the resolution achieved in an image reconstructed from 8 projections was estimated from images of 1.3 cm diameter phantoms to be roughly 3 mm, suitable for the purposes of the study discussed in Chapter 3.

#### **1.4 Application of NMR to Studies of Lung Water**

The NMR applications described in Chapters 2 and 3 include proton spin-echo imaging, deuterium FID imaging and deuterium total signal intensity measurements, for monitoring the clearance of fluid which has been artificially introduced into one lung lobe of an anesthetized cat. Chapter 2 discusses a study in which the instilled alveolar fluid is composed of blood serum taken from the cat itself, and Chapter 3 discusses a study in which a serum-like solution containing 50% D<sub>2</sub>O is instilled into the airspaces. In order to monitor the net clearance of alveolar fluid, and to monitor bi-directional fluid fluxes across the pulmonary air-blood barrier, a combination of proton and deuterium NMR techniques were employed.

Proton spin-echo imaging was employed both for first-echo image pixel intensity measurements, and for proton transverse relaxation time measurements, to enable monitoring of water proton environments in the lung. The spin-echo sequence employed was a CPMG sequence in which the selective 90° excitation pulse amplitude was modulated by a Gaussian function in order to define a 1 cm thick transverse imaging plane. Magnetic field gradients were employed to enable rectangular sampling of k-space. Moreover, the signal acquisition was gated to the cat's respiratory motion so that the NMR signal was only sampled when the cat's lungs were at functional residual capacity (FRC). However, the net transverse magnetization immediately after the 90° RF pulse depends on the time that has been allowed for the spin system magnetization to return to thermal equilibrium after the previous 90° RF pulse. As a result, it was necessary to employ "spin-conditioning" in which successive pulse sequences were applied with a constant repetition time,  $T_R$ , regardless of whether the cat's respiratory cycle was at FRC and the NMR

signal was to be sampled. In this way, the transverse magnetization,  $M$ , after each  $90^\circ$  RF pulse did not vary with the cat's respiratory rate but had a constant value given by

$$(1.138) \quad M = M_0[1 - \exp(-T_R/T_1)]$$

where  $M_0$  is the magnitude of the spin system magnetization at thermal equilibrium.

The deuteron imaging technique employed was designed to minimize the time between the  $90^\circ$  excitation pulse and sampling of the NMR signal, thereby minimizing the signal loss due to the rapid deuteron transverse magnetization decay. Deuteron images were obtained by applying non-selective  $90^\circ$  RF pulses and acquiring FIDs in the presence of magnetic field gradients which enabled radial sampling of  $k$ -space. As a result, deuteron images were reconstructed by means of a back-projection algorithm. Deuteron signal intensity measurements were obtained in a similar manner, with the exception that spatial encoding by means of magnetic field gradients was not required. The deuteron images and signal intensity measurement thus acquired, were employed for monitoring the time course of changes in the deuteron content of the lung, after instillation of a serum-like solution containing  $D_2O$ .

As will be discussed in the following chapters, these deuteron and proton NMR techniques have enabled us to obtain time course observations of alveolar fluid clearance, and of fluid absorption and secretion across the pulmonary air-blood barrier. Moreover, these observations were obtained non-invasively, in a living animal, for the first time.

### **1.5 References**

- 1      Abragam A. *The Principles of Nuclear Magnetism*, (Oxford University Press, 1961).
- 2      Barnes P. S. and K. F. Chung, PAF closely mimics pathology of asthma. *TIPS*, **8**, 285 (1987).
- 3      Basset G., C. Crone, G. Saumon, Significance of active ion transport in transalveolar water absorption: a study on isolated rat lung. *J. Physiol.*, **384**, 311-324 (1987).
- 4      Basset G., C. Crone, G. Saumon, Fluid absorption by rat lung *in-situ*: pathways for sodium entry in the luminal membrane of alveolar epithelium. *J. Physiol.*, **384**, 325-345 (1987).
- 5      Bensch K. G., E. Dominguez, A. A. Liebow, Absorption of intact protein molecules across the pulmonary air-tissue barrier. *Science*, **15**, 1204-1206 (1967).
- 6      Bensch K. G., E. A. M. Dominguez, Studies on the pulmonary air-tissue barrier. Part IV: cytochemical tracing of macromolecules during absorption. *Yale Journal of Biol. and Med.*, **43**, 236-241 (1971).
- 7      Bergin C. J., et al., MR imaging of lung parenchyma: a solution to susceptibility. *Radiology*, **183**: 673-676 (1992).

- 8 Berthezene Y., et al., Contrast-enhanced MR imaging of the lung: assessments of ventilation and perfusion. *Radiology*, **183**: 667-672 (1992).
- 9 Berthiaume Y., V. C. Broaddus, M. A. Gropper, T. Tanita, M. A. Matthay, Alveolar liquid and protein clearance from normal dog lungs. *J. Appl. Physiol.*, **65**(2), 585-593 (1988).
- 10 Berthiaume Y., Effect of exogenous cAMP and aminophylline on alveolar and lung fluid clearance in anesthetized sheep. *J. Appl. Physiol.*, **70**(6), 2490-2497 (1991).
- 11 Bethel R. A., et al., Effect of PAF on parasympathetic contraction of canine airways. *J. Appl. Physiol.*, **66**(6), 2629-34 (1989).
- 12 Bloch F., Nuclear induction. *Physical Review*, **70**, 460-485 (1946).
- 13 Bloembergen N., E. M. Purcell, R. V. Pound, Relaxation effects in nuclear magnetic resonance absorption. *Phys. Rev.*, **73**(7): 679-712 (1948).
- 14 Boucher R. C., M. J. Stutts, J. T. Gatzky, Regional differences in bioelectric properties and ion flow in excised canine airways. *J. Appl. Physiol.*, **51**(3), 706-714 (1981).
- 15 Bowtell R., M. G. Cawley, P. Mansfield, Proton chemical-shift mapping using PREP, *J. Mag. Res.*, **82**, 634-639 (1989).

- 16 Brooks R. A. and G. Di Chiro, Principles of computer assisted tomography (CAT) in radiographic and radioisotope imaging, *Phys. Med. Biol.*, **21**: 689-732 (1976).
- 17 Carr H. Y. and E. M. Purcell, Effects of diffusion on free precession in nuclear magnetic resonance experiments. *Phys. Rev.*, **94**, 630-638 (1954).
- 18 Carroll F. E., J. E. Loyd, K. B. Nolop, J. C. Collins, MR imaging parameters in the study of lung water - A preliminary study. *Invest. Radiol.*, **20**, 381-387 (1985).
- 19 Crone C., G. Saumon, G. Basset, News from the alveoli. *NIPS*, **5**, 50-53 (1990).
- 20 Cutillo A. G., et al., Determination of lung water content and distribution by nuclear magnetic resonance. *J. Appl. Physiol.: Respirat. Environ. Exercise Physiol.*, **57**(2), 583-588 (1984).
- 21 Cutillo A. G., et al., Assessment of lung water distribution by nuclear magnetic resonance. *Am. Rev. Resp. Dis.*, **137**, 1371-1378 (1988).
- 22 Drinker C. K. and E. Hardenbergh, Absorption from the pulmonary alveoli. *J. Exp. Med*, **86**, 7-17 (1947).
- 23 Durand J., W. Durand-Arczynska, F. Shoenenweid, Oxygen consumption and active sodium and chloride transport in bovine tracheal epithelium. *J. Physiol.*, **372**, 51-62 (1986).

- 24 Ehman R. L., M. McNamara, M. Pallack, H. Hricak, C. B. Higgins, Magnetic resonance imaging with respiratory gating: techniques and advantages. *Am. J. Roentgenol.*, **143**, 1175-1182 (1984).
- 25 Eisberg R. and R. Resnick, *Quantum Physics of Atoms, Molecules, Solids, Nuclei, and Particles* (John Wiley & Sons, New York, 1985).
- 26 Ewy C. S., J. J. H. Ackerman, R. S. Balaban, Deuterium NMR cerebral imaging in situ. *Mag. Res. Med.*, **8**: 35-44 (1988).
- 27 Frank J. A., Thesis (State University of New York at Stony Brook, 1977).
- 28 Fukushima E. and S. B. W. Roeder, *Experimental Pulse NMR, a Nuts and Bolts Approach* (Addison-Wesley Publishing Co., Reading, 1981).
- 29 Fullerton G. D., J. L. Potter, N. C. Dornbluth, NMR relaxation of protons in tissues and other macromolecular water solutions. *Mag. Res. Med.*, **1**, 209-228, (1982).
- 30 Gadian D. G., *Nuclear magnetic resonance and its applications to living systems*. (Oxford University Press, New York, 1982).
- 31 Goodman B. E. and E. D. Crandall, Dome formation in primary cultured monolayers of alveolar epithelial cells. *Am. J. Physiol.*, **243** (Cell Physiol 2), c96-c100 (1982).

- 32 Goodman B. E., R. S. Fleischer, E. D. Crandall, Evidence for active Na<sup>+</sup> transport by cultured monolayers of alveolar epithelial cells. *J. Physiol.*, **245** (Cell Physiol 14), c78-c83 (1983).
- 33 Goodman B. E., S. E. S. Brown, E. D. Crandall, Regulation of transport across pulmonary alveolar epithelial cell monolayers. *J. Appl. Physiol.: Respirat Environ. Exercise Physiol.*, **57**(3), 703-710 (1984).
- 34 Hahn E. L., Spin echoes. *Phys. Rev.*, **80**, 580-594 (1950).
- 35 Hayes C. E., et al., Lung water quantitation by nuclear magnetic resonance imaging. *Science*, **216**, 1313-1315 (1982).
- 36 Kumar, R., D. J. Hanahan, Diversity of the Biochemical and Biological Behavior of Platelet Activating Factor, Chapter 9 of *Platelet Activating Factor and Related Lipid Mediators*. edited by Fred Snyder, (Plenum Press New York, 1987).
- 37 Kumar, R., R. J. King, H. M. Martin, D. J. Hanahan, Metabolism of platelet activating factor (alkylacetylphosphocholine) by type-II epithelial cells and fibroblasts from rat lungs. *Biochim. Biophys. Acta* **917**: 33-41 (1987).
- 38 Kveder M., G. Lahajnar, R. Blinc, I. Zupancic, Non-brownian water self-diffusion in lung tissue. *Mag. Res. Med.*, **6**, 194-198 (1988).
- 39 Kveder M. et al., Water proton NMR relaxation mechanisms in lung tissue. *Mag. Res. Med.*, **7**, 432-441 (1988).

- 40     Lauterbur P. C., Image formation by induced local interactions: examples employing nuclear magnetic resonance. *Nature*, **242**, 190-191 (1973).
- 41     Lauterbur P. C., Paper presented at the Engineering Foundation Conference on Comparative Productivity of Techniques for Noninvasive Medical Diagnosis, (Henniker, N. H., August 1976).
- 42     Levitzky M. G., *Pulmonary Physiology*, 3<sup>rd</sup> Ed., (McGraw-Hill Inc., New York, 1991).
- 43     Liboff R. L., *Introductory Quantum Mechanics*, (Holden-Day Inc., Oakland, 1980).
- 44     Lim T. P. K., *Physiology of the Lung* (Charles C. Thomas, Springfield, 1983).
- 45     Lorrain P. and D. R. Corson, *Electromagnetic Fields and Waves*, 2<sup>nd</sup> Ed., (W. H. Freeman and Company, San Francisco, 1970).
- 46     MacLennan F. M., M. A. Foster, F. W. Smith, G. A. Crosher, Measurement of total lung water from nuclear magnetic resonance images. *Brit. J. Radiol.*, **59**, 553-560 (1986).
- 47     Mansfield P. and P. K. Grannell, NMR 'diffraction' in solids?, *J. Phys.*, **C6**: L422-L426 (1973).

- 48 Mansfield P., A. A. Maudsley, P. G. Morris, I. L. Pykett, Selective pulses in NMR imaging: a reply to criticism. *J. Mag. Res.* **33**: 261-274 (1979).
- 49 Mason R. J., et al., Transepithelial transport by pulmonary alveolar type II cells in primary culture. *Proc. Nat'l Acad. Sci. USA*, **79**, 6033-6037 (1982).
- 50 Matthay M. A., C. C. Landolt, N. C. Staub, Differential liquid and protein clearance from the alveoli of anesthetized sheep. *J. Appl. Physiol.: Respirat. Environ. Exercise Physiol.*, **53**(1), 96-104 (1982).
- 51 Matthay M. A., Pathophysiology of Pulmonary Edema, *Clin. Chest Med.*, **6**(3), 301-314 (1985).
- 52 Matthay M. A., Resolution of pulmonary edema, *Clin. Chest Med.*, **6**(3), 521-545 (1985).
- 53 Matthay M. A., Resolution of pulmonary edema - New insights. *West J Med*, **154**, 315-321 (1991).
- 54 McFadden R. G., T. J. Carr, I. D. F. Mackie, Thoracic magnetic resonance imaging in the evaluation of HIV-1/AIDS pneumonitis. *Chest*, **101**: 371-374 (1992).
- 55 Meiboom S. and D. Gill, Modified spin-echo method for measuring nuclear relaxation times. *Rev. Sci. Instr.*, **29**(8), 688-691 (1958).
- 56 Muller N. L., Imaging of the pleura. *Radiology*, **186**: 297-309 (1993).

- 57 Muller S. and J. Seelig, In vivo NMR imaging of deuterium. *J. Mag. Res.*, 72: 456-466 (1987).
- 58 O'Flaherty J. T., R. L. Wykle, Metabolic Origin and Fate of Platelet-Activating Factor, *Agents and Actions Supplements Vol. 21: PAF, Platelets and Asthma*. (Birkhauser Verlag Basel, 1988).
- 59 Olver R. E., B. Davis, M. G. Marin, J. A. Nadel, Active transport of  $\text{Na}^+$  and  $\text{Cl}^-$  across the canine tracheal epithelium in-vitro. *Am. Rev. Resp. Dis.*, 112, 811-815 (1975).
- 60 Oppenheim A. V. and R. W. Schaffer, *Digital Signal Processing* (Prentice Hall Inc., Englewood Cliffs, 1975).
- 61 Phillips D. M., J. A. Lunt, S. F. P. Man, P. S. Allen, Multiple spin echo imaging and quantitative relaxation measurements of pulmonary edema. *Mag. Res. Imag.*, 5, 137-147 (1987).
- 62 Phillips D. M., P. S. Allen, S. F. P. Man, Assessment of temporal changes in pulmonary edema with NMR imaging. *J. Appl. Physiol.*, 66(3), 1197-1208 (1989).
- 63 Pinckard R. N., J. C. Ludwig, L. M. McManus, Chapter 10 of *Platelet-Activating Factors, Inflammation: Basic Principles and Clinical Correlates*. (Raven Press Ltd., New York, 1988).

- 64 Scappaticci E., et al., Platelet-activating factor in bronchoalveolar lavage from patients with sarcoidosis. *Am. Rev. Resp. Dis.*, 146: 433-438 (1992).
- 65 Schmidt H. C., M. T. McNamara, R. C. Brasch, C. B. Higgins, Assessment of severity of experimental pulmonary edema with magnetic resonance imaging. *Invest. Radiol.*, 20, 687-692 (1985).
- 66 Schmidt H. C., D. G. Tsay, C. B. Higgins, Pulmonary edema: an MR study of permeability and hydrostatic types in animals. *Radiology*, 158(2), 297-302 (1986).
- 67 Shioya S., et al., Acute and repair stage characteristics of magnetic resonance relaxation times in oxygen-induced pulmonary edema. *Mag. Res. Med.*, 8, 450-459 (1988).
- 68 Shioya S., R. Christman, D. C. Ailion, An *in vivo* NMR imaging determination of multiexponential Hahn T<sub>2</sub> of normal lung. *Mag. Res. Med.*, 16, 49-56 (1990).
- 69 Shioya S., et al., Comparison of *in vivo* and *in vitro* Hahn T<sub>2</sub> measurements in rat lung. *Mag. Res. Med.* 26, 1-6 (1992).
- 70 Shioya S., et al., Nuclear magnetic resonance Hahn spin-echo decay (T<sub>2</sub>) in live rats with endotoxin lung injury. *Mag. Res. Med.*, 29: 441-445 (1993).

- 71 Skalina S., H. L. Kundel, G. Wolf, B. Marshall, The effect of pulmonary edema on proton nuclear magnetic resonance relaxation times. *Invest. Radiol.*, **19**, 7-9 (1984).
- 72 Slichter C. P., *Principles of Magnetic Resonance*, 3<sup>rd</sup> Ed. (Springer-Verlag, New York, 1984).
- 73 Smedira N., et al., Alveolar and lung liquid clearance in anesthetized rabbits. *J. Appl. Physiol.*, **70**(4), 1827-1835 (1991).
- 74 Solomon I., Relaxation processes in a system of two spins. *Physical Review*, **99**(2): 559-565 (1955).
- 75 Staub N. C., Pulmonary Edema, *Physiol. Rev.*, **54**(3), 678-811 (1974).
- 76 Staub N. C., *Basic Respiratory Physiology* (Churchill-Livingstone Inc., New York, 1991).
- 77 Sugahara K., J. H. Caldwell, R. J. Mason, Electrical currents flow out of domes formed by cultured epithelial cells. *J. Cell. Biol.*, **99**, 1541-1546 (1984).
- 78 Tam F. W. K., et al., Inhaled platelet-activating factor causes pulmonary neutrophil sequestration in normal humans. *Am. Rev. Resp. Dis.*, **146**: 1003-1008 (1992).
- 79 Tamaoki J., et al., Angiotensin II-1 receptor-mediated Cl secretion by canine tracheal epithelium. *Am. Rev. Resp. Dis.*, **146**: 1187-1191 (1992).

- 80 Vargaftig B. B., Bronchopulmonary Pharmacology of PAF-acether, Chapter 15 of *Platelet Activating Factor and Related Lipid Mediators*. (Plenum Press New York, 1987).
- 81 Webb W. R. and H. D. Sostman, MR imaging of thoracic disease: clinical uses. *Radiology*, 182: 621-630 (1992).
- 82 West J. B., *Respiratory Physiology - the Essentials* (Williams & Wilkins Co., Baltimore, 1974).
- 83 Wexler H. R., et al., Quantitation of lung water by nuclear magnetic resonance imaging. *Invest. Radiol.*, 20, 583-590 (1985).

## **2.0 Evaluation of the Effects of PAF on Alveolar Fluid Clearance Using NMR Imaging.<sup>1</sup>**

### **2.1 Introduction**

Although proton nuclear magnetic resonance (NMR) imaging is particularly suited to studies of the soft tissues in the body, image quality is greatly limited in *in-vivo* lung studies by the paucity of water protons and by susceptibility problems, as well as by artifacts caused by respiratory motion, cardiac motion, and pulsatile blood flow. However, the NMR signal intensity, depending as it does on three parameters, namely, the local proton density,  $\rho$ , the longitudinal relaxation time,  $T_1$ , and the transverse relaxation component,  $T_2$  (1) can also provide important information through the relaxation times. These times have been shown to be sensitive to the water content of tissue (16, 29), the mobile protein content of fluid (10, 20) and air-fluid interfaces (15).

Incorporating techniques to reduce artifacts and increase sensitivity, NMR signal intensity measurements, both in excised lungs (7) and *in-vivo* (8, 25), have been shown to be well correlated with gravimetric lung water measurements. Relaxation times of lung water protons have also been shown to be well correlated with gravimetric measurements (29) and have been used to differentiate between hydrostatic and permeability edema (25). Moreover, in normal rat lungs *in-vivo*, two transverse relaxation components have been demonstrated (27). In only a few

---

<sup>1</sup> A version of this chapter has been accepted for publication. P. W. Stroman, P. S. Allen, D. C. Lien, G. Machin, S. F. P. Man. Evaluation of the Effects of PAF on Alveolar Fluid Clearance Using NMR Imaging. Journal of Applied Physiology.

cases, though, were both quality images and relaxation time measurements obtained (23, 25) or were NMR techniques applied to monitor serial changes in lung water (8, 23, 27). One purpose of this study was to improve on the quality of both the images and the relaxation time measurements of alveolar fluid protons, so that modifications to the time course of alveolar fluid clearance by the administration of platelet-activating factor could be studied *in-vivo*.

Platelet-activating factor (PAF) is a family of ether-lipids whose active component is 1-O-Hexadecyl/octadecyl-2-acetyl-sn-glycero-3-phosphocholine (24). PAFs are produced by a wide variety of cells in the body (21, 24) including alveolar type II epithelial cells (13, 14). It has been shown that intra-airway PAF can cause bronchoconstriction (3) and inflammation in the airways and capillary spaces (30). Because the role of PAF in the development and/or resolution of pulmonary edema has not been previously evaluated, we studied the effects of PAF at a dosage that is comparable to that used in studies of the effects of PAF on lung endothelial and epithelial permeability (5, 9).

Our findings, using all the NMR parameters at our disposal, were that the addition of PAF to instilled alveolar fluid dramatically increased water clearance from the lung but had little or no effect on the clearance of albumin from the lung. From the gravimetric and NMR data acquired at the end of the experimental time course, we were able to demonstrate a correlation between NMR intensity measurements and gravimetric measurements of the instilled alveolar fluid, both when serum was instilled ( $p > 0.40$ ) and when serum plus PAF was instilled ( $p > 0.15$ ), where the  $p$  values quoted are the results of unpaired, 2 tailed,  $t$  tests. This correlation plot had a slope of 0.95 and a regression coefficient,  $r$ , of 0.74 ( $n = 6$ ).

## **2.2 Methods**

### **2.2.1 Animal Model Of Alveolar Fluid Clearance**

We have studied alveolar fluid clearance in anesthetized mongrel cats (3.0-6.0 kg body wt.) using a model similar to that described by Matthay et al. for the sheep (Matthay 1985). The cat was anesthetized with an intramuscular injection of ketamine (Ketalean 25 mg/kg), xylazine hydrochloride (Rompun 0.5 mg/kg) and acepromazine (Atravet 1 drop/4 kg). Anesthesia was maintained with the same mixture as required (~ 25% initial dose/hour). The supine cat was intubated, but breathed spontaneously. Polyethylene catheters (PE-90, o.d. 1.27 mm) were placed in an external jugular vein and a femoral artery for the administration of fluids and hemodynamic monitoring.

A 7-10 ml sample of venous blood was taken from the animal in order to prepare 4 - 5 ml of serum. The instillate was prepared from this serum by adding 1 mg of Evan's Blue dye and 3  $\mu$ Ci of  $^{125}$ I-albumin (Merck Frosst, Kirkland Quebec) to label the instilled albumin. For experiments which included PAF, 250  $\mu$ l of  $10^{-5}$  M PAF was also added to the serum just prior to instillation; a dose range of 0.17 to 0.31  $\mu$ g PAF/kg body weight was used (mean = 0.23  $\mu$ g PAF/kg). The volume of solution instilled into the lung was 0.7 ml/kg body weight and the remaining aliquot (1 ml) was used for  $^{125}$ I and water content determinations.

Prior to fluid instillation, the cat was ventilated manually 6 - 7 times with a tidal volume of 10 ml/kg body weight. A PE-90 catheter was inserted into a lower lung lobe (right lung, 27 times out of 36 experiments) and the fluid was injected with a syringe over 15 sec, followed by the insufflation of several ml of room air.

The precise amount of fluid instilled was determined by weight. NMR imaging and/or gravimetric analysis of the lung were then carried out, as described below, during the succeeding four hour period.

Five minutes prior to the end of the experiment the cat was given 5000 units of heparin intravenously. Just before the cat was sacrificed, venous blood samples were taken for determinations of hematocrit, blood density, hemoglobin content, and  $^{125}\text{I}$  and fractional water contents. The chest was opened with a mid-line sternotomy and the lungs were tied off at the hila and removed. The distribution of the instilled fluid in the experimental lobe was identified by the Evan's Blue dye.

The lung lobes were processed to determine the clearance rates of liquid and  $^{125}\text{I}$ -albumin (17). The lobes were weighed, added to a known amount (~100 g) of distilled water, homogenized, and half of the homogenate was centrifuged to obtain a clear red supernatant. The fractional water content of the homogenate, and  $^{125}\text{I}$  iodide, fractional water content, density, and hemoglobin content of the supernatant, were determined for each lobe. We computed the total weight of blood in each lobe using the calculations described by Pearce et al. (22) but we did not include a correction factor for pulmonary hematocrit. Within these calculations, we computed the hemoglobin concentration in the homogenate from the measured hemoglobin concentration in the supernatant as was done by Selinger et al (26).

To avoid interference from Evan's Blue dye the cyanmethemoglobin concentration in the supernatant was determined from the light absorbance at 420 nm instead of the usual 540 nm. Using this absorbance, Evan's Blue dye at a concentration of 1 mg/4 ml did not interfere with the measurement of hemoglobin, and was accurate to within 3% for hemoglobin concentrations of less than 0.1

mg/dL. The concentration of dye in the supernatant in these studies was typically in the order of 0.002 mg/ml.

The amounts of  $^{125}\text{I}$ iodide in the blood samples, instillate, homogenate samples and supernatant samples were determined with gamma counts of samples with uniform geometry using a LKB Wallac, model 1282 Compugamma. The counts were corrected for background, counter dead time and isotope decay.

Fractional water contents of samples were determined by weighing the samples before and after drying to a constant weight.

The number of cats included in each experimental group is listed in Table 2.1. Whereas data from NMR measurements were consecutive 45 minute averages that serially spanned a 4 hour period, the gravimetric measurements provided only discrete data points and so were obtained at either 1 hour or 4 hours after fluid instillation to allow comparison to the NMR data. Cats which received serum formed the control study group, cats which received serum plus PAF formed the first experimental study group, and cats which received serum plus lyso-PAF, a biologically inactive form of PAF, formed the second experimental study group. Each of these study groups is further subdivided in Table 2.1 into a 1 hour sacrifice and a 4 hour sacrifice subset, although in the 1 hour subset only 4 cats were studied, 2 were given serum and 2 were given serum plus PAF. Moreover, this 1 hour subset was only evaluated gravimetrically, leaving the early NMR data points to be obtained from the 4 hour subset.

Table 2.1 shows how the aforementioned study groups were further subdivided into those evaluated gravimetrically, those evaluated by NMR, and those

evaluated by both methods. In addition, 8 cats were assessed for histology (2 for saline, 3 each for autologous serum plus Evan's Blue dye and autologous serum plus Evan's Blue dye plus PAF) so that morphological changes in the lung caused by the experimental procedure, or by PAF, might be detected. The excised lungs were fixed in 2.5% glutaraldehyde and 1.5% formaldehyde in a sodium cacodylate buffer, osmolarity 295 mOsmol/kg H<sub>2</sub>O and pH of 7.4.

Data Obtained	Serum Instilled		Serum+ PAF Instilled		Serum + Lyso-PAF Instilled	Saline Instilled	
	1 hour	4 hours	1 hour	4 hours	4 hours	1 hour	4 hours
NMR only	0	2*	0	1	0	0	0
Gravimetric only	2	6	2	5	2	0	0
NMR and Gravimetric	0	3	0	4	1	0	0
Histology	1	2	1	2	0	1	1

\*One cat had 2 lung regions containing fluid monitored with multi-slice imaging, so 3 fluid clearance curves were obtained for this group

Table 2.1 The number of cats included in each of the experimental groups

### 2.2.2 NMR Imaging

Imaging was carried out on a modified Bruker CXP spectrometer (Bruker Instruments Inc. Billerica, MA) with a 40 cm bore magnet at a static field,  $B_0$ , of

2.35 T. The anesthetized supine cat was supported by a curved plexiglass tray inside the magnet bore. Hydrogen nuclei in a 1 cm thick transverse imaging slice were excited uniformly with selective radio frequency (RF) pulses transmitted by a large circumscribing coil. To provide high receiver sensitivity in the dorsal half of the thorax, a single turn rectangular surface coil (4 cm x 15 cm), curved around the thorax, served as the receiver. To avoid inductive coupling between the two coils, active switching to the proton resonant frequency, under the control of the pulse program, was employed between transmission and data acquisition. Respiratory gating was brought about by means of a flexible rubber bellows placed around the cat's abdomen and linked to a pressure transducer whose analog output was converted to TTL for triggering the pulse programmer. The pulse sequence was applied at regular intervals, regardless of the cat's breathing, but the NMR signal was only acquired when the cat's thorax was at functional residual capacity (FRC).

Our imaging pulse sequence (Figure 2.1) was based on a Carr-Purcell-Meiboom-Gill (CPMG) train of pulses (19) which had been modified for respiratory gating and multi-slice imaging. The selective  $90^\circ$  RF pulse was gaussian shaped with a 7.68 msec duration whereas the non-selective  $180^\circ$  RF pulses were square pulses, each with a duration of 350  $\mu$ s. The inter-echo interval,  $T_E$ , was 26.3 msec, and each of the spin-echo signals was acquired to form a series of spin-echo images. Four signal acquisitions with a repetition time,  $T_R$ , of 1.0 sec were averaged to improve the signal to noise ratio. The data set for each spin-echo image, acquired as a 64 x 256 matrix, was zero-filled to create a 128 x 256 matrix which was Fourier transformed to create a 128 x 256 pixel image (10 cm x 20 cm field of view).

Sets of 8 spin-echo images were obtained for each of 4 contiguous slices. The slices were interleaved in non-contiguous pairs thus allowing us to image the entire caudal half of the thorax every 30 to 40 minutes.

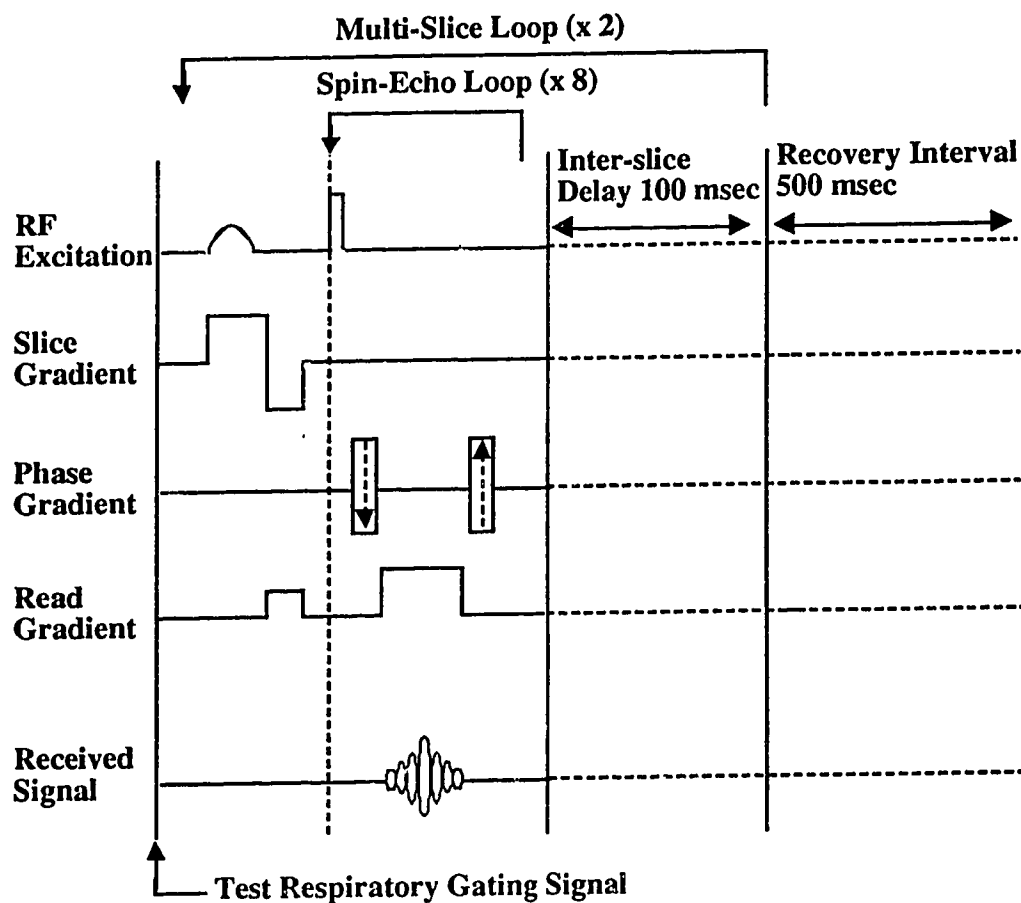


**Figure 2.1** Schematic of the pulse sequence used to obtain 8 spin-echo images of each of 2 non-contiguous slices. The TTL respiratory gating signal indicates when the cat's lungs are not at FRC. In this case, spin conditioning takes place and no gradients are applied and the NMR signal is not acquired.

The lungs were imaged before the instillation of serum solution into one lung lobe, and then continuously over the subsequent 4 hour period. The first spin-

echo image of each set was used for monitoring the lung water content. Rectangular regions of interest were defined using a grid as shown in Figure 2.2, with each region typically containing 300 to 400 pixels (1.5 to 2.0 cc). Most of the fluid-filled lung lobe fell into one of these regions and the equivalent part of the contralateral control lobe was also arranged to be a region of interest. Several regions of interest were analyzed, namely, the experimental lung lobe, the contralateral control lobe and several adjacent regions of the chest wall and back. Each region of interest was then characterized by the sum of the pixel intensities in that region. The background intensity,  $I_{BG}$ , was calculated from the set of control images taken prior to instillation, and subtracted from the total intensity of the fluid filled lung lobe region to determine  $I_{Inst}$ , the intensity of the NMR signal produced by the instilled fluid in the lung lobe. The calculated  $I_{Inst}$  values were then plotted as a function of the time,  $\Delta t$ , between instillation of the fluid and the mid-point of the image acquisition period. Because the fluid clearance over 4 hours was non-linear in general, the value of  $I_{Inst}(\Delta t=0)$  was approximated by linear extrapolation from the two values of  $I_{Inst}(\Delta t)$  closest to  $\Delta t=0$ . The estimated value of  $I_{Inst}(\Delta t=0)$  was used to normalize the time course of the fluid clearance from the lung lobe.

The same regions of interest were also used for transverse relaxation time measurements. Using the total pixel intensity of the chosen region, the eight spin-echo images provided a decay curve for the region-of-interest magnetization, from which average transverse relaxation time components were derived for that region using a non-linear least squares algorithm (4).

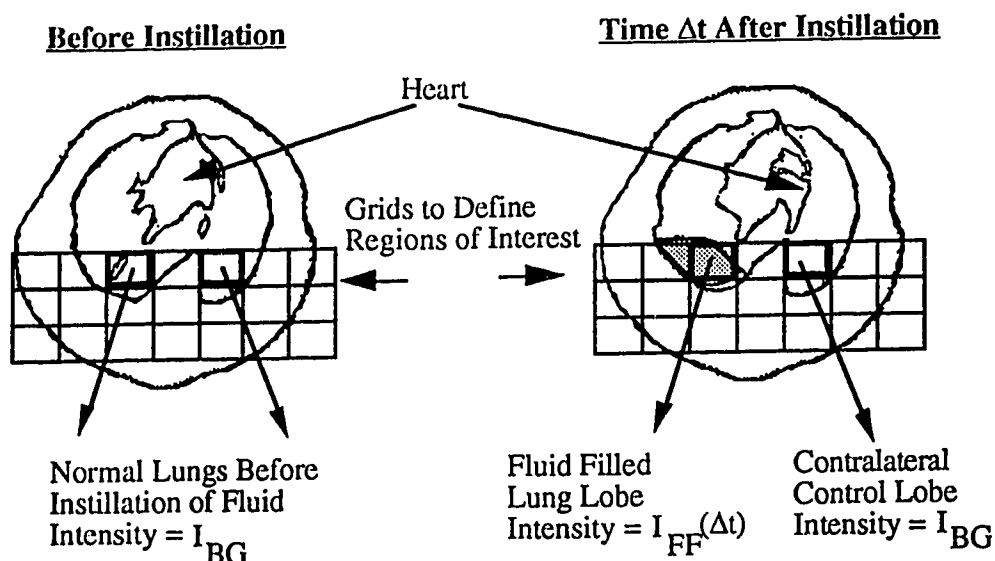


**Figure 2.2** The method used for defining regions of interest in transverse images of a cat's thorax. Only the first spin-echo images are used for monitoring the time course of changes in the lung water content. The intensity of the acquired signal which is due to the instilled fluid is given by:  $I_{inst}(\Delta t) = I_{FF}(\Delta t) - I_{BG}$ .

## 2.3 Results

Examples of NMR images obtained before and after instilling fluid into a cat's lower lung lobe are shown in Figures 2.3a to 2.3d. The time dependence of the integrated instillate NMR signal intensity data,  $I_{Inst}$ , grouped into 45 minute interval averages, is shown in Figure 2.4. For comparison, results of gravimetric measurements obtained at 1 and 4 hours after fluid instillation, are also shown. All of the results are expressed as the mean of  $n$  experiments, plus or minus the standard error of the mean. For the serum instillate, the integrated NMR intensity data showed that  $86\% \pm 6\%$  ( $n=6$ ) remained in the experimental lung lobe between 3.25 and 4 hours after instillation, which compared favorably to gravimetric measurements of  $78\% \pm 6\%$  ( $n=9$ ) at 4 hours after instillation. With PAF added to

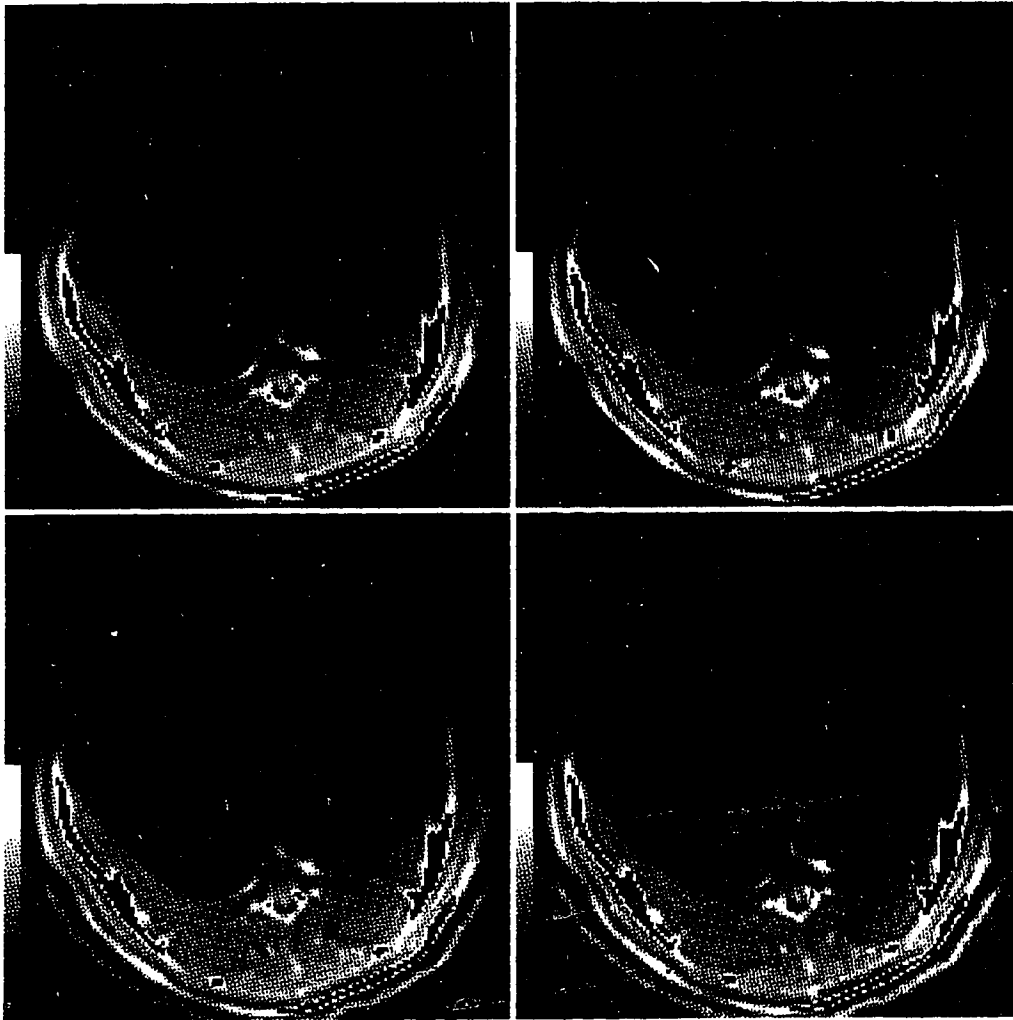
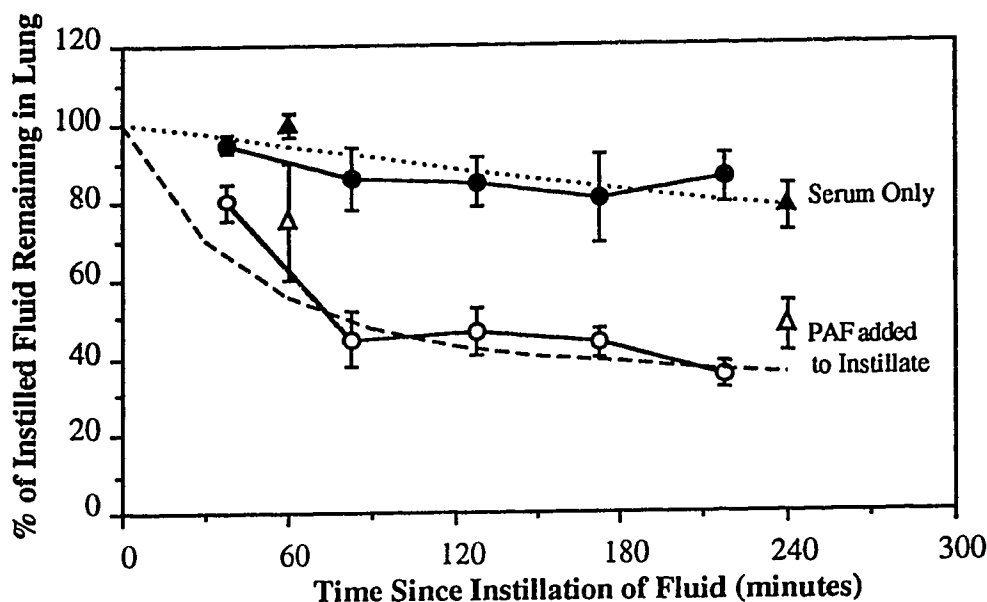


Figure 2.3 Transverse images of a cat's thorax; a) before instillation of fluid (upper left), b) 20 minutes after instillation of fluid (upper right), c) 120 minutes after instillation of fluid (lower left), and d) 200 minutes after instillation of fluid (lower right).

the instillate, the integrated NMR intensity data revealed that only  $35\% \pm 4\%$  ( $n=5$ ) remained in the lung lobe between 3.25 and 4 hours after instillation, compared to a measurement of  $47\% \pm 6\%$  ( $n=9$ ) after 4 hours from the gravimetric method. That the addition of PAF to the instillate dramatically increased fluid clearance over a 4 hour period was demonstrated by both measurement techniques. The addition of PAF to the serum instillate introduced a bi-phasic character to the water clearance which could be readily detected from the sequential NMR images. The fast clearance phase had a  $t_{1/2}$  of approximately 30 min, whereas the slow clearance rate was similar to the clearance rate for serum alone with a  $t_{1/2}$  of approximately 670 min.



**Figure 2.4** The time course of alveolar fluid clearance as determined by *in-vivo* NMR imaging and by gravimetric measurements of excised lungs. Circles indicate averaged NMR intensity data (serum  $n = 6$ , serum plus PAF  $n = 5$ ). Triangles indicate averaged gravimetric measurements (each group: 1 hour  $n = 2$ , 4 hours  $n = 9$ ). The dotted line shows the fitted clearance curve without PAF: % Remaining =  $100\exp(-t/966)$ . The dashed line shows the fitted clearance curve with PAF: % Remaining =  $55\exp(-t/40) + 45\exp(-t/966)$ .

When lyso-PAF was added to the instillate it did not appear to affect fluid clearance; gravimetrically,  $71\% \pm 19\%$  ( $n=3$ ) of the instilled water remained after 4 hours. NMR registered a corresponding value of approximately 90% ( $n=1$ ).

The amount of  $^{125}\text{I}$ -albumin (in the gravimetric groups) remaining in the experimental lung lobe after 4 hours suggests that the introduction of PAF decreased the residual  $^{125}\text{I}$ -albumin from  $91\% \pm 3\%$  ( $n=9$ ) with pure serum instillate to  $82\% \pm 5\%$  ( $n=9$ ) when PAF was added. Nonetheless, the significance of this discrimination is low ( $p = 0.06$ ). The amount of radioactivity we were able to recover was  $\geq 90\%$  (range 90% to 100%) of that instilled, and the amount present in the thyroid (as an index of free radioiodine) was negligible ( $<0.01\%$ ). We were therefore confident that leaching of the isotope from radiolabelled albumin was minimal.

The decay of the proton transverse magnetization from the region of interest in the fluid-instilled lung could be reproducibly resolved into two exponential components, with characteristic times  $T_{2F}$  (fast relaxing) and  $T_{2S}$  (slow relaxing). Measurements of  $T_{2F}$  and  $T_{2S}$ , again time averaged over the intervals used for the integrated signal intensity averaging (45 minutes), are shown as a function of time following instillation in Figure 2.5. It is clear from this figure that any differences in  $T_{2F}$  due to PAF addition to the instillate are too small to be resolved throughout the 4 hours of measurement. Resolution of the PAF induced differences in  $T_{2S}$  appears to be marginal, however the uncertainties were too large to claim a significant difference. Throughout the 4 hour observation period the more slowly relaxing  $T_{2S}$  component accounted for approximately 40% of the lung proton signal

in the region of interest, irrespective of whether serum or serum plus PAF was instilled.

Arterial blood gases, pH and blood pressure were monitored in experiments in which only gravimetric measurements were obtained. All of these monitored parameters were found to be stable and without systematic change throughout the course of the experiments.

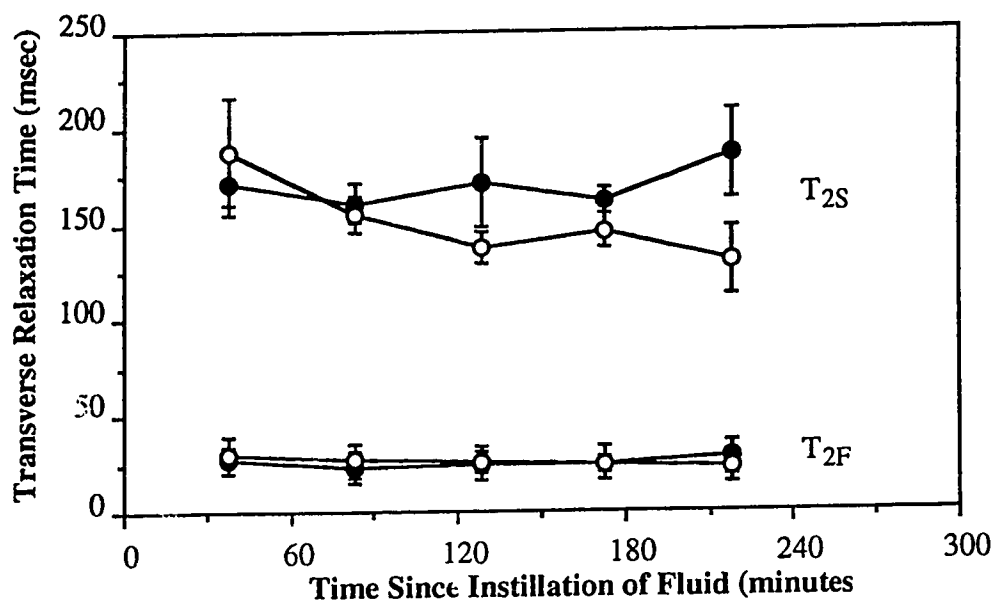


**Figure 2.5** The time dependence of the time averaged transverse relaxation times of cat lungs containing instilled fluid. The filled circles represent serum instilled into the lungs. The open circles represent serum plus PAF instilled into the lungs.

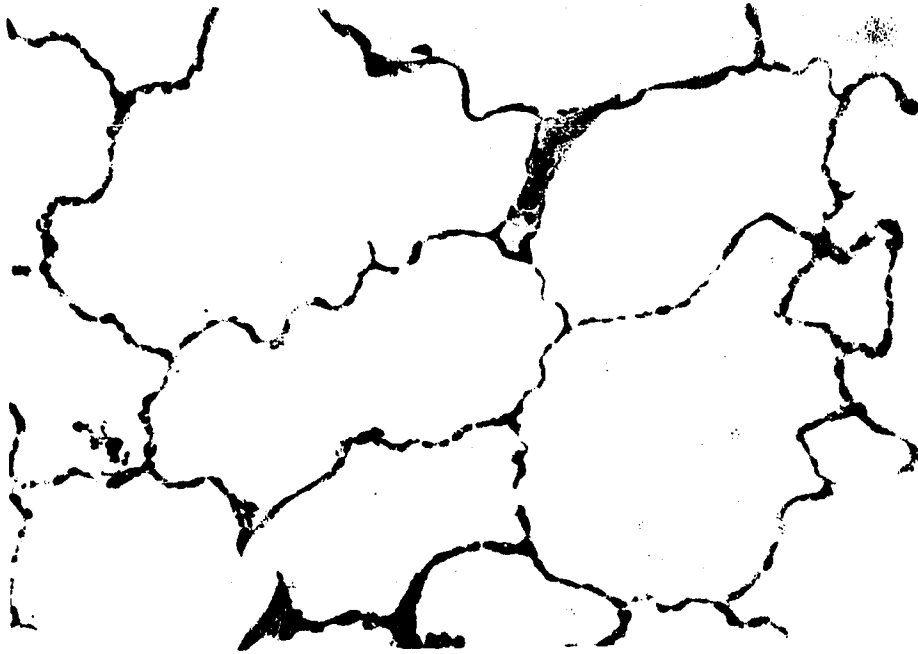


Figure 2.6a Photomicrograph of cat lung, 4 hours after instillation of autologous serum plus PAF.

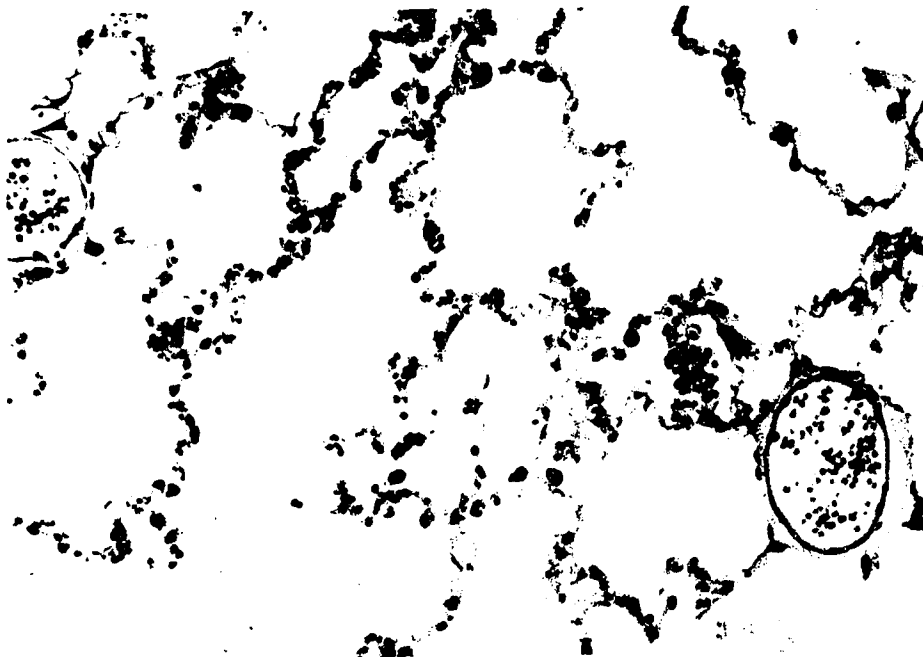


Figure 2.6b Photomicrograph of cat lung, 4 hours after instillation of autologous serum.

Histological sections of lungs, examined in a single blind fashion, made at 1 and 4 hours after instillation of saline plus dye showed no gross morphological evidence of inflammation, and verified that instillate was delivered to the alveoli. An accumulation of neutrophils in the vascular spaces was observed irrespective of whether the instillate was either serum or serum plus PAF, but no accumulation of neutrophils in the airspaces or interstitium could be detected. Photomicrographs of the PAF treated lungs in Figure 2.6a do not demonstrate any excess of fluid in the interstitium or vascular spaces, while the non-PAF treated lungs in Figure 2.6b show distended alveolar capillaries and venules.

## **2.4 Discussion**

The NMR images we have obtained have enabled us to observe, non-invasively, the time course of lung alveolar fluid clearance in living cats. After the instillation of either serum, or serum plus lyso-PAF into the airspaces, we observed a mono-phasic clearance with a half time ( $t_{1/2}$ ) of approximately 11 hours. In comparison, as summarized by Matthay et al. (18), alveolar liquid clearance in dogs, sheep and rabbits proceeds with an estimated  $t_{1/2}$  of 18 hours, 9 hours and 6 hours respectively. With the addition of PAF to the instilled fluid, however, we observed a dramatic change to the nature of the fluid clearance from the alveolar space of the cat. With PAF the clearance was bi-phasic, having an initial rapid clearance with a  $t_{1/2}$  of approximately 30 minutes followed by a clearance which was similar to that observed when either serum or serum plus lyso-PAF was instilled.

The clearance of protein from the alveolar space was seen to proceed at a much slower rate than that of the alveolar fluid itself, independent of the species studied. Protein clearance has been reported to be 1%/hour in sheep (17) and

2%/hour in the anesthetized dog (30). In cats we observed an alveolar  $^{125}\text{I}$ -albumin clearance rate of 2.3%/hour when serum alone was instilled, and this clearance did not appear to have been significantly altered by PAF.

The influence of PAF on the fluid and protein clearances, as well as that of lyso-PAF, which has similar biochemical but not biological properties, can be better but not totally understood from our data. With PAF, there was no significant increase in albumin clearance, leading to the postulate that the increased fluid clearance occurred not because of a change in the sieve properties of the epithelium. Lyso-PAF on the other hand did not show an effect on fluid clearance either. We can therefore postulate that the increase in fluid clearance caused by PAF is by a receptor mediated mechanism. Nonetheless, we cannot be certain whether this is primarily due to PAF, or secondarily due to a chain of events that have been initiated by PAF (3). One possible explanation arises from the fact that PAF has been shown to increase cytosolic calcium in a variety of cell lines (12, 14) including canine airway epithelial cells in primary culture (unpublished data, Man et al). As cytosolic  $\text{Ca}^{2+}$  is implicated in intracellular regulation of many absorptive or secretory processes, it is conceivable that this agent may enhance the absorptive function of the alveolar and airway epithelial cells. Alveolar protein clearance, on the other hand, may have proceeded via pinocytotic vesicles in alveolar type I cells and in capillary endothelial cells as demonstrated by Bensch et al. (2) and these vesicular transport processes may have been unaffected by PAF.

Recently it has been shown that solute-coupled fluid transport across the alveolar epithelium plays a significant role in the removal of liquid from the alveolar space (6). PAF in the airspaces appears to either supplement or enhance these active transport processes in some manner, but only transiently. The action of PAF

appears to be relatively short-lived as its effect was only observable from the NMR data within ~60 minutes of the introduction of serum plus PAF to the airspaces. This is not surprising as PAF has been reported to be metabolized rapidly by type II epithelial cells (14) and to have a transient effect in a variety of situations (5, 9, 12). More than 90 minutes after the instillation of serum, or serum plus PAF, the rates of alveolar fluid clearance determined from integrated NMR signal intensities were approximately equal and are therefore expected to have been driven by the same processes at this stage of the clearance.

The ability to decompose the transverse magnetization decay, for all cats with fluid instilled into their lungs, into two reproducible components, suggests that we were detecting NMR signal from at least two lung water compartments between which water exchange was slow with respect to  $T_2$ s. Shioya et al (28) also observed two transverse relaxation times for lung protons, *in-vivo*. In normal rat lungs they report  $T_2$  values of 9.5 msec (~90%) and 34 msec (~10%), where the percentages in parentheses denote the proportions of each component. By comparison, our overall four hour mean  $T_2$  values from serum instilled lungs are  $25 \text{ msec} \pm 1 \text{ msec}$  ( $n = 24$ ) ( $59\% \pm 2\%$ ) and  $177 \text{ msec} \pm 7 \text{ msec}$  ( $n = 24$ ) ( $41\% \pm 2\%$ ). Again the parenthetical percentages denote the proportions. Because the minimum inter-echo interval in our experiments was 26.3 msec, we were not able to resolve the faster of the two relaxation components observed by Shioya. It is likely, therefore, that the faster relaxing component resolved by us is actually a combination of the two components observed by Shioya in the normal lung. This component is then assumed to be due to tissue-bound fluid as in the cells and interstitial space of the lung. The more slowly relaxing component in our data, which does not correspond to either component observed by Shioya, could then be consistently interpreted as the instilled fluid residing in the airspaces.

Additional support for this interpretation was observed in a few isolated cases in which images showed that some of the instilled fluid remained in large airways. Fluid in the large airways was found to have  $T_2$  values ranging from 400 msec to 220 msec as compared with the instillate itself which had a  $T_2$  of approximately 480 msec. In contrast, for the fluid which was distributed over part of a lung lobe,  $T_2$  values ranged between 190 msec and 130 msec, as discussed previously. In all of these cases, the transverse relaxation in the lung also had a faster relaxing component with a  $T_2$  of approximately 25 msec. This elevation of the slow component transverse relaxation time for fluid in large airways is consistent with an expectation that relaxation rates ( $1/T_2$ ) be proportional to the tissue surface area in contact with the airspace fluid, an expectation which is in turn consistent with the work of Kveder et al. who report that  $T_1$  and  $T_2$  relaxation within the lung arises from a rapid exchange between bulk water and water protons which are tightly bound to biopolymer segments (15).

Although there is little or no signal obtained from the normal lung, as can be seen in figure 3a, within 15 minutes after fluid is instilled into the lung, ~60% of the signal corresponds to the relaxation component that we have attributed to tissue-bound fluid compartment. Equally surprising is the fact that the relative signal proportions corresponding to each of the two relaxation components changes very little during the observed fluid clearance, even with as much as 60% of the instilled fluid leaving the lung in some cases. To reconcile these data one would have to postulate that fluid is effectively being cleared from both the faster relaxing compartment (the cells and/or interstitium), and the more slowly relaxing compartment (the airspace fluid), by means of a flux of fluid from the airspaces into the interstitial space of the lung that is slow on a  $T_2$  time scale but fast relative to the

overall time course of these experiments. This postulate is supported by the observations of Gee and Staub (11) that perivascular fluid cuffs were formed within 10 minutes of fluid instillation into the airspaces of a dog lung. The photomicrographs in figures 2.6a and 2.6b also lend some support this hypothesis since it is clear that PAF has an affect not only the fluid clearance from the airspaces, but also on the content of the interstitial and vascular spaces of the lung as well.

## **2.5 Summary**

Results obtained from *in-vivo* NMR images, and nuclear relaxation time measurements, and confirmed gravimetrically and histologically from excised lungs, demonstrate the unique capabilities of NMR techniques for studying the lung fluid balance. In the *in-vivo* study, we were able to obtain both quantitative and qualitative results of alveolar fluid clearance. With PAF added to the instillate, clearance was markedly increased over a short 30 minute period, but was bi-phasic overall. Although the exact mechanism has not been defined, it appeared to be the result of a pharmacological action of PAF.

The resolution of transverse relaxation decay curves into two components has allowed us to speculate that tissue bound fluid and fluid in the airspaces are essentially separated on the short time scale of transverse relaxation. However, the constancy of the relative proportions of these two compartments over the 4 hour observation period and their independence of PAF, requires the additional hypothesis that exchange of airspace fluid does exist but only at a rate sufficient to equilibrate populations over periods of many minutes.

## **2.6 References**

- 1      Abragam A. *The Principles of Nuclear Magnetism*, (Oxford University Press, 1961).
  
- 2      Bensch K. G., E. A. M. Dominguez, Studies on the pulmonary air-tissue barrier. Part IV: cytochemical tracing of macromolecules during absorption. *Yale Journal of Biol. and Med.*, **43**, 236-241 (1971).
  
- 3      Bethel R. A., et al., Effect of PAF on parasympathetic contraction of canine airways. *J. Appl. Physiol.*, **66**(6), 2629-34 (1989).
  
- 4      Bevington P. R., *Data Reduction and Error Analysis for the Physical Sciences*, (McGraw Hill, New York, 1969).
  
- 5      Burhop K. E., et al., Platelet-activating factor increases lung vascular permeability to protein. *J. Appl. Physiol.*, **61**(6), 2210-2217 (1986).
  
- 6      Crone C., G. Saumon, G. Basset, News from the alveoli. *NIPS*, **5**, 50-53 (1990).
  
- 7      Cutillo A. G., et al., Determination of lung water content and distribution by nuclear magnetic resonance. *J. Appl. Physiol.: Respir. Environ. Exercise Physiol.* **57**(2): 583-588 (1984).
  
- 8      Cutillo A. G., et al., Assessment of lung water distribution by nuclear magnetic resonance. *Am. Rev. Respir. Dis.*, **137**: 1371-1378 (1988).

- 9 Evans T. W., K. F. Chung, D. F. Rogers, P. J. Barnes, Effect of platelet-activating factor on airway vascular permeability: possible mechanisms. *J. Appl. Physiol.*, **63**(2): 479-484 (1987).
- 10 Fullerton G. D., J. L. Potter, N. C. Dornbluth, NMR relaxation of protons in tissues and other macromolecular water solutions. *Mag. Res. Imaging*, **1**(4): 209-228 (1982).
- 11 Gee M. H., N. C. Staub, Role of bulk fluid flow in protein permeability of the dog lung alveolar membrane. *J. Appl. Physiol.: Respirat. Environ. Exercise Physiol.*, **42**(2): 144-149 (1977).
- 12 Kester M., P. Mene, G. R. Dubyak, M. J. Dunn, Elevation of cytosolic free calcium by platelet-activating factor in cultured rat mesangial cells. *FASEB J.*, **1**: 215-219 (1987).
- 13 Kumar R., D. J. Hanahan, Diversity of the Biochemical and Biological Behavior of Platelet Activating Factor, Chapter 9 of *Platelet Activating Factor and Related Lipid Mediators*. (edited by Fred Snyder, Plenum Press New York, 1987).
- 14 Kumar R., R. J. King, H. M. Martin, D. J. Hanahan, Metabolism of platelet activating factor (alkylacetylphosphocholine) by type-II epithelial cells and fibroblasts from rat lungs. *Biochim. Biophys. Acta* **917**: 33-41 (1987).
- 15 Kveder M., et al., Water proton NMR relaxation mechanisms in lung tissue. *Mag. Res. in Med.*, **7**: 432-441 (1988).

- 16 Ling C. R., M. A. Foster, Changes in NMR relaxation time associated with local inflammatory response. *Phys. Med. Biol.*, **27**(6): 853-860 (1982).
- 17 Matthay M. A., Y. Berthiaume, N. C. Staub, Long term clearance of liquid and protein from the lungs of unanesthetized sheep. *J. Appl. Physiol.*, **59**(3): 928-934 (1985).
- 18 Matthay M. A., Resolution of pulmonary edema - New insights. *West. J. Med.*, **154**: 315-321 (1991).
- 19 Meiboom S., D. Gill, Modified spin-echo method for measuring nuclear relaxation times. *Rev. Sci. Inst.*, **29**(8): 688-691 (1958).
- 20 Menon R. S., P. S. Allen, Solvent proton relaxation of aqueous solutions of the serum proteins  $\alpha_2$ -macroglobulin, fibrinogen, and albumin. *Biophysical Journal*, **57**: 389-396 (1990).
- 21 O'Flaherty J. T., R. L. Wykle, Metabolic Origin and Fate of Platelet-Activating Factor, *Agents and Actions Supplements Vol. 21: PAF, Platelets and Asthma*. (Birkhauser Verlag Basel, 1988).
- 22 Pearce M. L., J. Yamashita, J. Beazell, Measurement of pulmonary edema. *Circ. Res.*, **16**: 482-488 (1965).

- 23 Phillips D. M., P. S. Allen, S. F. P. Man, Assessment of temporal changes in pulmonary edema with NMR imaging. *J. Appl. Physiol.*, 66(3): 1197-1208 (1989).
- 24 Pinckard R. N., J. C. Ludwig, L. M. McManus, Chapter 10 of *Platelet-Activating Factors, Inflammation: Basic Principles and Clinical Correlates.*, (Raven Press Ltd., New York, 1988).
- 25 Schmidt H. C., D. G. Tsay, C. B. Higgins, Pulmonary edema: an MR study of permeability and hydrostatic types in animals. *Radiology*, 158: 297-302 (1986).
- 26 Selinger S. L. et al., Distribution volumes of [ $^{131}$ I]albumin, [ $^{14}$ C]sucrose, and  $^{36}$ Cl in sheep lung. *J. Appl. Physiol.*, 39(5): 773-779 (1975).
- 27 Shioya S., et al., Acute and repair stage characteristics of magnetic resonance relaxation times in oxygen-induced pulmonary edema. *Mag. Res. in Med.*, 8: 450-459 (1988).
- 28 Shioya S., R. Christman, D. C. Ailion, An *in vivo* imaging determination of multiexponential Hahn  $T_2$  of normal lung. *Mag. Res. in Med.*, 16: 49-56 (1990).
- 29 Skalina S., H. L. Kundel, G. Wolf, B. Marshall, The effect of pulmonary edema on proton nuclear magnetic resonance relaxation times. *Invest. Radiol.*, 19: 7-9 (1984).

30 Vargaftig B. B., Bronchopulmonary Pharmacology of PAF-acether, Chapter 15 of *Platelet Activating Factor and Related Lipid Mediators*. (Plenum Press New York, 1987).

### 3.0 In-vivo NMR Assessment of Bi-directional Alveolar Fluid Fluxes.<sup>1</sup>

#### 3.1 Introduction

The clearance of excess lung alveolar fluid and protein has been studied under a variety of conditions with a number of animal species and in every case fluid clearance has been shown to proceed more rapidly than protein clearance (5, 18, 24, 25). Moreover, alveolar fluid clearance has been shown to proceed against opposing oncotic pressure gradients which rise to greater than 50 cmH<sub>2</sub>O as proteins become concentrated in the alveolar space (17). Matthay et al. proposed that fluid may be cleared across the alveolar epithelium in opposition to a large pressure gradient by means of active cellular transport mechanisms (17). More recently, this proposal has been supported by the identification of several mechanisms of solute-coupled transport across the alveolar epithelium (3, 4, 6, 8, 19, 24). The presence of these active cellular transport mechanisms suggests that the alveolar epithelium may be much more active than was previously thought, and that there may be a certain amount of fluid transport in both directions across alveolar epithelial cells. As a result, the goal of this study was to determine if fluid transport in both directions across the alveolar epithelium could be detected *in-vivo* by means of nuclear magnetic resonance (NMR), and to obtain estimates of the relative flows in each direction.

---

<sup>1</sup> A version of this chapter is to be submitted for publication. P. W. Stroman, S. F. P. Man, P. S. Allen. In-vivo NMR Assessment of Bi-directional Alveolar Fluid Fluxes. Journal of Applied Physiology.

Excess alveolar fluid was modeled by instilling a 50% deuterated water based serum-like solution into one lung lobe of an anesthetized cat. Because there is a negligible amount of  $^2\text{H}$  occurring naturally in the body, this model provided us with a fluid tracer,  $^2\text{H}$ , only on the airspace side of the pulmonary air-blood barrier. In order to monitor the fluid and tracer clearances from the airspaces, we applied proton and deuteron NMR techniques consecutively and serially.  $\text{D}_2\text{O}$  has previously been used successfully as a tracer of  $\text{H}_2\text{O}$  movements (12). We have assumed that the clearance of instilled alveolar  $^2\text{H}$  reflects the time course of fluid absorption across the pulmonary air-blood barrier because  $\text{H}_2\text{O}$ ,  $\text{D}_2\text{O}$  and  $\text{HOD}$  are indistinguishable to the alveolar epithelium and because in liquid water, the motion of  $^1\text{H}$  and  $^2\text{H}$  is governed by the motion of intact water molecules and not by chemical exchange (27). The time course of the changes of the alveolar  $^1\text{H}$  content is influenced both by the absorption of  $\text{HOD}$  from the airspaces and by the secretion of  $\text{H}_2\text{O}$  into the airspaces, whereas the clearance of the tracer,  $^2\text{H}$ , reflects only the rate of  $\text{HOD}$  absorption from the airspaces. Thus, the combination of these two NMR techniques enabled us to quantify the rates of fluid absorption and secretion across the pulmonary air-blood barrier.

Because we have demonstrated previously that the net alveolar fluid clearance in cats can be enhanced by the inclusion of PAF in the instillate (25), we also chose to assess in this study the separate effects of this agent on airspace fluid absorption and secretion. Platelet-activating factor (PAF) is a family of ether-lipids whose active component is 1-O-Hexadecyl/octadecyl-2-acetyl-*sn*-glycero-3-phosphocholine (22). PAFs are produced by a wide variety of cells in the body including alveolar type II epithelial cells (13, 14, 21, 22). Moreover, these molecules may have physiological and/or pathological significance, as it has been

shown that the pulmonary response to intra-airway PAF mimics asthma, and PAF has been detected in the lungs of humans with sarcoidosis (2, 23).

## **3.2 Methods**

### **3.2.1 Animal Model of Alveolar Fluid Clearance**

Adult mongrel cats (3.0 - 5.0 kg) were studied after being anesthetized with an intramuscular injection of ketamine (Ketalean 25 mg/kg), xylazine hydrochloride (Rompun 0.5 mg/kg) and acepromazine (Atravet 1 drop/4 kg), and anesthesia was maintained at ~25% of the initial dose/hour. Throughout the study cats were in a supine position, intubated, and were ventilated with room air at 15 breaths/minute, a tidal volume of 10 ml/kg, and 2 cmH<sub>2</sub>O of positive end-expiratory pressure (PEEP). Arterial blood gas tensions were monitored to assure adequate ventilation was being maintained.

The instillate was prepared as a phosphate buffered physiological saline solution (PSS) which included 5.5 mM D-glucose and equal volumes of H<sub>2</sub>O and D<sub>2</sub>O. After preparation this solution was filtered through a 0.22 µm Millipore® filter to remove any possible bacterial contaminants. Just prior to instillation into the airspaces, 5 g/dL bovine serum albumin was added to 5 ml of PSS to make a serum-like solution (SLS). Also prior to instillation, 1 mg of Evan's Blue dye was added to mark the location of the instillate in the lung, and 3 µCi of <sup>125</sup>I-albumin was added to label the instilled albumin. The resulting SLS was instilled at a dose of 0.7 ml/kg into a localized region of one lower lung lobe, via a polyethylene catheter (PE-90). For studies which included PAF, 250 µl of 10<sup>-5</sup> M PAF was

also added to the SLS immediately prior to instillation; a dose range of 0.17 to 0.19  $\mu\text{g}$  PAF/kg body weight was used (mean = 0.18  $\mu\text{g}$  PAF/kg).

Prior to fluid instillation, mechanical ventilation was interrupted and a PE-90 catheter was inserted into a lower lung lobe (left lung, 7 times out of 10 experiments). The SLS was then injected with a syringe over 15 sec, followed by the insufflation of several ml of room air. Mechanical ventilation was resumed immediately after fluid instillation. The precise amount of fluid instilled was determined by weighing the syringe and catheter assembly before and after instillation. NMR imaging and/or gravimetric analysis of the lung were then carried out, as described below, during the succeeding four hour period.

At the end of the 4 hour observation period, the cat was euthanized and the lungs were removed. The distribution of the instilled fluid in the experimental lobe was identified by the Evan's Blue dye. The lung lobes were processed for gravimetric measurements of the excess fluid, and for gamma counting to determine the amount of instilled  $^{125}\text{I}$ -albumin remaining in the fluid-instilled lobe, as in our previous study. For the present study, however, the excess alveolar fluid contained both  $\text{H}_2\text{O}$  and  $\text{D}_2\text{O}$ .

A total of 5 cats were studied after instillation of SLS with PAF into a lower lung lobe, and another 5 were studied without PAF. Gravimetric measurements were obtained for all cats but the changes in the  $^1\text{H}$  and  $^2\text{H}$  contents of the instilled fluid were monitored in the lungs of only 4 cats in each of these two groups.

### 3.2.2 $^1\text{H}$ and $^2\text{H}$ NMR Methods

NMR measurements were carried out on a modified Bruker CXP Spectrometer (Bruker Instruments Inc., Billerica MA) with a 40 cm bore magnet at a static field of 2.35 T. Proton data were acquired using a surface coil attached to the plexiglass tray which supported the cat in a supine position, and curved around the cat's back to provide maximum sensitivity to the lower lung lobes. A typical repetition interval for proton NMR was 1 second. A second smaller surface coil (6 turns, 8 cm diameter) attached to the same tray, was employed for both transmission and reception at the deuteron resonant frequency (15.4 MHz). To overcome the rapid deuteron transverse relaxation in the lung ( $T_2^* \sim 3$  msec), the deuteron NMR signal was acquired in the form of FIDs and the peak signal amplitude was sampled only 30  $\mu\text{s}$  after the RF excitation pulse was transmitted. As a result, the  $^2\text{H}$  NMR signal intensity was not unduly influenced by the rapid deuteron transverse magnetization decay in the lung.

Measurements of the total  $^2\text{H}$  NMR signal intensity, without spatial resolution, were made with a technique similar to that used by Kim et al. (12). The total signal intensity was measured from 1000 acquisitions with a repetition interval of 100 msec. Our assumption that the  $^2\text{H}$  NMR intensity could be used to predict the quantity of  $^2\text{H}$  within our region of interest was repeatedly verified by a correlation ( $r \geq 0.993$ ) between intensity measurements and  $^2\text{H}$  concentrations of seven 100 ml phantoms ranging from 1.0% to 0.05% deuteration.

Because the receiver sensitivity was spatially non-uniform, a change of the instillate location in the lung, relative to the receiver coil, could have a considerable effect on the detected signal intensity. It was therefore necessary to check by

imaging that the fluid had not dispersed during clearance. After fluid instillation, the deuterium signal intensity measurements were each followed by a deuterium image and a proton image, and the sequence repeated throughout the 4 hour observation period.<sup>2</sup>

Deuterium NMR images were obtained by applying a reconstruction from projections technique to eight  $^2\text{H}$  signal projections from a transverse slice. Slice definition was provided by the spatial distribution in receiver sensitivity, a method which maximized the deuterium signal contribution to the image. The projections were generated at equal angular separations between  $0^\circ$  and  $180^\circ$ , from the corresponding FID. Employing a repetition time of 100 msec, 512 averages were used for each projection. The image was reconstructed by means of a back-projection algorithm (15, 16).

Transverse proton NMR images of a 1 cm thick slice of the cat's thorax were obtained using a Carr-Purcell-Meiboom-Gill (CPMG) spin-echo pulse sequence having an inter-echo interval of 18.1 msec and data acquisition gated to the cat's breathing as described in our previous study (25). Control images of several slices covering the caudal half of the cat's thorax were obtained prior to fluid instillation. After instillation, the region of the cat's thorax containing the instilled fluid was imaged alternately with  $^2\text{H}$  measurements over a 4 hour period. The 4 hour time course of changes in the  $^1\text{H}$  content of the fluid-instilled lung lobe was

---

<sup>2</sup> Further details of the deuterium NMR techniques employed for this study are included in Appendix 3.1 of this thesis.

determined by integrating first-echo image pixel intensities over the lung region of interest.<sup>3</sup>

### **3.3 Results**

An example of a deuteron image (Figure 3.1a) superimposed on the corresponding transverse proton image (Figure 3.1b) obtained after instilling fluid into a left lower lung lobe is shown in Figure 3.1c. The time dependence of the integrated  $^1\text{H}$  signal intensity data,  $I_{\text{H}}(t)$ , and that of the integrated  $^2\text{H}$  signal intensity data,  $I_{\text{D}}(t)$ , both averaged over 4 cats and with data grouped into 40 minute intervals, are shown in Figure 3.2 for the case in which the instillate was SLS. Figure 3.3 shows the corresponding data for an instillate of SLS plus PAF. The values of  $I_{\text{H}}(t)$  and  $I_{\text{D}}(t)$  are expressed relative to the extrapolated intensities immediately after instillation,  $I_{\text{H}}(0)$  and  $I_{\text{D}}(0)$ .

---

<sup>3</sup> Transverse relaxation time measurements were also obtained for the same lung region of interest. These relaxation time measurements supplement those discussed in Chapter 2 of this thesis but do not contribute to the current discussion of bi-directional fluid movements, and so are discussed in Appendix 3.2 of this thesis.

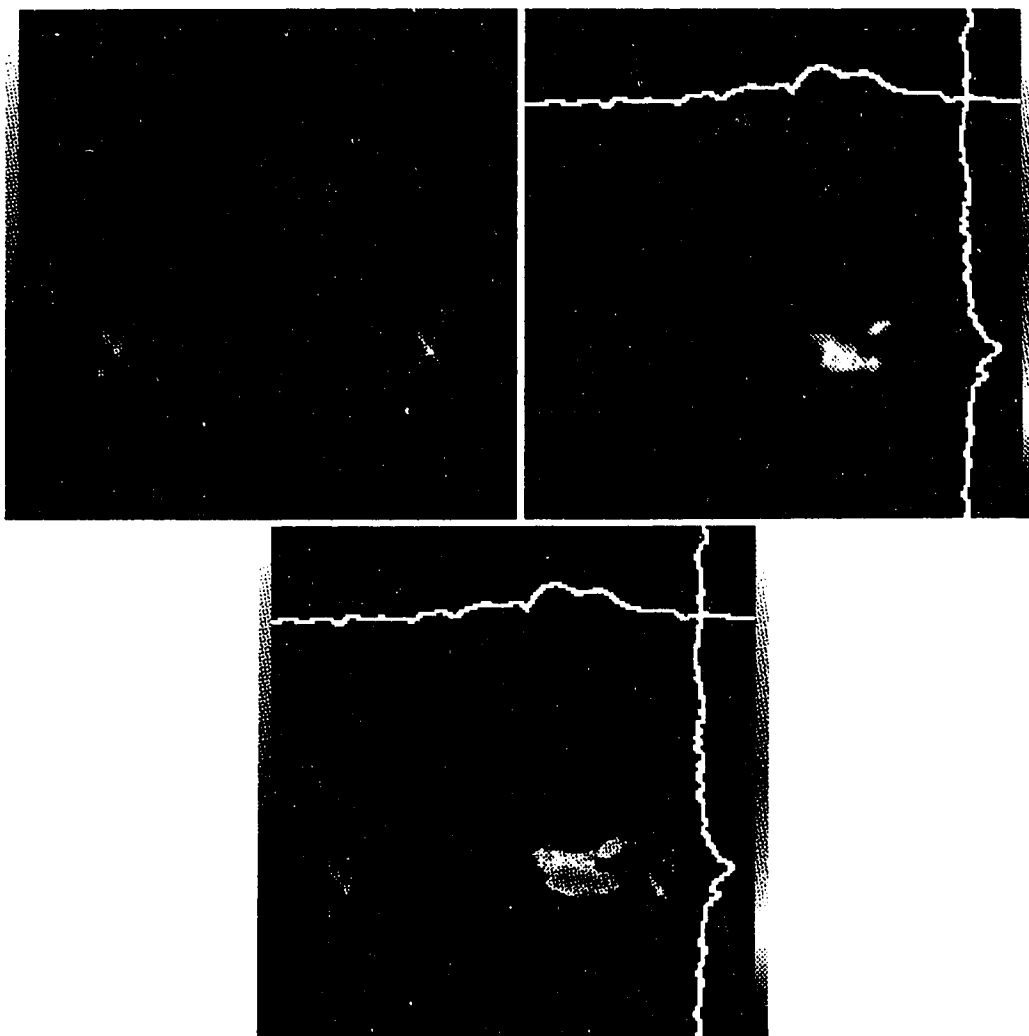
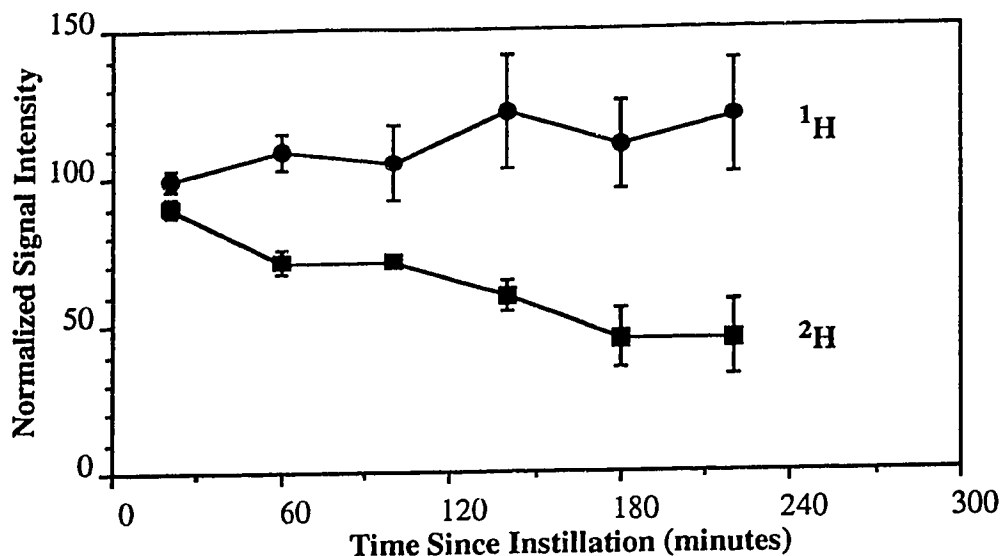


Figure 3.1 a) A  $^1\text{H}$  NMR image of a 1 cm thick transverse slice of a cat's thorax, 30 minutes after the instillation of SLS into the left lower lung lobe (upper left). b) The corresponding  $^2\text{H}$  NMR image of the instilled fluid in the cat's left lower lung lobe, as well as two of the projection profiles used to construct the image, acquired 20 minutes after fluid instillation (upper right). c) The same  $^1\text{H}$  and  $^2\text{H}$  NMR images overlaid for a spatial comparison (bottom).



**Figure 3.2** The averaged ( $n = 4$ ) time course of the  $\text{H}_2\text{O}$  content (black circles) and of the  $\text{D}_2\text{O}$  content (black squares) of a lower lung lobe after instillation of SLS. The data points correspond to averages over a 40 minute data acquisition period centered at the time of the data point. The error bars indicate the standard error of the mean.

Neither  $^2\text{H}$  nor  $^1\text{H}$  NMR images demonstrated any change in the location of the instilled alveolar fluid over the time course of an experiment, either toward or away from the receiver coil, and so the sensitivity of the receiver to the fluid tracer was assumed to remain constant during an experiment. Because the original instillate contained equal amounts of  $^1\text{H}$  and  $^2\text{H}$ , we are able to compute a net fluid clearance time course,  $I_{\text{Net}}(t)$ , from equation 3.1 using both sets of NMR data

$$(3.1) \quad I_{\text{Net}}(t) = \frac{1}{2} \left[ \frac{I_{\text{H}}(t)}{I_{\text{H}}(0)} + \frac{I_{\text{D}}(t)}{I_{\text{D}}(0)} \right]$$

$I_{\text{Net}}$ , which can be compared with the corresponding gravimetric results, is illustrated in Figures 3.4 and 3.5 for either SLS or SLS plus PAF, respectively.

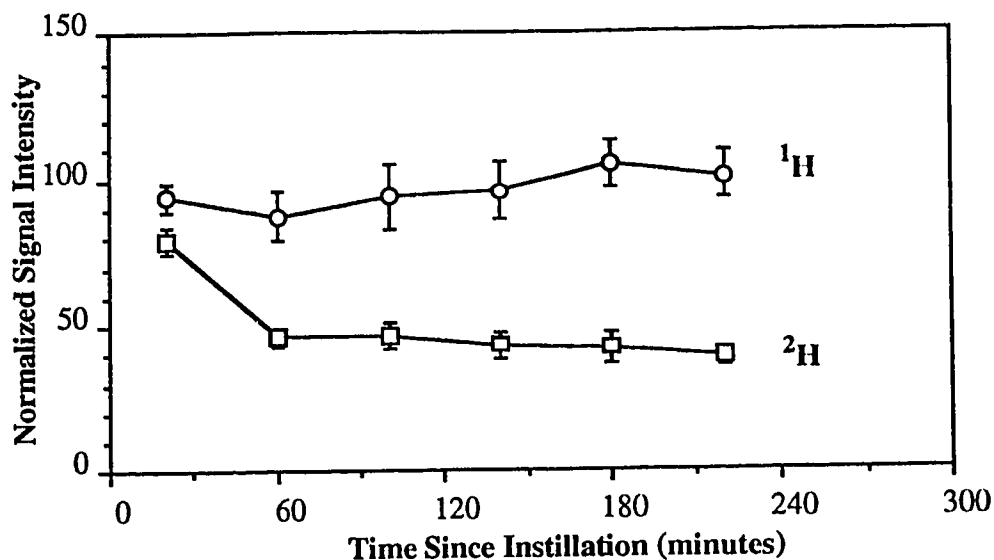


**Figure 3.3** The averaged ( $n = 4$ ) time course of the  $^1\text{H}$  content (white circles) and of the  $^2\text{H}$  content (white squares) of a lower lung lobe after instillation of SLS plus PAF. The data points correspond to averages over a 40 minute data acquisition period centered at the time of the data point. The error bars indicate the standard error of the mean.

For the SLS instillate,  $^1\text{H}$  NMR intensity data showed that the proton component of lung water increased to  $121\% \pm 19\%$  ( $n=4$ ) of its starting value in the experimental lung lobe over a period of 3.3 to 4 hours after instillation, whereas the  $^2\text{H}$  NMR intensity data showed a decrease in the deuterated component to  $45\% \pm 13\%$  ( $n=4$ ) of its starting value over the same time period (Figure 3.2). The total amount of fluid remaining in the experimental lung lobe, averaged over the final data acquisition period and computed by combining the  $^1\text{H}$  and  $^2\text{H}$  intensity data, is  $83\% \pm 16\%$  ( $n = 4$ ). This just agrees within the range of experimental uncertainty with the corresponding gravimetric measurement of  $56\% \pm 13\%$  ( $n = 5$ ) taken at 4 hours after instillation (Figure 3.4). All of the results are expressed as the mean of  $n$  experiments, plus or minus the standard error of the mean.

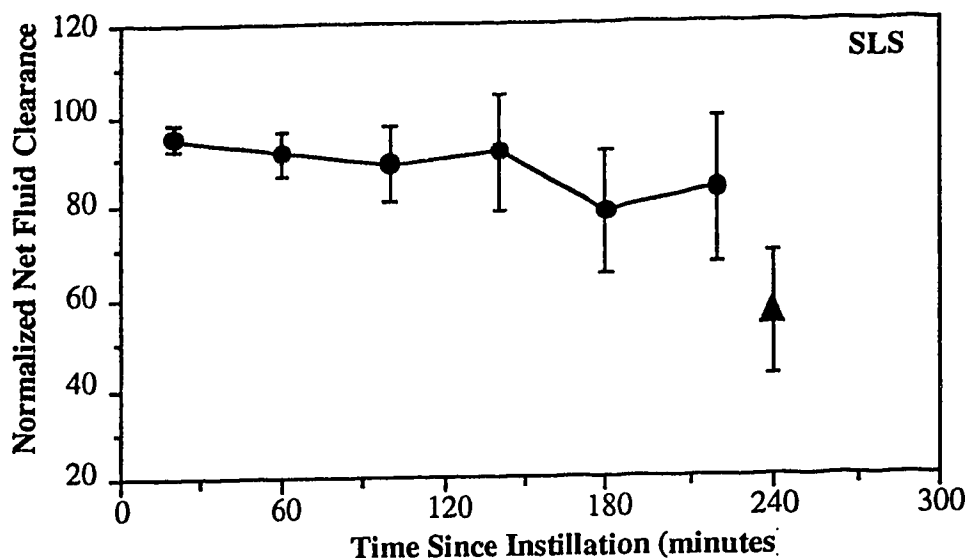


**Figure 3.4** The net clearance time course of instilled alveolar SLS, computed from *in-vivo* NMR measurements (black circles) and the corresponding gravimetric measurement (black triangle), with error bars indicating the standard error of the mean. The NMR measurements are averages over 40 minute data acquisition periods and over 4 cats. The gravimetric measurement is an average over 5 cats sacrificed at 4 hours post instillation.

With PAF added to the SLS, the  $^1\text{H}$  NMR intensity data showed no increase in the protonated component remaining in the experimental lung lobe between 3.3 and 4 hours after instillation, but an essentially constant value of  $101\% \pm 8\%$  ( $n=4$ ) (Figure 3.3). The  $^2\text{H}$  NMR intensity data however, showed a greater decrease in the deuterated component than without PAF, since only  $39\% \pm 3\%$  ( $n=4$ ) could be detected in the experimental lung lobe between 3.3 and 4 hours after instillation. Together these data indicate that the total averaged amount of instilled alveolar SLS plus PAF remaining in the lung lobe over the final data acquisition period was  $70\% \pm 6\%$  ( $n = 4$ ) of the amount initially instilled. Again the NMR data

point just overlaps within the limits of error with the corresponding gravimetric measurement of  $49\% \pm 15\%$  ( $n = 5$ ) (Figure 3.5).

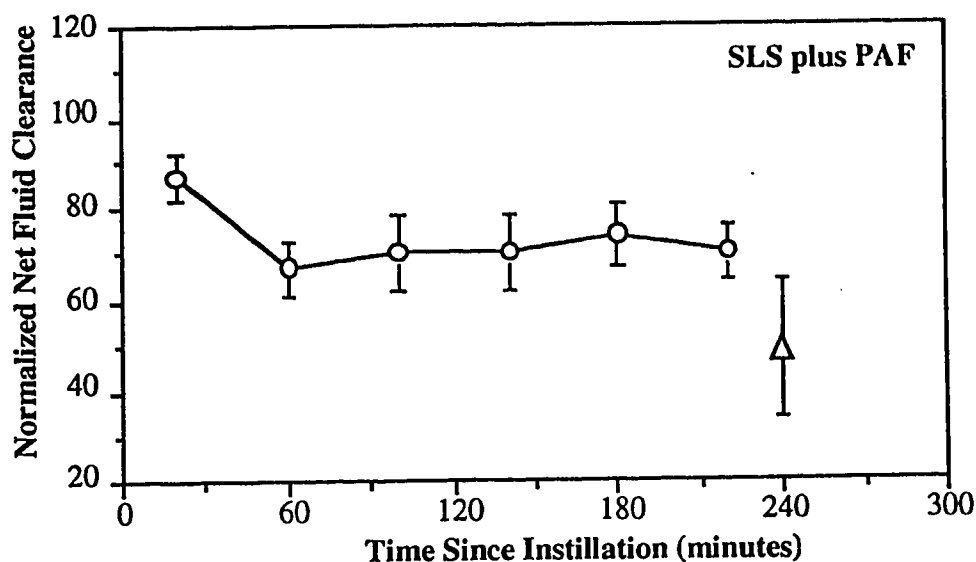


**Figure 3.5** The time course of the net clearance of instilled alveolar SLS plus PAF, computed from *in-vivo* NMR measurements (white circles) and the corresponding gravimetric measurement (white triangle), with error bars indicating the standard error of the mean. The NMR measurements are averages over 40 minute data acquisition periods and over 4 cats. The gravimetric measurement is an average over 5 cats sacrificed at 4 hours post instillation.

The proportions of  $^{125}\text{I}$ -albumin remaining in the lung 4 hours after instillation of either SLS or SLS plus PAF were  $82\% \pm 6\%$  ( $n = 5$ ) and  $86\% \pm 8\%$  ( $n = 5$ ), respectively, showing a marked consistency within the limits of their errors.

### 3.4 Discussion

The net clearance of instilled alveolar fluid is the result of considerable fluid transport in both directions across the stationary air-blood barrier, with the rate of fluid absorption exceeding that of secretion. Serially alternated *in-vivo* proton and deuteron intensity measurements of the clearance of a partially deuterated instillate from cat lung show a distinct difference between the proton and deuteron clearance rates. The protonated component clears more slowly (presumably due to H<sub>2</sub>O secretion into the airspaces) thus supporting the premise that bi-directional fluid movement across the air-blood barrier can be detected using a combined <sup>1</sup>H/<sup>2</sup>H monitoring technique. More conclusive support for this premise can be found in the agreement of (see Fig 3.6) the combined proton and deuteron clearance of the present study with the net clearance of H<sub>2</sub>O observed previously for a fully protonated autologous serum instillate (25). Matthay et al. (17) similarly found that the clearance of instilled Ringer's lactate with 5% albumin was identical to that of autologous serum. Accepting the premise, the individual rates of absorption and secretion can be obtained from the time course of the deuteron and proton signals. For example, for an instillate that is 50% deuterated, the time dependence of absorption, A(t), and secretion, S(t), expressed as a percentage of the original instillate, are<sup>4</sup>

$$(3.2) \quad A(t) = \left[ 1 - \frac{I_D(t)}{I_D(0)} \right] * 100$$

$$(3.3) \quad S(t) = \frac{1}{2} \left[ \frac{I_H(t)}{I_H(0)} - \frac{I_D(t)}{I_D(0)} \right] * 100$$

---

<sup>4</sup> The derivation of equations 3.2 and 3.3 is provided in Appendix 3.3 of this thesis.

and they are illustrated in Figures 3.7 and 3.8 respectively.

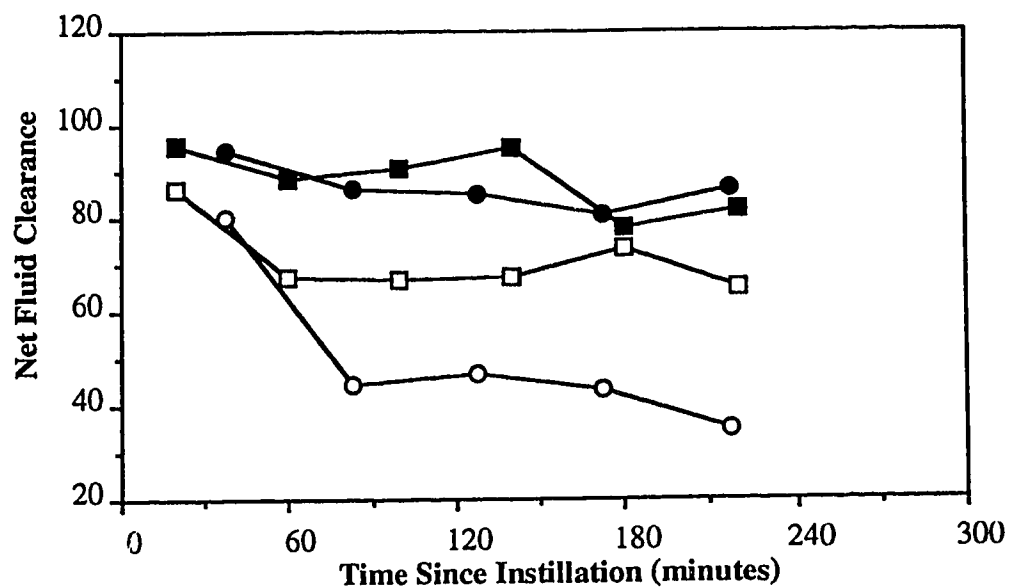


**Figure 3.6** A comparison of the time course of the net clearance from the present experiments and from the previous work (25) on net  $^1\text{H}$  clearance. Squares are used to indicate values computed from equation 3.1 from the present combined  $^1\text{H}$  and  $^2\text{H}$  intensity measurements, whereas the circles represent previous results of  $^1\text{H}$  intensity measurements (25). The instillates are represented as follows, SLS (black squares), serum (black circles), SLS plus PAF (white squares), and serum plus PAF (white circles).

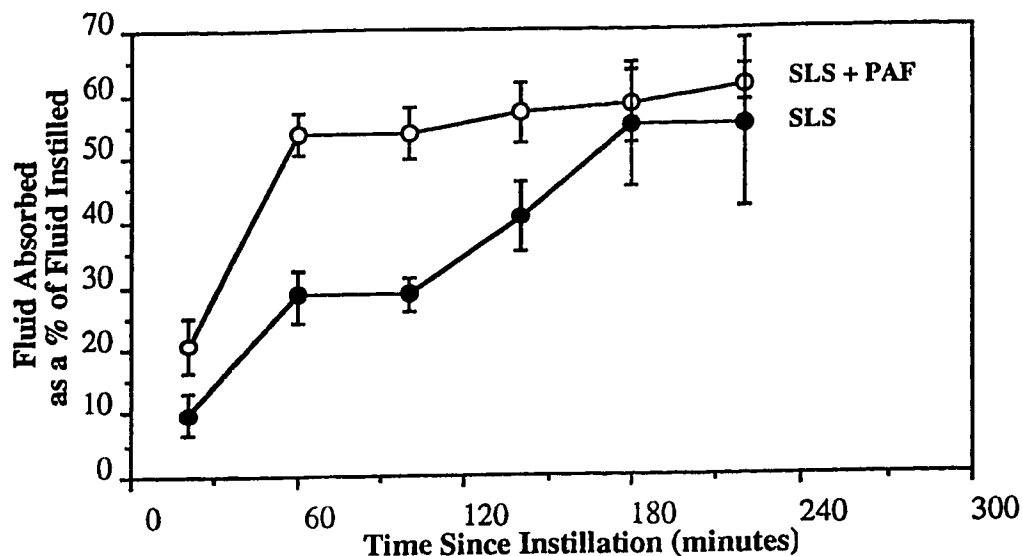


**Figure 3.7** An illustration of the time course of the amount of fluid absorbed from the lung, relative to the amount instilled, calculated from equation 3.2. Absorption of SLS (black circles) and of SLS plus PAF (white circles) are shown.

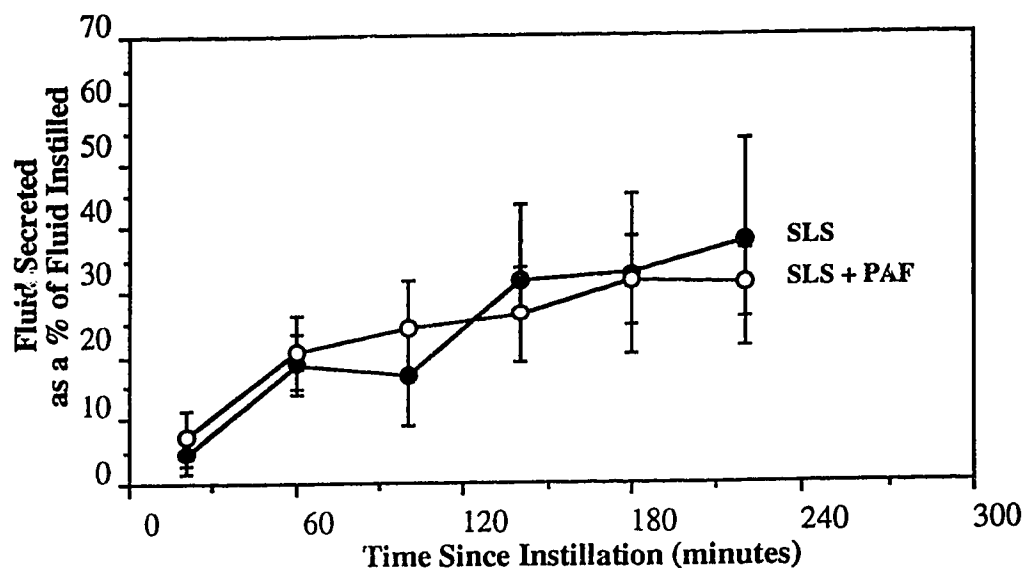


**Figure 3.8** An illustration of the time course of the amount of fluid secreted into the lung, relative to the amount instilled, calculated from equation 3.3. Fluid secretion after the instillation of SLS (black circles), and after the instillation of SLS plus PAF (white circles), are shown.

Figures 3.6, 3.7 and 3.8, indicate that over the 4 hour time period in which ~20% of instilled SLS is cleared from the lung, ~55% of the instilled fluid volume is absorbed from the airspaces, while a volume approaching 35% of that instilled is secreted back into the airspaces. This result illustrates a considerable amount of fluid moving in both directions across the air-blood barrier of the lung during the net clearance of instilled alveolar fluid. It is consistent with a model in which the net clearance is primarily the result of solute-coupled ion transport, with passive fluid movements being of secondary importance, as has been suggested by Matthay and by Basset et al. (4, 19). The efficacy of the solute-coupled  $\text{Na}^+$  transport across the alveolar epithelium has also been clearly demonstrated by Berthiaume et al. and by Smedira et al. (6, 24). Consequently, although there may be a certain amount of passive fluid movement via paracellular pathways contributing to the observed fluid secretion into the airspaces (17), the impermeable nature of the alveolar epithelium, the existence of a  $\text{Na}^+$ -  $\text{K}^+$  pump on the basolateral side of type II epithelial cells (4), and the demonstrated  $\text{Cl}^-$  secretion by tracheal epithelial cells (26), lead us to postulate that the primary source of secreted alveolar fluid is also solute-coupled transport.

The effects of PAF on the rates of net fluid clearance, and fluid absorption and secretion across the pulmonary air-blood barrier, are also illustrated by Figures 3.6, 3.7 and 3.8. For example, during the first hour after fluid instillation, approximately 25% of instilled SLS is absorbed from the airspaces, whereas with PAF added to the SLS, the amount absorbed is increased to approximately 55% of that instilled. The net clearance is increased from ~10% to ~30% by the presence of PAF, and over the whole 4 hour period, an analysis of variance (ANOVA) shows that the whole time course for SLS clearance differs significantly from that of SLS

plus PAF at the 95% confidence level. This enhancement of the net clearance by the presence of PAF in the instillate was also found previously (25) for autologous serum instillates. However, the enhancement was more marked in the case of autologous serum, probably due to the additional components in blood serum (7, 10)

The more detailed look at the clearance, which is afforded only by the combined  $^1\text{H}/^2\text{H}$  technique, enables the effect of PAF on the components of the bi-directional flow to be observed. Figures 3.7 and 3.8 show that while PAF enhances clearance, it apparently has little effect upon secretion. One possible mechanism of PAF action is suggested by the fact that this agent has been shown to increase cytosolic calcium in a variety of cell lines (1, 11, 14, 20) including canine airway epithelial cells in primary culture (Man et al, unpublished data). Because cytosolic  $\text{Ca}^{2+}$  is implicated in intracellular regulation of many absorptive or secretory processes, it is conceivable that this agent may enhance the absorptive function of the alveolar and airway epithelial cells. An alternative possibility for the mechanism of PAF action is suggested by the fact that PAF has been shown to increase intracellular cAMP (cyclic 3',5'-adenosine monophosphate) in human lymphocytes (28). Agents which act to increase intracellular cAMP have been shown to result in increased ion transport across primary cultured monolayers of alveolar type II epithelial cells (9). Moreover, Berthiaume has demonstrated that increasing lung tissue cAMP levels *in-vivo* results in an increased lung fluid clearance (6). Thus, a plausible explanation of the observed PAF-enhanced alveolar fluid absorption will be provided if the action of PAF can be shown to increase intracellular cAMP levels in pulmonary epithelial cells as well.

The ( $8\% \pm 6\%$ ) clearance of protein from the alveolar space over a 4 hour period was indicative of a much slower clearance rate than that of the alveolar fluid itself. Moreover, protein clearance was apparently unaffected by PAF. Both of these findings are in agreement with the results of our previous study on the net clearance of autologous serum (25) showing that neither SLS nor SLS plus PAF results in a change in the sieve properties of the epithelium when it is introduced into the airspaces of the lung.

### **3.5 Summary**

By means of a combination of  $^1\text{H}$  and  $^2\text{H}$  NMR techniques we have been able to quantify fluid movements in opposite directions across the pulmonary air-blood barrier, in a living animal. To our knowledge this is the first such observation. This bi-directional movement of fluid is thought to be primarily the result of solute-coupled ion transport, with passive fluid movements being of secondary importance. Furthermore, by obtaining independent measures of absorption and secretion, we have been able to show that the means by which PAF enhances alveolar fluid clearance in the first hour after fluid instillation is by increasing the rate of fluid absorption, while having no apparent effect on the rate of fluid secretion.

### 3.6 References

- 1 Avdonin P. V. et al., Evidence for the receptor-operated calcium channels in human platelet plasma membrane. *Thrombosis Research*, **46**: 29-37 (1987).
- 2 Barnes P. S. and K. F. Chung, PAF closely mimics pathology of asthma. *TIPS*, **8**: 285 (1987).
- 3 Basset G., C. Crone, G. Saumon, Significance of active ion transport in transalveolar water absorption: a study on isolated rat lung. *J. Physiol.*, **384**: 311-324 (1987).
- 4 Basset G., C. Crone, G. Saumon, Fluid absorption by rat lung *in-situ*: pathways for sodium entry in the luminal membrane of alveolar epithelium. *J. Physiol.*, **384**: 325-345 (1987).
- 5 Berthiaume Y., V. C. Broaddus, M. A. Gropper, T. Tanita, M. A. Matthay, Alveolar liquid and protein clearance from normal dog lungs. *J. Appl. Physiol.*, **65**(2): 585-593 (1988).
- 6 Berthiaume Y., Effect of exogenous cAMP and aminophylline on alveolar and lung fluid clearance in anesthetized sheep. *J. Appl. Physiol.*, **70**(6): 2490-2497 (1991).
- 7 Bolin R. W., T. R. Martin, R. K. Albert, Lung endothelial and epithelial permeability after platelet-activating factor. *J. Appl. Physiol.*, **63**(5): 1770-1775 (1987).

- 8 Crone C., G. Saumon, G. Basset, News from the alveoli. *NIPS*, 5: 50-53 (1990).
- 9 Goodman B. E., S. E. S. Brown, E. D. Crandall, Regulation of transport across pulmonary alveolar epithelial cell monolayers. *J. Appl. Physiol.: Respirat Environ. Exercise Physiol.*, 57(3): 703-710 (1984).
- 10 Henson P. M., PAF - a perspective. *Am. J. Cell. Mol. Biol.*, 1: 263-265 (1989).
- 11 Kester M., P. Mene, G. R. Dubyak, M. J. Dunn, Elevation of cytosolic free calcium by platelet-activating factor in cultured rat mesangial cells. *FASEB J.* 1: 215-219 (1987).
- 12 Kim S. G. and J. J. H. Ackerman, Multicompartment analysis of blood flow in tissue perfusion employing D<sub>2</sub>O as a freely diffusible tracer: a novel deuterium NMR technique demonstrated via application with Murine RIF-1 tumors. *Mag. Res. Med.*, 8: 410-426 (1988).
- 13 Kumar R., D. J. Hanahan, Diversity of the Biochemical and Biological Behavior of Platelet Activating Factor, Chapter 9 of *Platelet Activating Factor and Related Lipid Mediators*. edited by Fred Snyder, (Plenum Press New York, 1987).
- 14 Kumar R., R. J. King, H. M. Martin, D. J. Hanahan, Metabolism of platelet activating factor (alkylacetylphosphocholine) by type-II epithelial cells and fibroblasts from rat lungs. *Biochim. Biophys. Acta* 917: 33-41 (1987).

- 15 Link J. and J. Seelig, Comparison of deuterium NMR imaging methods and application to plants. *J. Mag. Res.*, **89**: 310-330 (1990).
- 16 Mansfield P., and P. G. Morris, *NMR Imaging in Biomedicine* (Academic Press, New York, 1982).
- 17 Matthay M. A., C. C. Landolt, N. C. Staub, Differential liquid and protein clearance from the alveoli of anesthetized sheep. *J. Appl. Physiol.: Respirat. Environ. Exercise Physiol.*, **53**(1): 96-104 (1982).
- 18 Matthay M. A., Y. Berthiaume, N. C. Staub, Long-term clearance of liquid and protein from the lungs of unanesthetized sheep. *J. Appl. Physiol.*, **59**(3): 928-934 (1985).
- 19 Matthay M. A., Resolution of pulmonary edema - New insights. *West J Med*, **154**: 315-321 (1991).
- 20 Michel L., et al., Biosynthesis of PAF-acether factor-acether by human skin fibroblasts *in vitro*. *J. Immunol.*, **141**: 948-953 (1988).
- 21 O'Flaherty J. T., R. L. Wykle, Metabolic Origin and Fate of Platelet-Activating Factor. *Agents and Actions Supplements Vol. 21: PAF, Platelets and Asthma*. (Birkhauser Verlag Basel, 1988).

- 22 Pinckard R. N., J. C. Ludwig, L. M. McManus, Chapter 10 of *Platelet-Activating Factors, Inflammation: Basic Principles and Clinical Correlates*. (Raven Press Ltd., New York, 1988).
- 23 Scappaticci E., et al., Platelet-activating factor in bronchoalveolar lavage from patients with sarcoidosis. *Am. Rev. Resp. Dis.*, **146**: 433-438 (1992).
- 24 Smedira N., et al., Alveolar and lung liquid clearance in anesthetized rabbits. *J. Appl. Physiol.*, **70**(4): 1827-1835 (1991).
- 25 Stroman P. W., et al., Evaluation of the effects of PAF on alveolar fluid clearance using NMR imaging. *J. Appl. Physiol.* (accepted).
- 26 Tamaoki J., et al., Angiotensin II-1 receptor-mediated Cl secretion by canine tracheal epithelium. *Am. Rev. Resp. Dis.*, **146**: 1187-1191 (1992).
- 27 Vinogradov S. N. and R. H. Linnel, *Hydrogen Bonding* (Van Nostrand Reinhold Company, New York, 1972).
- 28 Wang S. and R. G. Townley, Effects of platelet activating factor on cyclic AMP accumulation in human lymphocytes. *Annals of Allergy*, **6**: 140-142 (1992).

#### **4.0 General Discussion and Veracity of the Conclusions**

Light microscopy of the lung tissue 4 hours after the instillation of either serum or serum plus PAF showed no evidence of inflammation, and that the alveolar epithelium and capillary endothelium were apparently intact at that time. We can postulate that PAF did not cause a change in the sieve properties of the epithelium because the clearance of albumin from the alveolar space was observed to be ~3%/hour irrespective of whether the instillate was serum, serum plus PAF, SLS, or SLS plus PAF. Moreover, we can be fairly certain that the cat's overall pulmonary function was being maintained at a normal level, and was not disrupted by the instillation of a localized bolus of fluid, because blood gas tensions remained relatively stable in these anesthetized, spontaneously breathing cats. Our observations indicate that fluid clearances, both with and without PAF, were from relatively normal, intact lung lobes and may thus have direct physiological relevance.

#### **4.1 NMR and Gravimetric Measurements of Clearance Rates**

The NMR studies discussed in Chapters 2 and 3 have demonstrated that non-invasively, in a living animal, we are able to monitor the net clearance of instilled alveolar fluid, and to quantify the absorption and secretion components of this net clearance. The net clearance (17%/4 hours) of a serum (or serum-like) solution was observed to proceed more rapidly than that of albumin (8%/4 hours), and was the result of fluid absorption and secretion at 55%/4 hours and 38%/4 hours, respectively. These results are consistent with a model in which the net clearance of alveolar fluid is primarily the result of solute-coupled ion transport,

with passive fluid movements being of secondary importance, as was initially proposed by Matthay (11).

After instilling 3.1 ml of SLS into a 3 kg cat, the computed rates of absorption and secretion were approximately 80 nl/sec and 55 nl/sec, respectively. The action of PAF was observed to increase the SLS absorption rate to approximately 315 nl/sec, but only over the first hour after instillation, and had no discernible effect on the fluid secretion rate (see Chapter 3). In combination with an autologous serum instillate the action of PAF was even more pronounced than with SLS, as demonstrated by the experimentally observed clearance rates of 65%/4 hours, and 30%/4 hours, respectively (see Chapter 2). In a 3 kg cat, these net clearances are equivalent to average 4 hour clearance rates of 95 nl/sec and 44 nl/sec, respectively. We have proposed that PAF may act by increasing the cytosolic  $\text{Ca}^{2+}$  in pulmonary epithelial cells to enhance the absorptive function of the epithelium, or by increasing the levels of intracellular cAMP, thereby stimulating epithelial ion transport. Regardless of the mechanism of PAF action however, the observed clearance time courses of serum plus PAF, and of SLS plus PAF, indicate that there are one or more components of serum, not included in the SLS preparation, that act to enhance the effect of PAF on alveolar fluid clearance.

#### **4.2 Transverse Relaxation Time Measurements of Water Protons**

The transverse relaxation time measurements discussed in Chapter 2 and Appendix 3.2 have consistently demonstrated that we are detecting signal from two lung water compartments, between which, fluid exchange is slow with respect to the measured transverse relaxation times. In Chapter 2 we have proposed that the two relaxation components, which are identified by the relaxation times  $T_{2F}$

and  $T_{2S}$  (faster relaxing and slower relaxing, respectively), are associated with tissue-bound fluid in the interstitial and intracellular spaces, and with airspace fluid, respectively. The measured values of  $T_{2F}$  were consistently in the range of 25 msec to 32 msec and demonstrated no systematic variations over 4 hours of fluid clearance from the lung. Similarly, measured values of  $T_{2S}$  did not demonstrate conclusive systematic variation over 4 hours of fluid clearance, but the 4 hour mean values of  $T_{2S}$  varied considerably with the fluid instilled (serum-based or SLS-based) and with the mode of ventilation employed (spontaneous breathing or mechanical ventilation with positive end-expiratory pressure). Averaged values of  $T_{2S}$  ranged from 150 msec to 544 msec and strongly support our association of  $T_{2S}$  with airspace fluid. Moreover, the dependence of  $T_{2S}$  on the mode of ventilation employed supports the conclusions of Kveder et al. (8), that relaxation rates are proportional to the tissue surface area in contact with the airspace fluid, because water proton relaxation within the lung arises from a rapid exchange between bulk water and water protons which are tightly bound to biopolymer segments.

One aspect of the observed transverse relaxation components that has not been discussed in Chapter 2 or Appendix 3.2, is the relative amount of signal,  $\rho_F$  or  $\rho_S$ , contributing to either the faster relaxing or the slower relaxing component. Although Figure 2.3a demonstrates that there is little or no proton NMR signal obtained from the normal lung, within 15 minutes after fluid instillation, 60% to 80% of the NMR signal corresponded to the relaxation component that we have associated with intracellular and interstitial fluid. To investigate this surprising result we must keep in mind that virtually all of the naturally occurring lung fluid is in the intracellular and interstitial spaces, and also contributed to our relaxation time measurements. Moreover, the amount of naturally occurring lung fluid in a

cat was estimated from gravimetric measurements of 43 normal lung lobes to be 4.0 g H<sub>2</sub>O per kg of body weight. The instillate was delivered to an estimated 14% of the total lung, however, and this portion of the normal lung contains roughly 0.56 g H<sub>2</sub>O/kg body weight. In comparison, the instillate itself was delivered at a dose of 0.7 ml/kg, a dose which resulted in 0.68 g H<sub>2</sub>O/kg body weight in the airspaces. Based on these values, the value of  $\rho_F$  immediately after fluid instillation is estimated to be

$$(4.1) \quad \rho_F = \left( \frac{0.56 \text{ g H}_2\text{O/kg}}{0.68 \text{ g H}_2\text{O/kg} + 0.56 \text{ g H}_2\text{O/kg}} \right) = 0.45$$

This estimate suggests that because fluid was being cleared from the airspaces and passing through the interstitium, the minimum proportion of the NMR signal that could be expected to come from the tissue-bound fluid was approximately 45%. Support for our association of  $T_{2F}$  with the tissue-bound fluid is provided by this estimate, but it does not explain why  $\rho_F$  was consistently observed to be as high as 60% to 80%.

As surprising as the seemingly high observed values of  $\rho_F$ , is the fact that the values of  $\rho_F$  and  $\rho_S$  changed very little during the observed fluid clearance, even with as much as 60% of the instilled fluid leaving the lung in some cases. To reconcile both of these features of our data at once, however, one can postulate that fluid was effectively being cleared from both the faster relaxing compartment (the cells and/or interstitium), and the more slowly relaxing compartment (the airspace fluid), by means of a flux of fluid from the airspaces into the interstitial space of the lung. Moreover, this fluid flux must be slow on a  $T_2$  time scale but fast relative to the 4 hour time course of these experiments. This postulate is supported by the observations of Gee and Staub (6) that perivascular fluid cuffs

were formed within 10 minutes of fluid instillation into the airspaces of a dog lung by means of a relatively rapid initial fluid flux from the airspaces to the interstitium.

### **4.3 A Model of the Lung Fluid Balance**

Using all of our NMR observations, we are now able to construct a detailed postulate of the mechanisms responsible for the clearance of instilled alveolar fluid, and, by inference, for maintaining the alveolar fluid balance. We can assume that the observed clearance of  $^{125}\text{I}$ -albumin from the airspaces of the lung was likely via pinocytotic vesicles as demonstrated by Bensch et al (3). The fluid clearance, however, is governed by several mechanisms which include a passive mechanism (dominated by hydrostatic and osmotic forces with fluid movements via paracellular pathways), and active cellular transport. Passive fluid movements are responsible for the formation of perivascular fluid cuffs within ~10 minutes after the instillation of fluid as described by Gee et al (6) and as indicated by transverse relaxation component populations. Also, capillary blood hydrostatic pressures may or may not have been modified by the instillation of fluid into the airspaces of the lung. The fact that alveolar fluid protein osmotic pressures are highly elevated by differential alveolar fluid and protein clearances, on the other hand, has been well demonstrated (11). Nonetheless, active fluid transport mechanisms are expected to be the primary sources of lung fluid absorption and secretion, as well as being the mechanisms which are stimulated as a result of PAF action to enhance airspace fluid absorption.

In order to estimate the relative contributions of each of the aforementioned mechanisms to the maintenance of the lung fluid balance, and to

the clearance of instilled alveolar fluid, we have employed a mathematical model of the lung fluid balance. The basis of the model is that described by Blake (4) which describes the effects of hydrostatic and osmotic forces on fluid fluxes across the alveolar epithelium and across the capillary endothelium. Moreover, the parameters used in the model are to simulate one lung lobe of a 3 kg cat, in which an estimated alveolar surface area of 5000 cm<sup>2</sup> is in contact with 2.1 ml of serum. Additional parameters used in the development of this model are listed in table 4.1 and a flow chart which details the computer algorithm is included in Appendix 4.1.

The parameters used to describe the cat's lung fluid balance were first examined with a model of the normal lung which included only hydrostatic and osmotic forces. This model demonstrated fluid movements only from the blood into the interstitial space, and the rate at which lymphatics remove fluid from the interstitium was adjusted to maintain the lung in a steady state with the interstitial fluid volume listed in table 4.1. The number of endothelial pores per unit area was also adjusted to maintain the lymph/plasma protein concentration ratio near the expected value of 0.7 (12). Fluid movements across the alveolar epithelium were negligible in this model of the normal lung. Moreover, altering the model to include serum in the airspaces had a negligible effect on computed trans-epithelial fluid fluxes. Thus, this initial model of the lung fluid balance was unable to describe the lung fluid clearances that we have observed.

Epithelial pore diameter	0.8 nm (12)
Number of epithelial pores	$2.0\text{e}+10$ pores/cm <sup>2</sup>
Endothelial pore sizes	2 nm and 12.5 nm (4)
Ratio of 2 nm pores/12.5 nm pores	1000/1 (4)
Total number of endothelial pores	$2.0\text{e}+10$ pores/cm <sup>2</sup>
Alveolar diameter	100 $\mu\text{m}$ (14)
Distance across cell membranes	0.5 $\mu\text{m}$ (13)
Diameter of albumin molecule	3.4 nm (4)
Diameter of water molecule	0.15 nm (4)
Temperature	311.7 K
Flow rate	$1.44\text{e}-03$ ml/sec

**Before fluid instillation:**

Alveolar fluid volume	0.100 ml
Interstitial fluid volume	0.25 ml
Relative airspace pressure	0 mmHg
Relative interstitial pressure	-4 mmHg (9)
Relative capillary pressure	7 mmHg (10)
Interstitial protein concentration	$5.65\text{e}-07$ moles/ml (12)
Interstitial oncotic pressure	12 mmHg (12)
Capillary protein concentration	$7.97\text{e}-07$ moles/ml (12)
Capillary oncotic pressure	20 mmHg (12)

**After instillation of 2.10 ml of fluid:**

Airspace protein concentration	$7.97\text{e}-07$ moles/ml
Airspace oncotic pressure	20 mmHg

**Table 4.1** Parameters used in a mathematical model of the alveolar fluid exchange

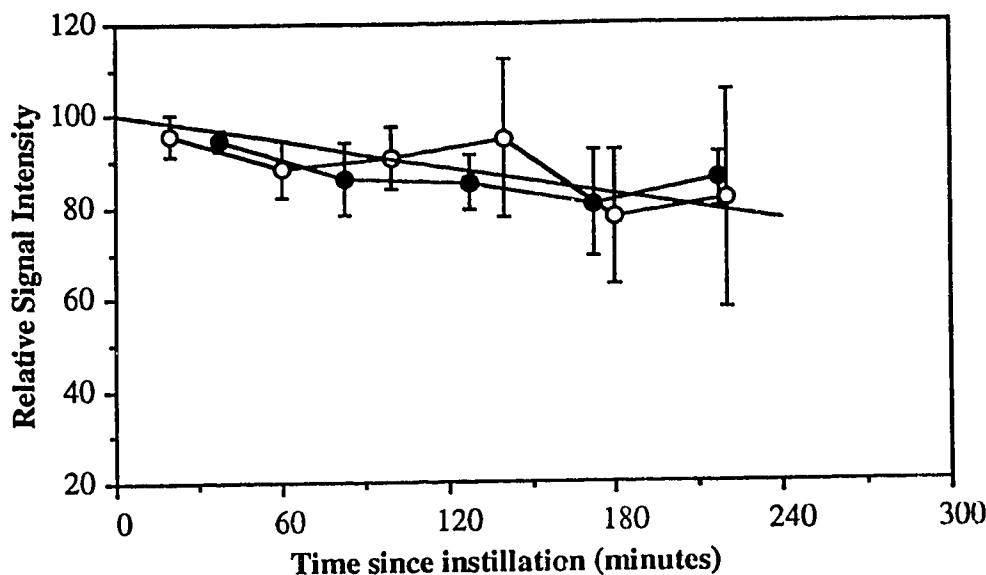


**Figure 4.1** The time courses of fluid clearance after the instillation of serum (black circles) and SLS (white circles) and the result of a mathematical model of the lung fluid clearance (solid line).

In order to simulate the observed clearance of SLS, and the corresponding time courses of changes in the lung's  $H_2O$  and  $D_2O$  contents, it was necessary to include in the model an epithelial fluid absorption rate of 175 nl/sec and a fluid secretion rate of 141 nl/sec. For the purposes of this model it was assumed that fluid movements across the endothelium were due to passive forces via paracellular pathways only, because the endothelial permeability is much higher than that of the alveolar epithelium (13). With the addition of active fluid fluxes across the epithelium, we were able to generate the computed time course of lung fluid clearance shown in figure 4.1. The simulated fluid clearance is displayed in comparison to the experimentally observed fluid clearance of serum and of SLS. Also, figure 4.2 illustrates the simulated time courses of the lung's  $H_2O$  and  $D_2O$  contents after the instillation of SLS, in comparison to the corresponding experimentally observed time courses of the lung's  $H_2O$  and  $D_2O$  contents.

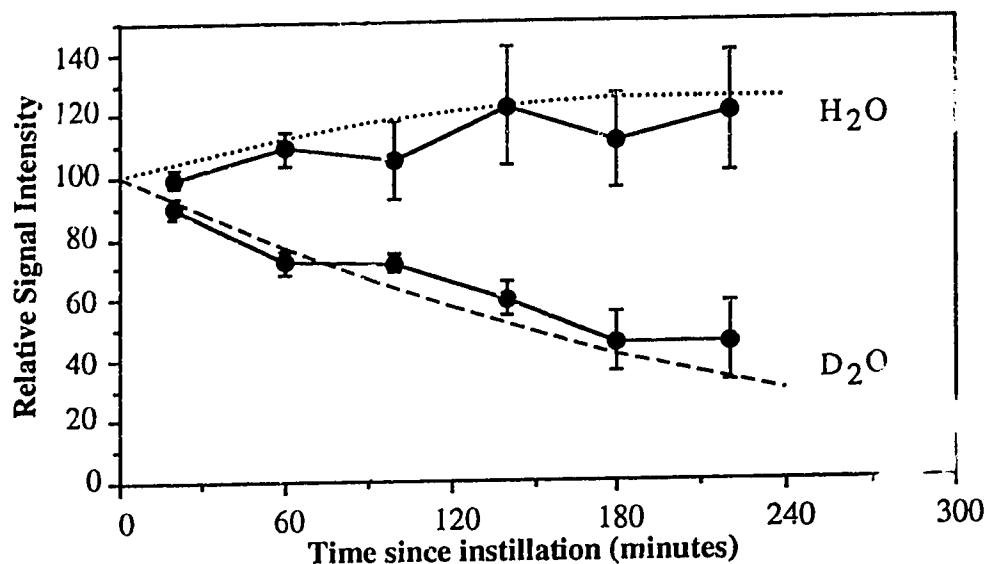


**Figure 4.2** The time courses of the changes of the H<sub>2</sub>O and D<sub>2</sub>O contents of the lung after instillation of SLS. The corresponding time courses simulated with a mathematical model of the lung fluid clearance are indicated by the dotted line and the dashed line, respectively. Results of the mathematical model are plotted at 15 minute intervals.

The active fluid absorption and secretion rates used to simulate the alveolar epithelium in the model were initially chosen to be the 4 hour average rates observed experimentally for the entire air-blood barrier, 80 nl/sec and 55 nl/sec, respectively. These values were then adjusted in the model to be 175 nl/sec and 141 nl/sec, respectively, to minimize the sum of the squares of the differences between our experimental measurements and the simulated amounts of H<sub>2</sub>O and D<sub>2</sub>O in the lung, at each of the 6 different measurement points in time after fluid was instilled. This mathematical model is thus sufficiently constrained that the estimated rates of absorption and secretion required to simulate our experimental observations are expected to be unique solutions. Furthermore, the simulated fluid clearance depends very little on the parameters we have assumed to describe passive fluid movements in the lung (listed in Table 4.1), and supports

our conclusion that alveolar fluid clearance is dominated by active transport mechanisms. As a result, the simulated clearance depends primarily on the epithelial absorption and secretion rates used in the model and we can therefore assume these to be reasonable estimates of those in the cat lung. This assumption is supported by the fact that Basset et al. (1) have observed an alveolar absorption rate of 134 nl/sec from excised rat lungs having an estimated alveolar surface area of 5000 cm<sup>2</sup>, in comparison to our estimated absorption rate of 175 nl/sec for the same alveolar surface area.

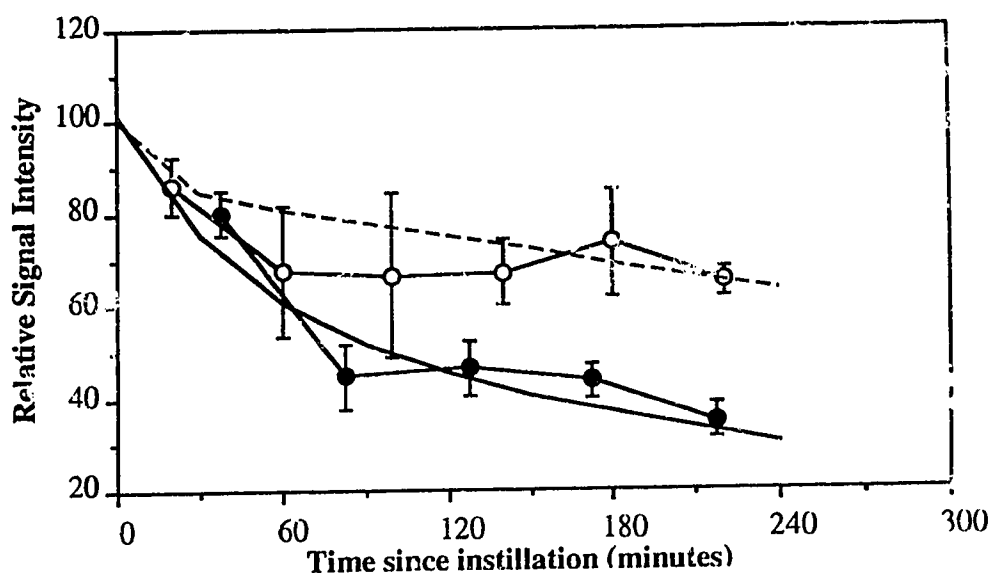


**Figure 4.3** The time courses of fluid clearance after the instillation of serum plus PAF (black circles) and SLS plus PAF (white circles) and the results of a mathematical model of the clearance of serum plus PAF (solid line) and the clearance of SLS plus PAF (dashed line) from the airspaces of the lung. Results of the mathematical model are plotted at 15 minute intervals.

Simulations of the observed fluid clearance from the lung after the instillation of SLS plus PAF, were generated by introducing supplemental epithelial fluid absorption and secretion at rates of 1520 nl/sec and 887 nl/sec,

respectively. Also, it was necessary that these supplemental absorption and secretion rates resulting from the addition of PAF to the instillate, decay exponentially with a half time of 8.3 minutes measured from the time of fluid instillation into the lung. Because bi-directional fluid movements could not be monitored with serum-based instillates, to simulate the observed clearance of serum plus PAF it was necessary to assume the same supplemental epithelial absorption and secretion rates as those introduced to model the clearance of SLS plus PAF, but the duration of PAF action was assumed to be greater for serum-based instillates.

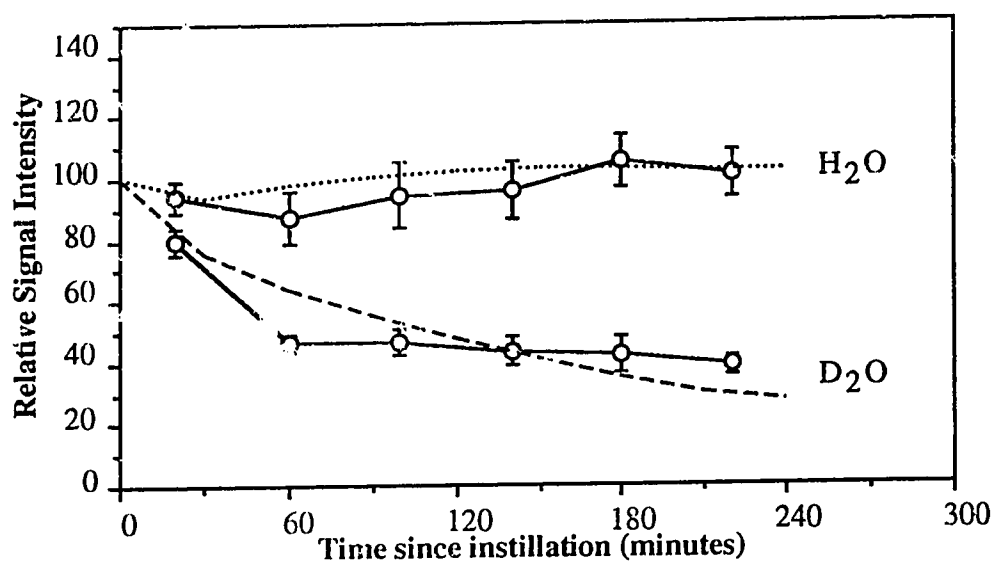


**Figure 4.4** The time courses of the changes of the H<sub>2</sub>O and D<sub>2</sub>O contents of the lung after instillation of SLS plus PAF. The corresponding time courses simulated with a mathematical model of the lung fluid clearance are indicated by the dotted line and the dashed line, respectively. Results of the mathematical model are plotted at 15 minute intervals.

To model the clearance of serum plus PAF then, the decay half-time of the supplemental active fluid fluxes was increased to 33.3 minutes. The simulated clearances of serum plus PAF, and of SLS plus PAF, are shown in figure 4.3 in

comparison to the corresponding experimentally observed clearance time courses of these solutions. Also, the time courses of the experimentally observed  $\text{H}_2\text{O}$  and  $\text{D}_2\text{O}$  contents of the lung after the instillation of SLS plus PAF are shown in figure 4.4 in comparison to the corresponding time courses generated with the mathematical model.

The simulated clearances of either serum plus PAF, or SLS plus PAF, that we have generated may not be unique because we cannot be certain of the effects of PAF on the alveolar epithelium. However, we can be certain that the mechanisms we have included in the model to simulate the action of PAF are at least plausible. We have observed that the absorption of fluid from the alveolar space is enhanced with PAF, and it has been shown by others that PAF is rapidly metabolized by alveolar type II epithelial cells (7) so that the expected duration of PAF action in the airspaces is limited. Surprisingly though, we have observed experimentally that PAF only enhances the rate of fluid absorption from the airspaces, and yet we have found it necessary to increase the rates of both epithelial fluid absorption and secretion in order to simulate the observed fluid clearances with PAF. The difference between our mathematical model and our experimental observations lies in the fact that experimentally we observed the effects of fluid movements across the entire air-blood barrier, and experimentally we were unable to observe separately the fluid movements across the alveolar epithelium and the capillary endothelium. Nonetheless, we have succeeded in simulating our experimental observations, indicating that the temporary enhancement, or augmentation, of both epithelial absorption and secretion mechanisms is a plausible explanation of the effects of PAF on the epithelial fluid transport mechanisms. Also, this model of the lung fluid balance has demonstrated that the clearance of fluid from the alveolar space of a relatively

normal lung is the result of active fluid transport mechanisms with the effects of hydrostatic and osmotic forces being of little consequence, as was first demonstrated by Basset et al. (1).

The overall picture of the lung fluid balance that unfolds from our experimental observations, and mathematical modeling of the lung, is as follows. The balance of fluid in the normal lung is dominated by active fluid transport mechanisms. Moreover, these mechanisms are expected to be responsible for transporting fluid in both directions across the alveolar epithelium of the normal lung to maintain a normal amount of alveolar surface fluid (5). These mechanisms must of course work in concert with those mechanisms responsible for maintaining the integrity of the surfactant layer which lines the alveolar surface. The interstitial fluid is reasonably expected to be held in balance by the lymphatics which routinely remove any excess of fluid that passes across the capillary endothelium as a result of hydrostatic and protein osmotic pressures. The role of the lymphatics in the lung fluid balance has already been described in considerable detail by Matthay (12) and Staub (13). In the event of a considerable increase in the capillary blood pressure, however, the lymphatic fluid clearance cannot match the flow into the interstitial space and interstitial edema quickly develops. Also, if the increase in capillary pressure is sufficient, the active transport mechanisms in the epithelium can most certainly become overpowered and alveolar edema results. Similarly, in the event of increased epithelial permeability, the mechanisms of active fluid transport across the epithelium likely become ineffective (2) and so, once again, the passive forces affecting fluid movement across the epithelium can become dominant and result in alveolar edema. Once alveolar flooding has occurred, if hydrostatic pressures and membrane permeabilities are restored to normal, it appears that fluid is rapidly

taken up into perivascular fluid cuffs as described by Gee et al. (6) and bi-directional fluid transport across the epithelium continues and once again dominates the lung fluid balance mechanisms. Once the excess fluid is moved into the interstitial space it can be cleared fairly rapidly either via the lymphatics or by crossing the endothelium to enter the blood. Thus, the lung is returned to its normal state and is able once again to continue in its primary function of gas exchange.

#### **4.4 References**

- 1      Basset G., C. Crone, G. Saumon, Significance of active ion transport in transalveolar water absorption: a study on isolated rat lung. *J. Physiol.*, **384**, 311-324 (1987).
  
- 2      Basset G., C. Crone, G. Saumon, Fluid absorption by rat lung *in-situ*. Effects of ouabain on sodium entry in the luminal membrane of alveolar epithelium. *J. Physiol.*, **384**, 325-345 (1987).
  
- 3      Bensch K. G., E. A. M. Dominguez, Studies on the pulmonary air-tissue barrier. Part IV: cytochemical tracing of macromolecules during absorption. *Yale Journal of Biol. and Med.*, **43**, 236-241 (1971).
  
- 4      Blake L. H., Ch. 5 of *Lung Water and Solute Exchange*, Ed. by N. C. Staub, (Marcel Dekker Inc., New York, 1978).
  
- 5      Frizzell R. A., Role of absorptive and secretory processes in hydration of the airway surface. *Am. Rev. Resp. Dis.*, **138**: s3-s6 (1988).
  
- 6      Gee M. H. and N. C. Staub, Role of bulk fluid flow in protein permeability of the dog lung alveolar membrane. *J. Appl. Physiol.: Respirat. Environ. Exercise Physiol.*, **42**(2), 144-149 (1977).
  
- 7      Kumar R., R. J. King, H. M. Martin, D. J. Hanahan, Metabolism of platelet-activating factor (alkylacetylphosphocholine) by type-II epithelial cells and fibroblasts from rat lungs. *Biochim. Biophys. Acta*, **917**, 33-41 (1987).

- 8 Kveder M. et al., Water proton NMR relaxation mechanisms in lung tissue. *Mag. Res. Med.*, **7**, 432-441 (1988).
- 9 Levitzky M. G., *Pulmonary Physiology*, 3<sup>rd</sup> Ed., (McGraw-Hill Inc., New York, 1991).
- 10 Lim T. P. K., *Physiology of the Lung* (Charles C. Thomas, Springfield, 1983).
- 11 Matthay M. A., C. C. Landolt, N. C. Staub, Differential liquid and protein clearance from the alveoli of anesthetized sheep. *J. Appl. Physiol.: Respirat. Environ. Exercise Physiol.*, **53**(1), 96-104 (1982).
- 12 Matthay M. A., Resolution of pulmonary edema, *Clin. Chest Med.*, **6**(3), 521-545 (1985).
- 13 Staub N. C., *Basic Respiratory Physiology* (Churchill-Livingstone Inc., New York, 1991).
- 14 Staub N. C., Pulmonary Edema, *Physiol. Rev.*, **54**(3), 678-811 (1974).

## **5.0 Summary**

Light microscopy of the lung tissue after either serum or serum plus PAF instillation showed no morphological evidence of inflammation and that the alveolar epithelium and capillary endothelium were apparently intact 4 hours after fluid instillation. Also, the  $^{125}\text{I}$ -albumin clearance rate was  $\sim 3\%/ \text{hour}$  regardless of whether the instillate was serum, serum plus PAF, SLS, or SLS plus PAF. These observations support our belief that NMR and gravimetric measurements were done in normal lungs of a cat, and should have direct physiological application.

The proton NMR images that we have obtained, have enabled us to observe, non-invasively, the time course of alveolar fluid clearance in living cats. Moreover, by employing both  $^1\text{H}$  and  $^2\text{H}$  NMR techniques we have been able to quantify the absorption and secretion components of this net fluid clearance. The clearance of a serum (or serum-like) solution from the alveolar spaces was observed to proceed at a rate of approximately  $17\%/4 \text{ hours}$  ( $t_{1/2} \sim 1.4 \text{ hours}$ ), and was the net result of fluid absorption and secretion rates of  $55\%/4 \text{ hours}$  and  $38\%/4 \text{ hours}$ , respectively. The quoted rates of fluid movement are expressed as percentages of the initially instilled amount. These results are consistent with a model in which the net clearance of alveolar fluid is primarily the result of solute-coupled ion transport, with passive fluid movements being of secondary importance.

With the addition of PAF to the serum instillate, the clearance was biphasic with an initial rapid clearance with a  $t_{1/2}$  of only  $\sim 30 \text{ minutes}$ , followed by a slower, more sustained clearance similar to that observed after the instillation of

serum alone. Similarly, in the first hour after fluid instillation, the rate of absorption of SLS was increased from 28%/hour to 54%/hour by the addition of PAF, but the fluid secretion rate remained unchanged at approximately 20%/hour. However, the effect of PAF on the clearance of serum was considerably more pronounced than that observed with SLS, as demonstrated by their respective net 4 hour clearances of 65% and 30%, respectively. This dependence of PAF action on the instilled fluid (serum-based or SLS-based) indicates that there are one or more components of serum, not included in the SLS preparation, that act to enhance the effect of PAF on alveolar fluid clearance. Furthermore, we have proposed that PAF may act by increasing cytosolic  $\text{Ca}^{2+}$  in pulmonary epithelial cells to enhance the absorptive function of the epithelium or by increasing levels of intracellular cAMP, thereby stimulating epithelial ion transport.

Transverse relaxation curves obtained from proton spin-echo images were repeatedly resolved into two relaxation components, indicating that we were detecting NMR signal from at least two lung water compartments. We have demonstrated the faster relaxing of these two components (giving rise to 60% to 75% of the NMR signal) to be associated with tissue-bound fluid in the intracellular and interstitial spaces of the lung, and the more slowly relaxing component to be associated with the instilled alveolar fluid. Whereas the tissue-bound fluid had a relatively constant  $T_2$  value of 25 msec to 32 msec, the airspace fluid  $T_2$  value varied with the instilled alveolar fluid (serum-based or SLS-based) and with the mode of ventilation (spontaneous breathing or mechanical ventilation with PEEP), and ranged from 150 msec to 544 msec. These observations are consistent with the conclusion that lung water proton relaxation rates are proportional to the tissue surface area in contact with the airspace fluid, because

relaxation within the lung arises from a rapid exchange between bulk water and water protons which are tightly bound to biopolymer segments.

The combination of  $^1\text{H}$  and  $^2\text{H}$  NMR techniques we have employed has enabled us to quantify not only the rate of alveolar fluid clearance, but also the rates of alveolar fluid absorption and secretion in the lungs of a living animal, for the first time. Also, these techniques are sufficiently sensitive that we were able to assess the effects of PAF on the mechanisms which influence alveolar fluid clearance, and which presumably play a role in the maintenance of the lung fluid balance. Thus, future research in this area should have two distinct goals, namely, the clinical application of the  $^1\text{H}$  NMR imaging techniques that we have developed, and the further definition of alveolar fluid clearance mechanisms and their modification with PAF, in animal models of alveolar edema. Further studies should include monitoring the time course of changes in the extravascular lung water content, and of proton transverse relaxation times of lung fluid, in patients with chronic lung diseases as well as during the resolution phase of acute pulmonary edema. Future research with animal models of alveolar edema should also include evaluations of the effects of agents which block the active cellular transport and/or uptake of  $\text{Na}^+$ ,  $\text{Cl}^-$  and  $\text{Ca}^{2+}$  ions, on the absorptive and secretory functions of the pulmonary air-blood barrier. In addition, monitoring the clearance of  $\text{Na}^+$  from the airspaces, and the effect of PAF on this clearance, should be attempted with  $^{23}\text{Na}$  NMR techniques.

This project has demonstrated the unique capabilities of NMR measurement techniques for monitoring the dynamics of extravascular lung fluid, non-invasively, in a living animal. Not only have these NMR techniques enabled us to observe separately the absorption and secretion of airspace fluid, but through

transverse relaxation time measurements have also enabled us to distinguish between tissue-bound and airspace fluids. Furthermore, the ability to monitor bi-directional fluid movements across the pulmonary air-blood barrier may prove to be a powerful research tool. As a result, it is hoped that the successful completion of this project will provide an impetus for future NMR studies of the lung fluid balance, in both research and clinical settings.

### Appendix 1.1: Detailed Calculations of the Motions of Spins in the Presence of a Rotating Magnetic Field

In order to describe the motion of the net magnetization of a system of non-interacting spins under the influence of a rotating magnetic field, it is useful to work in the rotating frame of reference and to assume the simplest case to start. The simplest case is that in which the rotating magnetization,  $\mathbf{B}_1$ , and the rotating frame of reference have the same angular velocity,  $\Omega$ , which in combination with a static  $B_0$  field, provides an effective field in the rotating frame of reference,  $\mathbf{B}_{\text{eff}}$ , which is defined to be along the  $z'_p$  axis as shown:

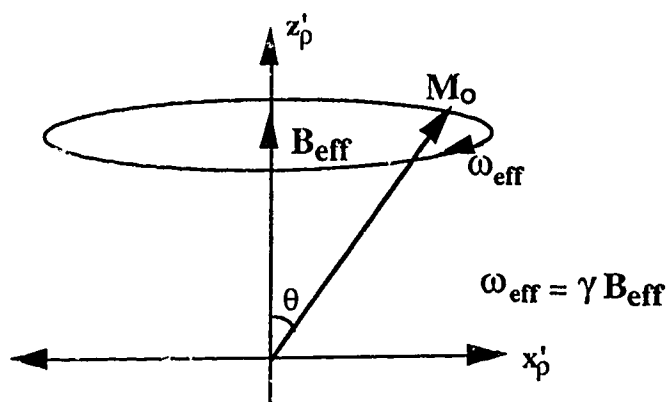


Figure A1.1.1 Precession of the net magnetization,  $M_0$ , about an effective magnetic field in the rotating frame of reference,  $\mathbf{B}_{\text{eff}}$ , defined to be along the  $z'_p$  axis.

The magnetization components in the  $x'_p y'_p$  plane and along the  $z'_p$  axis are described by:

$$(A1.1.1) \quad M_{x'} = M_0 \sin\theta \cos(\omega_1 t) \hat{i}_p'$$

$$(A1.1.2) \quad M_{y'} = -M_0 \sin\theta \sin(\omega_1 t) \mathbf{j}_{p'}$$

$$(A1.1.3) \quad M_{z'} = M_0 \cos\theta \mathbf{k}_{p'}$$

where  $\mathbf{i}_{p'}$ ,  $\mathbf{j}_{p'}$ , and  $\mathbf{k}_{p'}$  are unit vectors along the  $x_{p'}$ ,  $y_{p'}$  and  $z_{p'}$  axes respectively.

To expand this description to the more general case in which the effective field is not aligned with the  $z$  axis of the coordinate system, we can rotate the coordinate system through an angle  $\theta$ . This coordinate rotation allows us to describe the case in which the net magnetization was initially parallel to  $\mathbf{B}_0$  along the  $z$  axis, before the application of  $\mathbf{B}_{\text{eff}}$  at the angle  $\theta$  from the  $z$  axis, as shown:

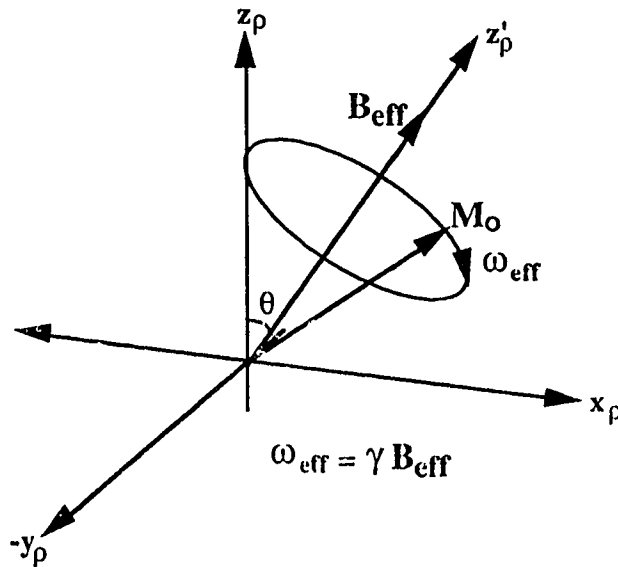


**Figure A1.1.2** Precession of the net magnetization,  $\mathbf{M}_0$ , about an effective magnetic field in the rotating frame of reference,  $\mathbf{B}_{\text{eff}}$ .

Equations which describe a rotation of the  $(x_p', y_p', z_p')$  coordinate system to the  $(x_p, y_p, z_p)$  system are as follows

$$(A1.1.4) \quad x_p = x_p' \cos\theta - z_p' \sin\theta$$

$$(A1.1.5) \quad z_p = z_p' \cos\theta + x_p' \sin\theta$$

$$(A1.1.6) \quad y_p = y_p'$$

Applying this coordinate transformation to equations A1.1.1 to A1.1.3 yields

$$(A1.1.7) \quad M_{xp} = M_o (\cos(\omega_1 t) - 1) \sin\theta \cos\theta$$

$$(A1.1.8) \quad M_{yp} = -M_o \sin\theta \sin(\omega_1 t)$$

$$(A1.1.9) \quad M_{zp} = M_o [\cos^2\theta + \sin^2\theta \cos(\omega_1 t)]$$

As a result, the magnetization component in the  $x_p y_p$  plane, under the influence of a rotating  $B_1$  field, can be described by the expression

$$(A1.1.10) \quad M_{xpy_p} = M_o \sin\theta [\cos^2\theta (\cos(\omega_1 t) - 1)^2 + \sin^2(\omega_1 t)]^{1/2}$$

where the values of  $\cos\theta$  and  $\sin\theta$  are defined in terms of the applied fields as follows:

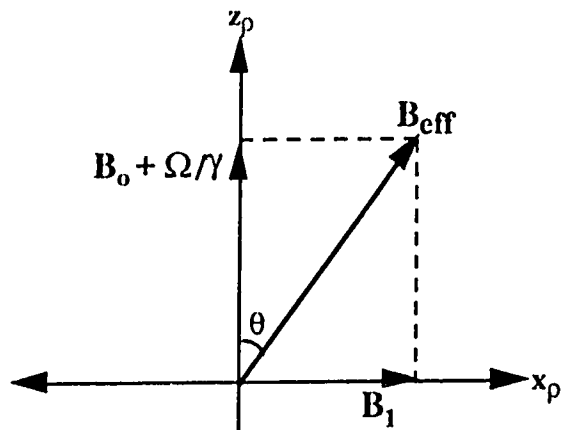


Figure A1.1.3 Definition of the effective magnetic field in the rotating frame of reference.

$$(A1.1.11) \quad B_{\text{eff}} = [(B_0 + \Omega/\gamma)^2 + B_1^2]^{(1/2)}$$

$$(A1.1.12) \quad \sin\theta = B_1/B_{\text{eff}}$$

$$(A1.1.13) \quad \cos\theta = (B_0 + \Omega/\gamma)/B_{\text{eff}}$$

### **Appendix 3.1: Deuteron NMR Techniques Employed for Monitoring Instilled Alveolar SLS, or SLS plus PAF**

In order to determine the optimal  $^2\text{H}$  NMR technique for monitoring the spatial distribution of instilled alveolar fluid, we assessed the suitability of gradient-recalled echo and free-induction decay (FID) imaging schemes. The 8 msec minimum required by our NMR hardware to form a gradient-recalled echo gave rise to insufficient sensitivity for gradient-recalled echo imaging. This time is considerably longer than the transverse relaxation time,  $T_2^*$ , with which the echo amplitude decays, and which for SLS deuterons in the lung is roughly 3 msec.

The FID imaging scheme, although being more prone to image artifacts than gradient-recalled echo imaging (4), provided a factor of 14 greater sensitivity than the latter method, sufficient sensitivity to obtain images of instilled SLS in the lungs of a living cat. The improved sensitivity resulted from the ability to sample the peak signal amplitude only 30  $\mu\text{s}$  after the RF excitation pulse was transmitted. As a result, the  $^2\text{H}$  NMR signal intensity was not degraded by the rapid deuteron transverse magnetization decay in the lung. Images were obtained by applying a reconstruction from projections technique to eight NMR signal projections from a transverse imaging slice. The fact that only eight projections were used limited the spatial resolution to roughly 3 mm. Because the NMR sensitivity of deuterons is only 1% of that of protons, it was necessary to average 512 FIDs for each projection, over a period of 51 seconds, to achieve a projection signal amplitude to noise ratio of approximately 10:1 immediately after SLS instillation. Although an increase in the number of projections and signal averages would have improved the image quality, the total number of acquisitions was limited to 4096 (8 projections x 512 averages) by the capacity of the computer memory allocated for storing

magnetic field gradient values for each acquisition. The image was reconstructed by means of a back-projection algorithm (2, 3).

To achieve the maximum sensitivity possible to  $^2\text{H}$  NMR, and hence the maximum precision in the measurements with the hardware employed for this study, it was necessary to forgo spatial resolution altogether and measure the global  $^2\text{H}$  NMR signal intensity with a spectroscopic technique similar to that used by Kim et al. (1). To maximize the weak deuteron signal in a given time, the total signal intensity was measured from 1000 spectral acquisitions with a repetition time of 100 msec. When applied to detecting SLS immediately after instillation into a cat's lung lobe this spectral acquisition technique was able to provide a signal to noise ratio as high as 50:1 in 100 seconds.

### **References**

- 1 Kim S. G. and J. J. H. Ackerman, Multicompartment analysis of blood flow in tissue perfusion employing D<sub>2</sub>O as a freely diffusible tracer: a novel deuterium NMR technique demonstrated via application with Murine RIF-1 tumors. *Mag. Res. Med.*, 8: 410-426 (1988).
- 2 Link J. and J. Seelig, Comparison of deuterium NMR imaging methods and application to plants. *J. Mag. Res.*, 89: 310-330 (1990).
- 3 Mansfield P., and P. G. Morris, *NMR Imaging in Biomedicine* (Academic Press, New York, 1982).
- 4 Muller S. and J. Seelig, In vivo NMR imaging of deuterium. *J. Mag. Res.*, 72: 456-466 (1987).

### **Appendix 3.2: Proton Transverse Relaxation Time Measurements of Lung Water, after Instillation of either SLS or SLS plus PAF**

Measurements of lung water proton transverse relaxation times were carried out after the instillation of SLS-based instillates to supplement those obtained with serum-based instillates (Chapter 2). These measurements enabled us to monitor changes in the microscopic environment experienced by lung water protons during the clearance of instilled alveolar fluid.

#### **Methods**

Transverse relaxation time measurements of lung water protons were obtained from the lungs of anesthetized, ventilated cats, after the instillation of either SLS or SLS plus PAF, as described in Chapter 3. For this study, transverse magnetization decay curves were described by integrating the pixel intensities of the lung region of interest in each of 16 spin-echo images. These spin-echo images were acquired using a Carr-Purcell-Meiboom-Gill (CPMG) sequence having an inter-echo interval of 18.1 msec. Spatially averaged transverse relaxation times were then derived for that lung region of interest using a non-linear least squares algorithm (1).

#### **Results**

The decay of the transverse proton magnetization from the region of interest in the fluid-instilled lung, could be reproducibly resolved into two exponential components, with characteristic times  $T_{2F}$  (fast relaxing) and  $T_{2S}$  (slow relaxing). Measurements of  $T_{2F}$  and  $T_{2S}$  (again time averaged over the 40 minute intervals

used for the integrated signal intensity measurements), are shown as a function of time following instillation in Figure A3.2.1.

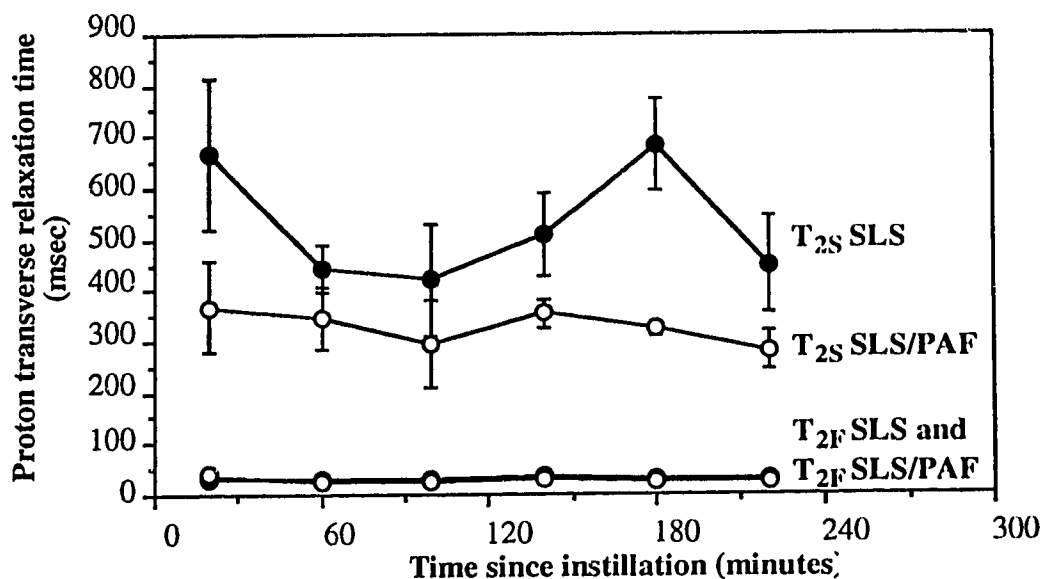


**Figure A3.2.1** A comparison of the time course of lung water proton transverse relaxation times of the more slowly relaxing component,  $T_{2S}$ , and of the faster relaxing component,  $T_{2F}$ . White circles are used to indicate relaxation times measured after the instillation of SLS plus PAF whereas the black circles indicate measurements obtained after the instillation of SLS alone. The two time courses of  $T_{2F}$  values illustrated in this figure overlap so that one obscures the other. All measurements are averages over 40 minute data acquisition periods and over 4 cats, with error bars indicating the standard error of the mean.

These results indicate that the measured transverse relaxation properties do not vary systematically over the 4 hours of observation. Assuming that fluctuations are due to measurement uncertainty we can derive an overall average (over 4 hours) of the relaxation times. All of the average relaxation times are expressed as the mean of  $m$  measurements, plus or minus the standard error of the mean. After the instillation of SLS the overall value of  $T_{2F}$  was  $32 \text{ msec} \pm 1 \text{ msec}$  ( $m = 18$ ), and was similar

to the value of  $29 \text{ msec} \pm 2 \text{ msec}$  ( $m = 25$ ) measured after instilling SLS plus PAF. The overall average value of  $T_{2S}$ , on the other hand, was  $544 \text{ msec} \pm 55 \text{ msec}$  ( $m = 18$ ) after the instillation of SLS alone, and  $337 \text{ msec} \pm 13 \text{ msec}$  ( $m = 25$ ) for the case when PAF was added to the SLS instillate. Throughout the 4 hour observation period the proportion of the total signal from the more slowly relaxing component,  $p_S$ , was  $25\% \pm 2\%$  ( $m = 43$ ), irrespective of whether SLS or SLS plus PAF was instilled.

### **Discussion**

The ability to decompose the transverse proton magnetization decay into two reproducible components indicates that we were detecting signal from two distinct fluid compartments in the lung. These two compartments can be identified by their transverse relaxation times,  $T_{2F}$  and  $T_{2S}$ , respectively. Previously (6) we have associated the faster relaxing water protons with tissue bound fluid in the intracellular and interstitial spaces of the lung, whereas the more slowly relaxing water protons were associated with the airspace fluid.

Comparison of the present results with those from our previous study demonstrated that spatially and time averaged values of  $T_{2F}$  were similar for SLS-based and serum-based instillates (range of 25 msec to 32 msec). Moreover, the small difference in  $T_{2F}$  observed after the instillation of either SLS ( $32 \text{ msec} \pm 1 \text{ msec}$ ) or SLS plus PAF ( $29 \text{ msec} \pm 2 \text{ msec}$ ) is not regarded as significant and does not support a conclusion of a PAF dependence. In contrast, the similarly averaged  $T_{2S}$  value measured after the instillation of serum-based instillates (range of 150 msec to 170 msec) was considerably shorter than that with SLS-based instillates (range of 337 msec to 544 msec) (6). This difference is possibly a consequence of

the different modes of ventilation employed with the two instillate types since it is expected that  $T_{2S}$  values are elevated for fluid in larger airways (6). For example, the cat was allowed to breathe spontaneously after instilling a serum-based solution (6), whereas after the instillation of an SLS-based solution (Chapter 3) mechanical ventilation was employed with a positive end-expiratory pressure of 2 cmH<sub>2</sub>O, resulting in an increased average lung volume. Similarly, because PAF has been demonstrated to cause bronchoconstriction in a variety of animal species (5), the use of mechanical ventilation is suspected of enabling us to distinguish between  $T_{2S}$  values measured with either SLS (544 msec  $\pm$  55) or SLS plus PAF (337 msec  $\pm$  13 msec) in the airspaces.

The dependence of  $T_{2S}$  values on the airway diameter is consistent with the conclusion that  $T_{2S}$  arises from a fast exchange between the bulk airspace water and a second faster relaxing water component, possibly that adsorbed to cellular surface proteins as suggested by Kveder et al. (2). This conclusion is also supported by the fact that  $T_{2S}$  does not appear to have a strong dependence on the  $T_2$  of the bulk airspace fluid. Our results indicate that  $T_{2S}$  is not sensitive to the considerable increase in the airspace fluid protein concentration (and corresponding decrease in the bulk airspace fluid  $T_2$  (4)) that occurs over 4 hours of fluid clearance (3).

## **References**

- 1 Bevington P. R., *Data Reduction and Error Analysis for the Physical Sciences*, (McGraw Hill, New York, 1969).
- 2 Kveder M. et al., Water proton NMR relaxation mechanisms in lung tissue. *Mag. Res. Med.*, **7**, 432-441 (1988).
- 3 Matthay M. A., C. C. Landolt, N. C. Staub, Differential liquid and protein clearance from the alveoli of anesthetized sheep. *J. Appl. Physiol.: Respirat. Environ. Exercise Physiol.*, **53**(1): 96-104 (1982).
- 4 Menon, R. S., P. S. Allen, Solvent proton relaxation of aqueous solutions of the serum proteins  $\alpha_2$ -macroglobulin, fibrinogen, and albumin. *Biophysical Journal*, **57**: 389-396 (1990).
- 5 Spencer D. A., An update on PAF. *Cin. Exp. Allergy.*, **22**: 521-524 (1992).
- 6 Stroman P. W., et al., Evaluation of the effects of PAF on alveolar fluid clearance using NMR imaging. *J. Appl. Physiol.* (accepted).

### Appendix 3.3: Derivation of the Equations used to Compute the Time Course of Alveolar Fluid Absorption and of Alveolar Fluid Secretion

The derivation of the equations employed in Chapter 3 to compute the time course of alveolar fluid absorption,  $A(t)$ , and of alveolar fluid secretion,  $S(t)$ , depends on the premise that the observed clearance of  $^2\text{H}$  from the airspaces is only the result of alveolar fluid absorption. Assuming this premise to be true, the quantity of  $^2\text{H}$ ,  $Q_{\text{abs}}$ , that is absorbed from the lung over a period of duration,  $t$ , is given by

$$(A3.3.1) \quad Q_{\text{abs}}(t) = Q_D(0) A(t)$$

where  $Q_D(0)$  is the quantity of  $^2\text{H}$  initially instilled into the lung. The quantity of residual alveolar  $^2\text{H}$ ,  $Q_D(t)$ , is therefore

$$(A3.3.2) \quad Q_D(t) = Q_D(0) - Q_D(0) A(t)$$

Equation A4.2 can be rearranged to yield an expression for  $A(t)$

$$(A3.3.3) \quad A(t) = 1 - \frac{Q_D(t)}{Q_D(0)}$$

In order to derive a similar expression for  $S(t)$  however, we must first look at the net clearance time course,  $N(t)$ . The net amount of fluid,  $Q_{\text{Net}}$ , remaining in the lung at a time,  $t$ , after fluid instillation, is given by

$$(A3.3.4) \quad N(t) = Q_D(t) + Q_H(t)$$

where  $Q_H(t)$  is the quantity of residual alveolar  $^1H$ . Moreover, the quantity of fluid instilled into the lung initially is given by,  $Q_{Inst}$ , where

$$(A3.3.5) \quad Q_{Inst} = Q_D(0) + Q_H(0)$$

$N(t)$  is simply the amount of residual alveolar fluid relative to the instilled amount, and can therefore be expressed as

$$(A3.3.6) \quad N(t) = \frac{Q_D(t) + Q_H(t)}{Q_{Inst}}$$

$$(A3.3.7) \quad N(t) = \frac{Q_D(t)}{Q_D(0)} \frac{Q_D(0)}{Q_{Inst}} + \frac{Q_H(t)}{Q_H(0)} \frac{Q_H(0)}{Q_{Inst}}$$

For the study discussed in Chapter 3,  $Q_H(0)$  and  $Q_D(0)$  are equal, and the ratios  $Q_H(0)/Q_{Inst}$  and  $Q_D(0)/Q_{Inst}$  are both equal to  $1/2$ . As a result

$$(A3.3.8) \quad N(t) = \frac{1}{2} \left[ \frac{Q_D(t)}{Q_D(0)} + \frac{Q_H(t)}{Q_H(0)} \right]$$

Now, returning to the derivation of an expression for  $S(t)$ , we know from the definitions of  $N(t)$ ,  $A(t)$  and  $S(t)$ , that

$$(A3.3.9) \quad N(t) = 1 - A(t) + S(t)$$

which can be rearranged to give the following expression for  $S(t)$ .

$$(A3.3.10) \quad S(t) = N(t) + A(t) - 1$$

Substituting for  $A(t)$  and  $N(t)$  from equations A3.3.3 and A3.3.8 yields

$$(A3.3.11) \quad S(t) = \frac{1}{2} \left[ \frac{Q_D(t)}{Q_D(0)} + \frac{Q_H(t)}{Q_H(0)} \right] - \frac{Q_D(t)}{Q_D(0)}$$

$$(A3.3.12) \quad S(t) = \frac{1}{2} \left[ \frac{Q_H(t)}{Q_H(0)} - \frac{Q_D(t)}{Q_D(0)} \right]$$

The  $^1\text{H}$  and  $^2\text{H}$  NMR signal intensities,  $I_H(t)$  and  $I_D(t)$ , are assumed to be proportional to the quantities of  $^1\text{H}$  and  $^2\text{H}$  in the lung region of interest, so that

$$(A3.3.13) \quad \frac{I_H(t)}{I_H(0)} = \frac{Q_H(t)}{Q_H(0)}$$

$$(A3.3.14) \quad \frac{I_D(t)}{I_D(0)} = \frac{Q_D(t)}{Q_D(0)}$$

By substituting the relative NMR signal intensities for the quantities of  $^1\text{H}$  and  $^2\text{H}$  in the lung at a time  $t$  after fluid instillation, the expressions for  $N(t)$ ,  $A(t)$ , and  $S(t)$ , become

$$(A3.3.15) \quad N(t) = \frac{1}{2} \left[ \frac{I_D(t)}{I_D(0)} + \frac{I_H(t)}{I_H(0)} \right]$$

$$(A3.3.16) \quad A(t) = \left[ 1 - \frac{I_D(t)}{I_D(0)} \right]$$

$$(A3.3.17) \quad S(t) = \frac{1}{2} \left[ \frac{I_H(t)}{I_H(0)} - \frac{I_D(t)}{I_D(0)} \right]$$

#### **Appendix 4.1: Flow chart of the Mathematical Model of the Lung Fluid and Solute Exchange**

Definition of variables:

$abs+$  = the additional epithelial fluid absorption caused by PAF

$abs\_norm$  = the normal epithelial fluid absorption rate

$ap$  = the pore area

$asd$  = the effective area for solute diffusion through a single pore

$asf$  = the area for solute filtration through a single membrane pore

$awf$  = the area for water filtration through a single membrane pore

$a\_alb$  = the diameter of an albumin molecule

$a\_water$  = the diameter of a water molecule

$C$  = the mean concentration of solutes across the membrane

$chod\_as$  = the alveolar HOD concentration

$chod\_is$  = the interstitial HOD concentration

$decay\_time$  = the characteristic decay time of the PAF effect

$\Delta t$  = the element of time over which fluid and solute fluxes are integrated

$F\_end1$  = the number of endothelial pores of size #1

$F\_end2$  = the number of endothelial pores of size #2

$F\_ep$  = the number of epithelial pores

$J_s$  = the trans-membrane solute flux

$J_s\_as$  = the solute flux across the epithelium

$J_s\_is1$  = the solute flux across the endothelium through pore size #1

$J_s\_is2$  = the solute flux across the endothelium through pore size #2

$J_v$  = the trans-membrane fluid flux

$J_v\_as$  = the fluid flux across the epithelium

$J_v\_is1$  = the fluid flux across the endothelium through pore size #1

$J_{v_{is2}}$  = the fluid flux across the endothelium through pore size #2

$l_p$  = the membrane fluid permeability

$P_1$  = the hydrostatic pressure on side 1 of the membrane

$P_1$  = the hydrostatic pressure on side 1 of the membrane

$\pi_1$  = the protein osmotic pressure on side 1 of the membrane

$P_2$  = the hydrostatic pressure on side 2 of the membrane

$P_2$  = the hydrostatic pressure on side 2 of the membrane

$\pi_2$  = the protein osmotic pressure on side 2 of the membrane

$\pi_{as}$  = the protein osmotic pressure of the alveolar space fluid

$\pi_{is}$  = the protein osmotic pressure of the interstitial space fluid

$\dot{Q}_{fas}$  = the rate of fluid flux across the epithelium

$\dot{Q}_{fis}$  = the rate of fluid flux across the endothelium

$\dot{Q}_{sas}$  = the rate of solute flux across the epithelium

$\dot{Q}_{sis}$  = the rate of solute flux across the endothelium

$q_{hod_{as}}$  = the quantity of HOD in the alveolar space

$q_{hod_{is}}$  = the quantity of HOD in the interstitial space

$Q_{lymph}$  = the rate of lymph flow out of the interstitial space

$q_{s_{as}}$  = the quantity of solutes in the alveolar space

$r_p$  = the radius of a membrane pore

$\sigma$  = the solute reflection coefficient

$sec+$  = the additional epithelial fluid secretion caused by PAF

$sec_{norm}$  = the normal epithelial fluid secretion rate

$Sin_{as}$  = the solute flux rate into the alveolar space

$Sin_{is}$  = the solute flux rate into the interstitial space

$Sout_{as}$  = the solute flux rate out of the alveolar space

$Sout_{is}$  = the solute flux rate out of the interstitial space

$t$  = time elapsed since the instillation of fluid into the lung

$V_{in\_as}$  = the fluid flux rate into the alveolar space

$V_{in\_is}$  = the fluid flux rate into the interstitial space

$V_{out\_as}$  = the fluid flux rate out of the alveolar space

$V_{out\_is}$  = the fluid flux rate out of the interstitial space

$v_{as}$  = the alveolar fluid volume

$v_{instilled}$  = the volume of fluid instilled into the alveolar space

$v_{int}$  = the interstitial fluid volume

$v_{int\_initial}$  = the interstitial fluid volume of the normal lung

$\omega$  = the permeability of the membrane to solutes

